DYNAMIC IMAGING OF SECRETION FROM PANCREATIC BETA-CELLS BY CONFOCAL FLUORESCENCE MICROSCOPY

By

WEIJUN QIAN

A DISSERTATION PRESENTED TO THE GRADUATE SCHOOL
OF THE UNIVERSITY OF FLORIDA IN PARTIAL FULFILLMENT
OF THE REQUIREMENTS FOR THE DEGREE OF
DOCTOR OF PHILOSOPHY

UNIVERSITY OF FLORIDA

2002

To my parents for their guidance and support and my wife for her love, support and encouragement.

ACKNOWLEDGMENTS

I would like to express my sincere thanks to my advisor, Dr. Robert T. Kennedy, for his continuous guidance and support throughout my graduate career. I would also like to thank all the members of the Kennedy group, past and present, for their help during my time in the Kennedy lab. I would especially like to thank Dr. Craig A. Aspinwall and Mr. Michael G. Roper for their help and collaboration in part of my research, especially the amperometric detection of secretion presented in Chapter 6. I would also like to express my gratitude to Dr. Jennifer L. Peters for her help during the writing of my dissertation.

I would like to express my appreciation to Dr. Kyle R. Gee at Molecular Probes for supplying samples of zinc fluorophores and for his collaboration. I would like to thank Dr. Merle A. Battiste for his assistance in the synthesis of the zinc fluorophore Zinquin. I would like to thank all of the members of my doctoral committee—Dr. Mark A. Atkinson, Dr. Jon D. Stewart, Dr. Weihong Tan, and Dr. Richard A. Yost—for their wisdom, assistance, and encouragement. I would also like to thank Eastman Chemical Company, GE Plastics, the American Chemical Society Division of Analytical Chemistry, and the UF Chemistry Department Division of Analytical Chemistry for sponsoring fellowships to fund this work.

TABLE OF CONTENTS

page

ACKNOWLEDGMENTS iii

LIST OF ABBREVIATIONS vii

ABSTRACT x

CHAPTERS

1 INTRODUCTION 1

Secretion of Neurotransmitters and Hormones 1
Insulin Secretion and Diabetes Mellitus 2
Pancreatic Islets and β-cells 5
Stimulus-secretion Coupling in β-cells 7
Techniques for Monitoring Insulin Secretion 11
Fluorescence Imaging Techniques for Monitoring Exocytosis 14
Confocal Fluorescence Microscopy 16
Dissertation Overview 18

2 DETECTION OF SECRETION FROM SINGLE PANCREATIC β-CELLS USING EXTRACELLULAR FLUOROGENIC REACTIONS AND CONFOCAL FLUORESCENCE MICROSCOPY 19

Introduction 19
Experimental 21
Results 28
Discussion 45
Conclusion 49

3 SPATIAL ORGANIZATION OF Ca^{2+} ENTRY AND EXOCYTOSIS IN MOUSE PANCREATIC β-CELLS 51

Introduction 51
Experimental 53
Results 55
Discussion 66

4 DETECTION AND IMAGING Zn^{2+} RELEASE AT THE LEVEL OF SINGLE EXOCYTOTIC EVENTS 71

Introduction 71
Experimental 73
Results 77
Discussion 94

5 TEMPORAL AND SPATIAL PATTERNS OF OSCILLATORY Zn^{2+} SECRETION FROM CLUSTERS OF PANCREATIC β-CELLS AND ISLETS OF LANGERHANS REVEALED BY FLUORESCENCE IMAGING 100

Introduction 100
Experimental 102
Results 105
Discussion 118

6 ROLES OF INSULIN RECEPTOR SUBSTRATE-1, PHOSPHATIDYLINOSITOL 3-KINASE, AND RELEASE OF INTRACELLULAR Ca^{2+} STORES IN INSULIN-STIMULATED INSULIN SECRETION IN β-CELLS 124

Introduction 124
Experimental 127
Results 132
Discussion 144

7 SUMMARY AND FUTURE DIRECTIONS 149

Summary 149
Future Directions 153

APPENDICES 157

A NIKON RCM 8000 CONFOCAL LASER-SCANNING SYSTEM 157

Introduction of the System 157
Imaging Operation 160
Data Analysis and Image Presentation 164
Instrumental Maintenance 165

B CONFOCAL IMAGING OF INTRACELLULAR FREE Ca^{2+} CONCENTRATIONS 167

Fluorescent Ca^{2+} Probes 167
Confocal Imaging of Ca^{2+} in Pancreatic β-cells 167

LIST OF REFERENCES 171

BIOGRAPHICAL SKETCH 183

LIST OF ABBREVIATIONS

5-HT	5-hydroxytryptamine
5-HTP	5-hydroxytryptophan
ADP	Adenosine diphosphate
AM	Acetoxymethyl ester
ATP	Adenosine triphosphate
βTC3	Insulin secreting tumor line
$[Ca^{2+}]_i$	Intracellular free Ca^{2+} concentration
cAMP	Cyclic adenosine monophosphate
CLSM	Confocal laser-scanning microscope
DMEM	Dulbecco's modified Eagle's medium
DMSO	Dimethylsulfoxide
EDTA	Ethylenediaminetetraacetic acid
EGTA	Ethylene glycol-bis(2-aminoethyl)-N,N,N',N'-tetraacetic acid
ELISA	Enzyme-linked immunosorbent assay
ER	Endoplasmic reticulum
FBS	Fetal bovine serum
GABA	γ-aminobutyrate
GLUT-2	Type 2 glucose transporter
GSIS	Glucose-stimulated insulin secretion

HBSS	Hanks' Balance Salt Solution
HEPES	N-(2-hydroxyethyl)piperazine-N'-(2-ethanesulfonic acid)
IDDM	Insulin-dependent diabetes mellitus
IP_3	Inositol 1,4,5-triphosphate
IRS	Insulin receptor substrate
KRB	Krebs-Ringer buffer
NA	Numerical aperture
NIDDM	Non-insulin-dependent diabetes mellitus
NMDA	N-methyl-D aspartate
OMDR	Optical Monochrome Disc Recorder
PI-3K	Phosphoinositol 3-kinase
PIP_3	Phosphatidylinositol 3,4,5-triphosphate
PKB	Protein kinase B
PKC	Protein kinase C
PLC	Phospholipase C
PMT	Photomultiplier tube
RIA	Radioimmunoassay
ROI	Region of interest
RRP	Readily releasable pool
S.D.	Standard deviation
SEM	Standard error of the mean
SERCA	Sarcoplasmic and endoplasmic reticulum Ca^{2+}-ATPases
S/N	Signal-to-Noise ratio

SNAP-25	Synaptosomal protein of 25 kDa
SNAREs	Soluble *N*-ethylmaleimide-sensitive factor attachment protein receptors
SSCE	Sodium-saturated calomel reference electrode
TPEN	Tetrakis-(2-pyridylmethyl)ethylenediamine
UV	Ultraviolet

Abstract of Dissertation Presented to the Graduate School
of the University of Florida in Partial Fulfillment of the
Requirements for the Degree of Doctor of Philosophy

DYNAMIC IMAGING OF SECRETION FROM PANCREATIC BETA-CELLS BY CONFOCAL FLUORESCENCE MICROSCOPY

By

Weijun Qian

May 2002

Chair: Robert T. Kennedy
Major Department: Chemistry

Insulin is stored in secretory vesicles of pancreatic β-cells and secreted by exocytosis in response to external stimuli, most notably glucose. A better understanding of stimulus-secretion coupling is of great interest due to the possible role of defective insulin secretion in type 2 diabetes. Studies of stimulus-secretion coupling require analytical techniques that allow the monitoring of secretion with high temporal and spatial resolution.

In this work, a fluorescence imaging approach has been developed for spatially and temporally resolved measurements of secretion from β-cells using extracellular fluorogenic reactions and confocal laser-scanning fluorescence microscopy. In this method, Zn^{2+} efflux from β-cells is monitored as a marker of insulin secretion because of the co-release of Zn^{2+} and insulin from β-cells by exocytosis. To detect Zn^{2+} release, cells are incubated in buffer containing the fluorogenic Zn^{2+} indicator Zinquin, while fluorescence signals are monitored by confocal fluorescence microscopy. When secretion is evoked by stimulation, the released Zn^{2+} reacts with Zinquin in the extracellular space to form a fluorescent complex, resulting in an increase in fluorescence at the site of release. Spatial organization of β-cell secretion has been investigated using this spatially resolved technique. It was revealed that secretion from single β-cells was localized and the active areas of release spatially co-localized with $_{L}$-type Ca^{2+} channels on the plasma membrane of cells.

The sensitivity and temporal resolution of this approach was further improved with the use of a novel Zn^{2+} indicator FluoZin-3. Temporally resolved exocytotic release from individual secretory vesicles has been observed for the first time by a fluorescence imaging technique. Unlike other single-cell techniques that limit their applications to single cells, this approach allows the monitoring of secretion from clusters of cells and single islets with sub-second temporal resolution. For the first time, oscillatory secretion from cell clusters and single islets was observed with high temporal resolution. Complex patterns of oscillatory secretion, spatial heterogeneity, and spatial synchrony of secretion from cell clusters and islets have been revealed. The high sensitivity, high temporal and spatial resolution of this technique would make it a valuable tool for physiological studies of insulin secretion and exocytosis.

CHAPTER 1
INTRODUCTION

Secretion of Neurotransmitters and Hormones

Regulated secretion of neurotransmitters and hormones by exocytosis is a complex process that is of fundamental importance in cell physiology. Many biological functions or processes such as cellular communication in neuronal and endocrine systems, body homeostasis, metabolism, and growth are regulated by secretion of these biochemical messengers including small molecules, peptides, and proteins. Hormones or neurotransmitters are synthesized by cells, stored in membrane-bounded secretory vesicles or granules and secreted from cells via exocytosis (Almers, 1990). Figure 1-1 shows a schematic diagram of the steps of vesicle trafficking toward exocytosis. Exocytosis is a multistage process involving transport of secretory vesicles to the plasma membrane, vesicle docking, vesicle priming, vesicle fusion with the plasma membrane, and finally extrusion or clearance of the vesicular contents into the extracellular space. It is generally believed that exocytosis is a calcium-dependent process and is regulated by a cascade of protein-protein interactions, known as the assembly and disassembly of the complex of soluble N-ethylmaleimide sensitive factor attachment protein receptors (SNAREs) (Söllner et al., 1993; Rothman, 1994; Mochida, 2000).

The diameter of individual secretory vesicles is typically in the range of 25 to 500 nm. Each vesicle contains between 5000 to 10^6 molecules and release of vesicular contents to the extracellular space occurs on the time scale of milliseconds (Travis and

Wightman, 1998). Analytical techniques with high sensitivity, high spatial and temporal resolution are required for detection of such rapid exocytotic release events. Furthermore, monitoring the dynamics of secretion is of interest in order to achieve a fundamental understanding of secretory processes and their regulation.

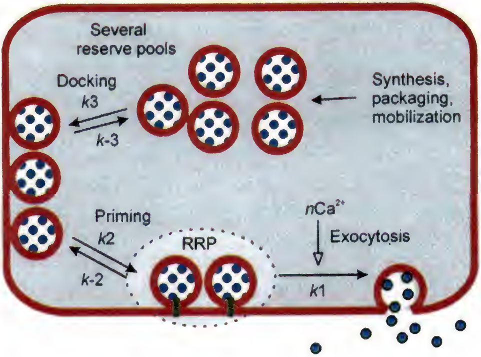

Figure 1-1. Kinetic pools of vesicles in the regulated secretory pathway in an excitable cell. Neurotransmitters or hormones are synthesized and packed inside the secretory vesicles. Exocytosis (step k1) is triggered by binding of Ca^{2+} ions. The small readily releasable pool (RRP) of vesicles is formed by priming (step k2) of docked vesicles. Docked vesicles are formed (step k3) by mobilization and transport from deep intracellular pools. (Adapted from Hille et al., 1999)

Insulin Secretion and Diabetes Mellitus

Secretion of insulin from pancreatic β-cells is an important example of regulated secretion of hormones by exocytosis in the endocrine system. Insulin is a pluripotent hormone that has a wide sphere of influence on virtually every organ and tissue in the body. Finely controlled secretion of insulin is the primary regulator of glucose homeostasis (Polonsky, 1995), an essential feature for the life of higher vertebrates. In addition to its major role in glucose homeostasis, insulin also influences a variety of other cellular processes including glycolysis, transport of ions and amino acids, lipid metabolism, DNA synthesis, gene transcription, protein synthesis and degradation, and cellular proliferation and differentiation (Gupta, 1997). The physiological significance of insulin becomes obvious in the light of its crucial involvement in diseases such as diabetes mellitus and obesity.

Diabetes mellitus, or more commonly diabetes, is the most prevalent metabolic disease worldwide (Kahn, 1998). Diabetes is a major public health problem in the US, affecting ~5% of the population (Taylor, 1999). If not controlled, diabetes can have devastating consequences for the eyes, kidneys, and blood vessels, and severely reduce life expectancy (Orci et al., 1988). Clinically, there are two common forms of diabetes: type 1 or insulin-dependent diabetes mellitus (IDDM) and type 2 or non-insulin-dependent diabetes mellitus (NIDDM). Type 1 diabetes results from an autoimmune destruction of pancreatic β-cells, leading to a near total deficiency of insulin secretion (Figure 1-2). Type 2 diabetes is the most common form of diabetes, accounting for more than 90% of diabetic patients. It is characterized by two physiological defects: resistance to the action of insulin on peripheral tissues and impaired insulin secretion from pancreatic β-cells (DeFronzo, 1997), both of which lead to hyperglycemia, the clinical hallmark of diabetes. There has been considerable controversy about which of these two defects is primary and which is secondary in type 2 diabetes (Kahn et al. 1996, Ferrannini, 1998); however, it is generally agreed that defective insulin secretion is a requirement for the disease to develop (Efendic and Östenson, 1993). Initially, insulin resistance is compensated by increased insulin secretion from β-cells and normal glucose homeostasis is maintained. Overt diabetes develops only if a defect in insulin secretion develops and β-cell compensation fails (Kahn, 1998).

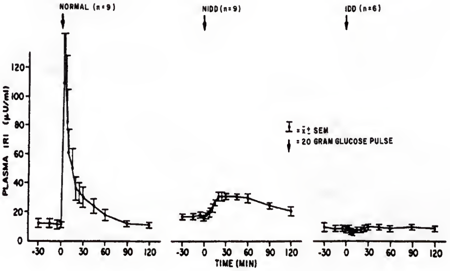

Figure 1-2. Glucose-stimulated insulin response in normal, NIDDM (type 2) and IDDM (type 1) patients. (Adapted from Kahn et al., 1997).

Several lines of evidence suggest the important role of defective insulin secretion in the development of type 2 diabetes. Under normal conditions, insulin response to a glucose challenge is biphasic, with a rapid first phase of secretion and a sustained second phase of secretion (Figure 1-2). In some of NIDDM patients, the first phase of insulin response is markedly reduced or lost (Figure 1-2), suggesting dysfunction of β-cells in these patients. Another interesting feature of insulin secretion in type 2 diabetes is that the normal oscillatory secretion is abolished in most patients and also in their relatives (O'Rahilly et al., 1988; Polonsky et al., 1988b). Indeed, loss of oscillatory insulin release has been shown to be an early symptom of type 2 diabetes (O'Rahilly et al., 1988). Owing to the importance of impaired insulin secretion in type 2 diabetes, there has been considerable interest in trying to understand the regulatory mechanisms of insulin secretion. To date, there is no convincing data to support the hypothesis that defective insulin release is caused by markedly reduced β-cell mass or impaired biosynthesis of insulin (Östenson, 2001). Therefore, it is more likely that defective insulin secretion arises from specific defects in the regulatory mechanisms of insulin secretion (Flatt et al., 1992).

Pancreatic Islets and β-cells

Insulin is produced and stored in the β-cells of islets of Langerhans in the pancreas. The mammalian pancreas contains both exocrine and endocrine tissue. The exocrine tissue secretes major digestive enzymes such as the proteases trypsin, amylase, and lipase, while the endocrine tissue of the pancreas produces the peptide hormone insulin, glucagon, pancreatic polypeptide, somatostatin, and small amounts of other peptide hormones (Norman and Litwack, 1997). The endocrine tissue of pancreas is known as islets of Langerhans, which are clusters of endocrine tissue scattered throughout the pancreas. Each islet is a complex mixture of cells and functions both separately as a microorgan and in concert as the endocrine pancreas. There are approximately one million islets in the adult human pancreas, which make up only about 1-2% total pancreatic weight (Orci et al., 1988). An islet can vary in size from only a few cells and a diameter of less than 40 μm, to about 5000 cells and a diameter of 400 μm (Bonner-Weir, 1991). There are four basic types of cells in mammalian islets: the glucagon-producing α–cells, the insulin-producing β-cells, the somatostatin-producing δ–cells, and the pancreatic polypeptide-producing pp-cells. The endocrine cells in an islet are arranged in a nonrandom distribution with the β-cells forming a central core surrounded by a discontinuous mantle of non-β-cells. Of all four types of cells, the β-cell accounts for 60-80% of cells within the islet, the α-cell for 15-20%, and the δ-cell and pp-cell for the remaining ~20%.

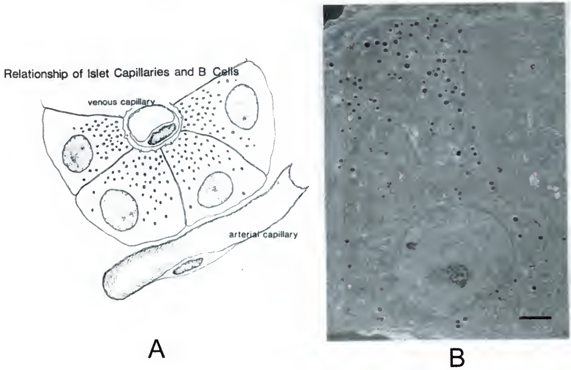

Figure 1-3. Islets of Langerhans and pancreatic β-cells. (A) Diagram of the cross-sectional array of β-cells around a central capillary. The outer face of each β-cell also abuts a capillary, which is not usually in cross section. The distribution of granules in β-cells is polarized toward the central capillary. (Adapted from Bonner-Weir, 1989). (B) Electron micrograph of a partially degranulated pancreatic β-cell. The remaining secretory granules (black dots) show clear polarity with the majority of granules accumulated at the upper portion of the cell. Bar = 2 μm. (Adapted from Bonner-Weir, 1988)

The islet has an infrastructure of microvasculature and nerves around which the endocrine cells are organized. As shown in Figure 1-3A, the β-cells are arranged so that a ring of cells face a central capillary, which would be tubelike in three-dimensions. The outer face of each cell also faces a capillary, which is not usually in cross-section (Bonner-Weir, 1989). Figure 1-3B shows an electron micrograph of an experimentally degranulated β-cell. The remaining secretory granules show an obvious polarity with the majority of granules accumulated at one end of the cell facing one capillary. The uneven distribution of granules suggests that β-cells in an islet may be polarized toward the central capillary (Bonner-Weir, 1988).

The β-cell cytoplasm is filled with insulin-containing secretory granules (Bonner-Weir, 1988). In the secretory granules, insulin is crystallized as Zn^{2+}-insulin hexamers with two Zn^{2+} per hexamer (Blundell et al., 1972). Figure 1-4A shows an electron micrograph of an isolated insulin granule obtained from a rat at high magnification. The graph shows a rough hexagonal outline with a well-defined repeating distance of 40-50 Å (Howell et al., 1969). This corresponds to the 50 Å diameter of Zn^{2+}-insulin hexamer in the rhombohedral crystal as shown in Figure 1-4B (Howell et al., 1969). *In vitro* experiments showed that insulin precipitated in the presence of Zn^{2+} was crystalline only between pH 6.2 and 6.4, which suggests that pH in the secretory granules is likely to be between 6.2 and 6.4 (Blundell et al., 1972). In response to external stimuli such as glucose, the insulin granule will fuse with the plasma membrane and expose its content to extracellular environment, which has a pH of ~7.4. Since the insulin crystal is much more soluble at high pH and high ionic strength (Coore et al, 1969), it is expected that the insulin granule will dissolve rapidly and diffuse into the large volume of bloodstream after the granule is fused with the plasma membrane. The co-release of insulin and Zn^{2+} from the secretory granules of β-cells is illustrated in the diagram of Figure 1-5.

Stimulus-secretion Coupling in β-cells

Insulin secretion from pancreatic β-cells has a unique stimulus-secretion coupling, which requires the oxidative mechanisms of glucose or other metabolic fuels (Newgard and McGarry, 1995). Besides glucose, other nutrient secretagogues such as certain amino acids or free fatty acids also stimulate insulin release, but usually require a basal glucose level in order to do so (Liang and Matschinsky, 1994). Although the

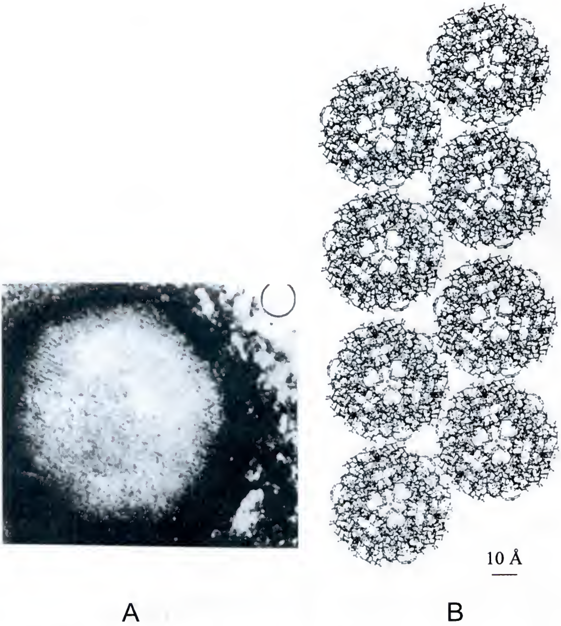

Figure 1-4. Insulin granule and insulin-Zn^{2+} crystal. (A) Electron micrograph of an isolated insulin granule from a rat. The repeat distances of about 50 Å are apparent. (B) The organization of the Zn^{2+}-insulin hexamer in the rhombohedral crystal. (Adapted from Blundell et al., 1972)

physiological mechanism responsible for glucose-stimulated insulin secretion (GSIS) is only partially understood, it is generally accepted that insulin secretory response is tightly dependent on the rate of glucose metabolism. Pancreatic β-cells can be viewed as fuel sensors since they can sense subtle changes in blood glucose concentration and release appropriate amounts of insulin. The GLUT-2 and glucokinase in β-cells are responsible for translating the changes in blood glucose concentration into signal-generating metabolic flux rates for initiation of insulin secretion (Liang and Matschinsky, 1994). The activity of glucokinase is considered as the rate-limiting step in β-cell glucose metabolism since glucose transport is almost 100 times faster than glucose phosphorylation catalyzed by glucokinase (Liang and Matschinsky, 1994). Many metabolic factors generated during glucose metabolism also potentiate or enable GSIS, but how these factors regulate GSIS is still unclear.

In addition to blood glucose, neurotransmitters such as acetylcholine and catecholamines and hormones such as glucagon, somatostatin, and insulin itself regulate insulin secretion under physiological conditions (Liang and Matschinsky, 1994; Aspinwall et al., 1999a). These hormones and neurotransmitters first bind to specific receptors on the β-cell membrane and then generate secondary messengers that regulate insulin secretion (Liang and Matschinsky, 1994). The most important secondary messenger in insulin secretion probably is calcium and the concept of calcium-secretion coupling in β-cells is well accepted (Hellman et al., 1992). Under physiological conditions, intracellular Ca2+ concentrations ($[Ca^{2+}]_i$) in β-cells are regulated by a sophisticated interplay between nutrients, hormones, and neurotransmitters (Berggren and Larson, 1994). Besides calcium, other secondary messengers such as cyclic adenosine monophosphate (cAMP), diacylglycerol, nitric oxide, and arachidonic acid may also have important roles in modulating the effects of specific secretagogues on insulin secretion (Howell et al., 1994).

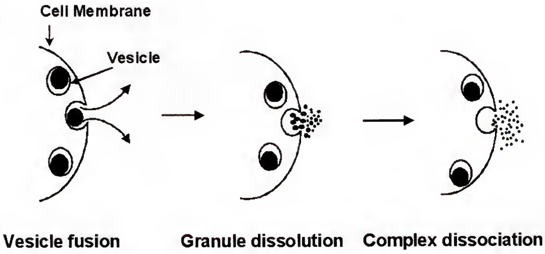

$$(INS_6Zn_2)_{solid} \xrightarrow{-H^+} (INS_6Zn_2)_{soln} \longrightarrow INS_x + 2\,Zn^{2+}$$

Figure 1-5. Co-release of insulin and Zn^{2+} from secretory vesicles of β-cell. Zn^{2+} and insulin are stored as a solid complex in the secretory vesicles. The pH inside vesicles is ~ 6.4. Upon stimulation, secretory vesicles fuse with the plasma membrane and expose the insulin-Zn^{2+} granules to extracellular medium. Due to the high pH in the extracellular environment (pH = 7.4), the insulin-Zn^{2+} granule will dissolve and dissociate into free biological active insulin and Zn^{2+}.

While it is known that insulin secretion is regulated by a sophisticated interplay between nutrients, hormones and neurotransmitters, the nature of stimulus-secretion coupling in β-cell is still far from clear. It is certain, however, that a defect at any point in the stimulus-secretion coupling pathways will result in impaired insulin secretion, which plays an important role in the development of type 2 diabetes. Indeed, marked insulin secretory defects were demonstrated recently in knockout mice with insulin receptor substrate-1 (IRS-1) deficiency (Kulkarni et al., 1999a) as well as mice lacking insulin receptors in their β-cells (Kulkarni et al., 1999b). Therefore, it is of great importance to gain a better understanding of stimulus-secretion coupling in β-cells.

Techniques for Monitoring Insulin Secretion

Advances in the techniques used for monitoring insulin secretion have greatly contributed to the study of stimulus-secretion coupling in β-cell. Insulin is stored in secretory vesicles with an average diameter of 300 nm in human (Larsson et al., 1976). Each secretory vesicle within the β-cell contains approximately 1.6 attomoles of insulin and the release of insulin from individual vesicles occurs on the time scale of milliseconds (Huang et al., 1995). Ideally, techniques for monitoring insulin secretion should have attomole or less mass sensitivity, millisecond temporal resolution, and sub-micron spatial resolution in order to detect the dynamic release from individual vesicles and localize the site of release on the cell. However, none of the previous techniques used to measure insulin release fulfills all of these requirements, although techniques with high temporal resolution or high spatial resolution have been developed for detection of insulin secretion (Huang et al., 1995; Tsuboi et al., 2000).

The first method to measure insulin was radioimmunoassay (RIA), introduced by Yalow and Berson in 1960. Now RIA has become a common approach for monitoring insulin secretion from perfused whole pancreas or populations of islets. With improved sensitivity, RIA has been applied to monitor oscillations in secretion from single islets (Rosario et al., 1986; Gilon et al., 1993). However, RIA suffers from low sensitivity and poor temporal resolution. Since RIA is a mass sensitive technique, long sampling times are required for monitoring secretion from smaller samples such as single islets, resulting in poor temporal resolution. Typically, the temporal resolution of RIA is 30-180 s.

Enzyme-linked immunosorbent assay (ELISA) has also been developed and applied to monitor secretion from single islets with improved sensitivity and temporal resolution (Bergsten and Hellman, 1993a). Secretion monitored by RIA and ELISA is an average response from a population of cells. It has not been possible to reveal the functional heterogeneity in secretion from individual β-cells by these techniques, although individual β-cells are known to be functionally heterogeneous (Jonkers et al., 2001). Therefore, techniques with sufficient sensitivity to monitor insulin secretion from single cells would be of interest.

During the last decade, two techniques have been introduced to monitor secretion from single cells, including pancreatic β-cells, with high sensitivity and temporal resolution. One of these is membrane capacitance measurements, which assess rapid changes in membrane surface area using patch-clamp techniques (Penner and Neher, 1989; Gillis and Misler, 1992). The plasma membrane can be modeled as a capacitor and the total capacitance of a given cell is proportional to the surface area of the plasma membrane. Membrane capacitance can be monitored in real time with increases in capacitance corresponding to increases in plasma membrane area caused by vesicle fusion. Although capacitance measurements have been used as a general approach for monitoring exocytosis on many cell types, this technique suffers several limitations. For example, this method measures secretion indirectly and the correlation between capacitance change and vesicle fusion is still questionable. Also, capacitance measurements cannot distinguish changes caused by exocytosis and endocytosis because the increase of plasma membrane area is a net result of these two processes.

The second technique, amperometry with carbon fiber microelectrodes, allows the direct detection of secretory products from single cells with high sensitivity and temporal resolution (Wightman et al., 1991). In amperometry, the microelectrode, held at a constant potential, is positioned close to an isolated cell surface and electrochemically active secretion products are directly oxidized and detected at the electrode surface (Figure 1-6). Secretion is detected as a series of current spikes corresponding to the detection of concentration pulses of released products generated by exocytosis. It has been shown that exocytosis occurs as quantal release of vesicular contents and an individual spike on the amperometric current trace corresponds to a single exocytotic event (Wightman et al., 1991). If the number of electrons per molecule in the redox reaction is known, the quantity of molecules secreted for a single exocytotic event can be calculated from the spike area according to Faraday's law. Amperometry with microelectrodes has been applied to quantitative measurements of exocytosis from adrenal chromaffin cells (Wightman et al., 1991; Chow et al., 1992), PC12 cells (Chen et al., 1994), mast cells (Tatham et al., 1991), neurons (Zhou and Misler, 1995), and melanotrophs (Paras and Kennedy, 1995). Recently, amperometry has been applied to characterize secretory activities at pancreatic β-cells by directly detecting secreted insulin with a ruthenium oxide/cyano-ruthenate modified carbon fiber microelectrode (Huang et al., 1995). Unfortunately, the modified electrode used for direct detection of insulin is not stable at physiological pH and the sensitivity of detection is species dependent. Alternatively, 5-hydroxytryptamine (5-HT), a substance that is accumulated primarily into secretory vesicles of β-cells during bath incubation and is co-secreted with insulin, has been used as a marker of insulin secretion (Zhou and Misler, 1996; Aspinwall et al., 1997; Aspinwall et al., 1999b). 5-HT is easily oxidized at bare carbon fiber electrodes.

Although capacitance measurements and amperometry have been successfully applied to the detection of secretion from single β-cells with high temporal resolution, a common limitation of these techniques is that they are both single point measurements, meaning that these measurements do not provide a spatially resolved picture of release from β-cells. As complementary to single point measurements, spatially resolved imaging (such as fluorescence imaging) of secretion from cells would also be of interest, especially for probing the spatial organization of exocytosis.

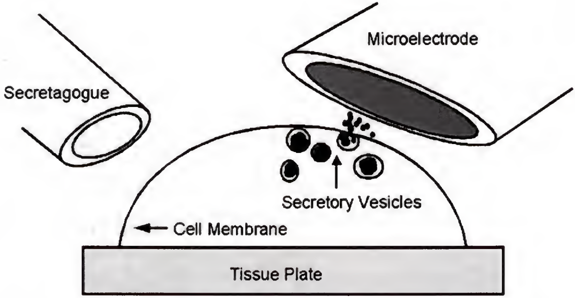

Figure 1-6. Schematic drawing of the basic experimental setup for amperometric detection of secretion from a single cell (Not to scale).

Fluorescence Imaging Techniques for Monitoring Exocytosis

Fluorescence microscopic imaging has become increasingly important for the study of living cells because it allows one to visualize dynamic chemical changes in cells. Recent advances in fluorescence imaging have resulted in several new approaches for monitoring exocytosis. First, laser-induced native fluorescence imaging with UV excitation or multi-photon excitation has allowed monitoring of exocytotic release of certain hormones such as serotonin and catecholamines from neurons and mast cells (Yeung, 1999; Maiti et al., 1997; Williams et al., 1999). Native fluorescence imaging of insulin secretion from pancreatic β-cells, however, has not been reported. Second, the development of membrane-specific fluorescent markers such as styryl dyes, most notably FM 1-43, has made the measurement of membrane trafficking associated with exocytosis, endocytosis, and vesicle cycling possible with fluorescence imaging (Smith and Betz, 1996; Cochilla et al., 1999). FM 1-43 molecules reversibly partition into the outer leaflet of exposed membrane, displaying enhanced fluorescence after partitioning into the membrane. Increases in membrane area due to exocytosis can be detected as increases in fluorescence when FM 1-43 is present in the extracellular buffer (Smith and Betz, 1996). FM 1-43 can also be internalized by endocytosis and vesicle trafficking can be monitored by imaging stained recycled vesicles (Cochilla et al., 1999). Although FM 1-43 imaging has been applied in many neuronal and nonneuronal cells, it is unclear whether or not this technique is applicable to the monitoring of secretion from β-cells. Finally, vesicle trafficking and exocytosis can be monitored by directly labeling secretory vesicles with fluorescent dyes. Secretory vesicles, including insulin-containing secretory granules, have been labeled with a weak base fluorescent dye acridine orange, which tends to accumulate into the acidic compartments of the cells (Bokvist et al., 1995; Steyer et al., 1997). Secretory vesicles have also been labeled by fusion of green fluorescence protein (or its derivatives) to vesicle membrane protein or vesicular protein (Pouli et al., 1998;Tsuboi et al., 2000; Ohara-Imaizumi et al., 2002). Using confocal microscopy or evanescent-wave microscopy, imaging of exocytosis from individual labeled vesicles from several types of cells including pancreatic β-cells has been reported (Steyer et al., 1997; Tsuboi et al., 2000; Ohara-Imaizumi et al., 2002).

Confocal Fluorescence Microscopy

One of the most important advances in fluorescence imaging is the introduction of confocal microscopy. Compared to conventional epi-fluorescence microscopy, confocal microscopy provides improved spatial resolution and signal-to-noise ratio (S/N) by combining focused illumination with filtered detection to collect signal from a diffraction-limited focal volume while rejecting out-of-focus light (Pawley, 1995). As shown in Figure 1-7, a laser beam is focused onto an excitation pinhole, which produces a point source of illumination. The emission pinhole, located at the confocal point, allows emission light from the focal point to pass through to the detector (green solid line). Light emitted from outside the focal point is rejected by the pinhole (dashed line). Thus, signal to background ratio is greatly improved due to the rejection of out-of-focus light by the emission pinhole. The diameter of focused spot is diffraction-limited, typically 0.2 μm for a high numerical aperture (NA) microscope objective. The stray light arising from simultaneous excitation of multiple regions of the specimen is greatly reduced in confocal microscopy because only one spot is illuminated at any point of time. Therefore, spatial resolution in confocal microscopy is also improved compared to conventional microscopy. By scanning the focused spot relative to the specimen in X-Y directions, two-dimensional images can be obtained. Because only the light emitted from the focal plane can reach the detector and the out-of-focus fluorescence is rejected, confocal microscopy offers great improvement in depth discrimination (Z-axis resolution) over conventional microscopy. A three-dimensional image can be reconstructed by collecting a series of images from various focal planes of the specimen (optical sectioning). With the development of high speed laser-scanning systems and imaging processing techniques, confocal microscopy has become an essential analytical technique for monitoring dynamic processes and fast signaling in living cells.

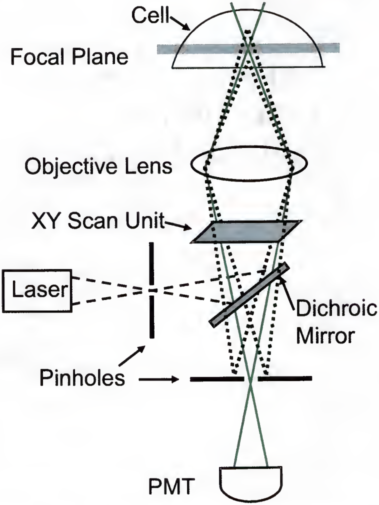

Figure 1-7. Schematic diagram of a confocal laser-scanning microscope. The excitation pinhole at the confocal point allows excitation light to be focused onto a diffraction-limited spot on the sample. The emission pinhole allows the light from the focal point to pass through to the PMT detector while rejecting the light emitted from above or below the focal spot. A two-dimensional fluorescence image at the focal plane is obtained by scanning the light across the sample through the XY scan unit.

Dissertation Overview

The overall objectives of this research are to develop a spatially resolved imaging approach for monitoring dynamic secretion from pancreatic β-cells using confocal fluorescence microscopy and to apply this approach to study stimulus-secretion coupling of β-cells.

Chapter 2 describes the development of a novel imaging approach for spatially and temporally resolved measurement of Zn^{2+} secretion from single pancreatic β-cells using confocal fluorescence microscopy and extracellular fluorogenic reactions. In chapter 3, the developed imaging approach was applied to study the spatial organization of β-cell secretion. Chapter 4 describes the detection of Zn^{2+} release at the level of single exocytotic events with much improved sensitivity and temporal resolution by using a novel Zn^{2+} fluorophore FluoZin-3. Chapter 5 describes the applications of this improved approach in monitoring oscillatory secretion from clusters of cells and single islets of Langerhans. In chapter 6, the intracellular mechanism through which insulin stimulates insulin secretion in the pancreatic β–cell was investigated by the combination of confocal fluorescence imaging of intracellular Ca^{2+} concentrations and Zn^{2+} secretion and amperometric detection of secretion.

CHAPTER 2

DETECTION OF SECRETION FROM SINGLE PANCREATIC β-CELLS USING EXTRACELLULAR FLUOROGENIC REACTIONS AND CONFOCAL FLUORESCENCE MICROSCOPY

Introduction

Insulin produced and stored in pancreatic β-cells is released by exocytosis in response to glucose and other stimuli. A greater understanding of stimulus-secretion coupling and exocytosis at β-cells is of intense interest due to mounting evidence for the importance of defective insulin secretion in type 2 diabetes (Avruch, 1998; Kahn, 1998). Studies of stimulus-secretion coupling and exocytosis in these cells are greatly aided by techniques that allow high resolution monitoring of secretion. Amperometry has proven useful in monitoring secretion from single cells, even at the level of single exocytotic events, because it allows detection of attomole quantities with millisecond temporal resolution (Chow et al., 1992; Chen et al., 1994; Wightman et al.; 1991). Amperometry has been applied to β-cells either by using a ruthenium oxide/cyanoruthenate-coated microelectrode to directly detect insulin (Huang et al., 1995; Aspinwall et al., 1997) or by using a carbon fiber microelectrode to detect 5-hydroxytryptamine (5-HT) that had been allowed to accumulate into the secretory vesicles (Smith et al., 1995; Zhou and Misler, 1996). A limitation of amperometry is that a microelectrode is inherently a single-point sensor, meaning that measurements are made at one location on a cell with a detection area determined by the size of the electrode. In principle this limitation of amperometry may be overcome by using arrays of microelectrodes; however, present microelectrode technology does not allow the combined high spatial and temporal resolution that is possible with microscopy. Spatially resolved measurements of release, such as those possible with imaging techniques, may be a useful complement to single-point measurements to facilitate probing spatial organization of secretion.

Recent advances in fluorescence imaging have resulted in several new approaches for monitoring exocytosis that may be applicable to pancreatic β-cells. Styryl dyes, such as FM 1-43, which display enhanced fluorescence when partitioned into cellular membranes, allow detection of membrane area changes associated with exocytosis and endocytosis (Smith and Betz, 1996). In addition, individual vesicles can be detected and their intracellular movements tracked by labeling secretory vesicles either with dyes that accumulate into acidic vesicles (Steyer et al., 1997) or with the fusion of green-fluorescent proteins to naturally occurring vesicular proteins (Kaether et al., 1997; Levitan, 1998; Pouli et al., 1998). Native fluorescence imaging by UV or multiphoton excitation has also been used to detect intracellular levels of certain hormones such as serotonin or catecholamines (Maiti et al., 1997; Tan et al., 1995; Lillard and Yeung, 1997; Tong and Yeung, 1998; Parpura et al., 1998; Yeung, 1999). Changes in intracellular fluorescence corresponding to secretion of the compounds have been detected (Tan et al., 1997; Lillard and Yeung, 1997; Tong and Yeung, 1998; Parpura et al., 1998; Yeung, 1999).

As a complement to these fluorescence imaging techniques, imaging secretion at β-cells has been explored by direct detection of endogenous Zn^{2+} efflux from single pancreatic β-cells. Insulin is stored in secretory vesicles as a solid hexamer bound with two Zn^{2+} per hexamer (Blundell et al., 1972; Emdin et al., 1980; Gold and Grodsky, 1984; Foster et al., 1993) so that during exocytosis the Zn^{2+}-insulin complex dissolves and dissociates co-releasing free Zn^{2+} and insulin (Aspinwall et al., 1997; Formby et al., 1984; Grodsky and Schmid-Formby, 1985). Detection of Zn^{2+} efflux, therefore, could allow secretion in the β-cell to be monitored. Zn^{2+} is an attractive target for fluorescent measurements because several Zn^{2+}-specific fluorogenic dyes have already been developed. In this work, Zinquin [(2-methyl-8-p-toluenesulphonamido-6-quinolyloxy) acetic acid], a dye that chelates Zn^{2+} with a dissociation constant (K_d) of ~370 nM and enhances its fluorescence by 20-fold upon binding to Zn^{2+} (Zalewski et al., 1993, 1994), is used with the confocal laser-scanning fluorescence microscopy to image Zn^{2+} released by exocytosis. This is the first example of using fluorescence microscopy to detect extracellular concentration changes associated with secretion. Imaging of Zn^{2+} efflux reveals that β-cell secretion is frequently constrained to only a portion of the cell, suggesting spatial organization of secretion machinery within the cell.

Experimental

Chemicals

Zinquin and its ester form (Zinquin ester) were synthesized and characterized according to an established protocol (Mahadevan et al., 1996). Type XI collagenase, HEPES, 5-hydroxytryptophan (5-HTP), digitonin, and carbachol were purchased from Sigma and used without further purification. FM 1-43 was purchased from Molecular Probes. Unless otherwise stated, all chemicals for islet and cell culture were obtained from Life Technologies. All other chemicals for buffers and stimuli were from Fisher unless noted.

Isolation and *In Vitro* Culture of Mouse β-cells

Pancreatic islets were isolated from 20-35 g CD-1 mice. Prior to isolation, Ca^{2+}-free Hanks' Balance Salt Solution (HBSS) containing 136 mM NaCl, 5.4 mM KCl, 1.0 mM $MgCl_2$, 0.41 mM KH_2PO_4, 0.41 mM NaH_2PO_4, 10 mM HEPES, 5.0 mM D-glucose was prepared and its pH was adjusted to 7.4 with NaOH. Ca^{2+}-containing HBSS was made by adding $CaCl_2$ to a final concentration of 1.26 mM $CaCl_2$. Both solutions were filtered with sterile, 0.22 μm pore size, bottle top membrane filter (Nalgene). Immediately before animal surgery, enzyme solution was prepared by dissolving Type XI collagenase (0.7 mg/mL) in Ca^{2+}-free HBSS. All solutions were stored on ice during isolation.

Mice were sacrificed by anesthesia in a desiccator using halothane followed by cervical dislocation. Following dissection, the enzyme solution was injected into the pancreatic duct through a sterile syringe. Approximately 2-5 mL was injected for each mouse. Following injection, the distended pancreas was removed and placed into a 20 mL scintillation vial that has been siliconized (Sigmacote) and sterilized prior to use. Approximately 5 mL of enzyme solution was added to the vial and the vial was then placed into a water bath incubating for 12-14 min at 37° C. Following incubation, the vial was filled with ice-cold Ca^{2+}-free HBSS and shaken vigorously for 30 s. The resulting suspension was transferred to a sterile, 50 mL centrifuge tube. The islet tissue in the tube was then washed with Ca^{2+}-containing HBSS 6-8 times. Following the washing steps, the islets were transferred to a 60 mm culture dish and handpicked using a 10-100 μL Eppendorf pipet with sterile tips under a dissecting microscope. The picked islets were transferred to another culture dish with fresh RPMI 1640 medium containing

10% fetal bovine serum (FBS), 100 U/mL penicillin and 100 μg/mL streptomycin. The islets were then incubated in RPMI 1640 in a humidified incubator at 37° C, 5% CO_2, pH 7.4 until use for dispersion into single cells.

For dispersion into single cells, approximately 100-150 islets were transferred into a 15 mL sterile centrifuge tube. The medium was removed following centrifuging and 1 mL warmed 0.025 trypsin was added to the tube. The tube was then shaken gently for 6 min at 37° C in a water bath to disperse the islets into single cells. The trypsin digestion was stopped by adding RPMI medium and the supernatant was removed following centrifuging. Then, approximately 0.04-0.05 mL of RPMI per 15 islets was added to the tube. After mixing well, dispersed cells were plated onto 25 mm coverslips in tissue culture dishes (approximately 0.03 mL per dish). After incubating for 2 h, additional 3 mL RPMI was added to each dish and cells were incubated at 37° C, 5% CO_2, pH 7.4. Cells were used for experiments typically 1 to 2 days following isolation.

Confocal Imaging and Data Analysis

All imaging experiments were performed on a Nikon RCM 8000 laser-scanning confocal microscope, consisting of a Nikon Diaphot 300 invert microscope, a Coherent argon-ion laser (Model 622), associated optics and mechanical units as described in Appendix A. A Nikon 40x, 1.15 NA, UV-corrected water immersion objective was used for all the experiments. With this objective, confocal images were obtained as a ~1 μm thick slice through the cell. The imaging field of view with a 40x objective is 150 μm, corresponding to ~0.3 μm/pixel in both X and Y directions with a 512 × 486 pixel image. A full X-Y laser scan requires 33.3 ms (X-Y scans completed at 30 Hz), which yields a dwell-time for a single pixel of ~135 ns. A full X-Y scan is defined as one frame, so the frame acquisition rate of this system is 30 Hz for full frame scanning. Typically a number of frames will be averaged to reduce noise in the images. Thus, an image acquisition time of 266 ms corresponds to averaging 8 frames collected at 30 Hz.

Zinc images were taken with 351 nm excitation and 480 ± 10 nm band-pass emission filters. The typical excitation power used for Zn^{2+} imaging was 70-150 μW. FM 1-43 images were acquired using 488 nm excitation and 595 nm long-pass emission filters. All images were stored on an optical disc cartridge (TQ-FH332, Panasonic) by an optical disc recorder (TQ-3038F, Panasonic). For analysis, images were played back from the optical disk cartridge and captured and analyzed using Simca image analysis software (C-IMAGING Systems). For plots of fluorescence as a function of time, regions of interest (ROI) around cells were highlighted and average intensities within the ROIs were plotted by Simca during playback of images. Ratio images were generated by the RCM software in the confocal system.

Cells to be imaged were bathed in Krebs-Ringer buffer (KRB), pH 7.4 containing 118 mM NaCl, 5.4 mM KCl, 2.4 mM $CaCl_2$, 1.2 mM $MgSO_4$, 1.2 mM KH_2PO_4, 20 mM HEPES, 3.0 mM D-glucose and maintained at 37° C on the stage of the microscope by a microincubator (Medical Systems, Inc.). For intracellular Zn^{2+} measurements, cells were loaded with 15 μM Zinquin ester in RPMI medium for 30 min at 37° C and washed with dye-free KRB twice. For extracellular Zn^{2+} measurements, cells were bathed in KRB containing 10 μM Zinquin (acid form). For FM 1-43 experiments, the bathing buffer contained 1 μM FM 1-43. For Ca^{2+}-dependency experiments, $CaCl_2$ in the KRB was replaced by the same concentration of $MgCl_2$. Secretagogues and control KRB were applied to individual cells by pressure ejection at 3-6 psi from micropipettes positioned

~60 μm from the cells (Aspinwall et al., 1997). The pressure ejections were performed using a multi-channel Picospritzer (General Valve Corporation). Stimulants (30 mM K^+, 20 mM glucose, 200 μM carbachol or 20 μM digitonin) were dissolved in solutions identical to the buffer that cells were bathed in. For the K^+ stimulating solution, the NaCl was decreased by 30 mM to maintain ionic strength. For digitonin stimulation, extracellular Ca^{2+} was reduced to 0.2 mM. For controls, the identical buffer minus the stimulant was applied to the cell from a different pipette.

Simultaneous Fluorescence and Amperometric Measurements

Cells used for simultaneous measurements were loaded with 5-HT by incubating in RPMI medium containing 0.5 mM 5-HTP for 16 h at 37° C in 5% CO_2, pH 7.4 (Aspinwall et al., 1997). The 5-HTP is enzymatically converted to 5-HT once it enters the cell. After loading, cells were treated as for the fluorescence measurements.

Two types of carbon fiber microelectrodes were used to monitor the release of 5-HT. One type was glass encased carbon fiber disk electrodes with a relatively large glass tips (total diameter ~30 μm), the other was flame-etched, polymer coated carbon fiber electrodes with tip diameter 1~3 μm. The glass encased carbon fiber disk electrodes were constructed as described previously (Kawagoe et al., 1993; Huang et al., 1995). A single 9 μm carbon fiber (P-55S, Amoco Performance Products) was aspirated into a filamented glass capillary (0.69 mm i.d. × 1.2 mm o.d.). The capillary was then pulled on a Narishige PE-2 pipette puller yielding two electrodes. Electrode tips were cut using a scalpel under a dissecting microscope to generate a tip opening of ~12-15 μm and the carbon fiber was manipulated to extrude ~10 μm from the tip. Cut electrodes were sealed by dipping for 20 s into 3 g of hot epoxy (Epon 828, Miller-Stephenson) containing 0.5 g *m*-phenylenediamine hardener and allowed to cure overnight at room temperature. The following day, electrodes were baked at 100° C for 2 h and then 150° C for 2 h.

The flame-etched carbon fiber electrodes were prepared slightly differently. The glass pipette was pulled and cut at the tip with tip size ~100-300 μm and the carbon fiber was manipulated to extrude ~500 μm from the tip. The extruded portion of the carbon fiber was etched in a Bunsen burner flame into a sub-micron tip (Robinson et al., 1995). The glass tip was then sealed with Sylgard (Corning) and the exposed fiber was insulated by electrochemical polymerization in a phenol, allylphenol solution as previously described (Strein and Ewing, 1992). The polymerization was performed using a two-electrode system, where a platinum wire was used as a counter electrode. During polymerization, a 4.0 V potential vs. the counter electrode was applied to the carbon fiber electrode by a battery for 13 min. The polymer-insulating layer was then cured for 30 min at 150° C. The polymerization solution contained 50% methanol, 50% water, 2% butoxyethanol, 0.14 M 2-allylphenol and 0.06 M phenol and pH was adjusted to 9.0-9.3.

Prior to use, both types of electrodes were polished at a 45° angle using a pipette beveler (BV-10 with 104D polishing wheel, Sutter Instruments). The larger electrodes were positioned over the top of the cell ~1 μm away and to measure secretion from the top face of the cell, while the smaller electrodes directly touched the cell to measure secretion from a small area of cell membrane.

Amperometry was performed using a two-electrode system and a battery to apply -0.65 V to the sodium-saturated calomel reference electrode (SSCE). Current was monitored at the carbon fiber working electrode using an AI-403 current amplifier and CyberAmp 320 programmable signal conditioner (Axon Instruments, Foster City, CA).

Data were low-pass filtered at 100 Hz and collected at 500 Hz using a personal computer (Gateway 2000 P6-266) via a data acquisition board (Digidata 1200B, Axon Instruments). During simultaneous measurements, the UV laser scanning caused fluctuations in the amperometric trace with a frequency that matched the laser scanning (30 Hz). These fluctuations were large enough to obscure all amperometric signals; therefore, the amperometric data were notch-filtered at 30 Hz by a Fourier-filtering software (ts-findn.exe, a data analysis program provided by Prof. R. M. Wightman) to remove this noise.

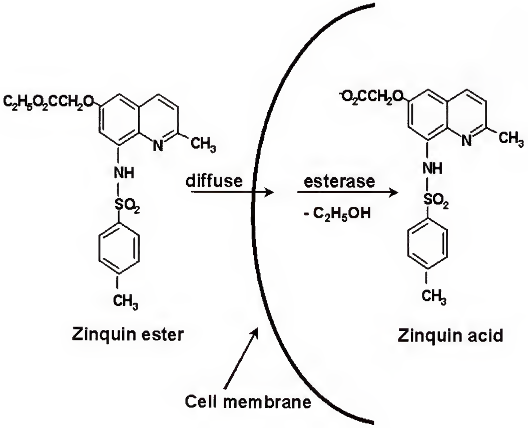

Figure 2-1. Loading of Zinquin into the cell. During loading, cells are incubated in buffer containing Zinquin ester. Zinquin ester diffuses across the plasma membrane and is hydrolyzed by intracellular esterases. The hydrolyzed Zinquin acid is accumulated in the cell due to its negative charge.

Results

Intracellular Zn^{2+} Measurements

Zinquin has previously been used to measure intracellular and intravesicular labile Zn^{2+} (Zalewski et al., 1994; Snitsarev et al., 2001) by incubating cells with the ester form of Zinquin, which crosses the plasma membrane and is hydrolyzed by intracellular esterases to the carboxylate anion (acid form). The cell membrane is relatively impermeable to the acid form of Zinquin, which leads to intracellular accumulation of the dye as illustrated in Figure 2-1. Used in this way at β-cells, stimulation of exocytosis would be expected to cause a decrease in fluorescence intensity as Zn^{2+} is released, similar to what has been observed in Zn^{2+}-containing hippocampal neurons by using TFLZn, a structural analog of Zinquin (Budde et al., 1997). In experiments with this approach, it was found that intracellular fluorescence signals did decrease during stimulation with 200 μM carbachol as shown in Figure 2-2. Although intracellular fluorescence decreases also occurred during application of control buffers to the cell, the decrease, measured as the slope of the time-dependent fluorescence trace, was significantly greater during stimulation than during control or basal conditions. The decreases that occurred during basal or control conditions could be caused by photobleaching of the dye inside the cells or "leaking" of the dye out of the cells. While the intracellular fluorescence decreases during stimulation were significant, it was apparent that such decreases could be caused by other events such as changes in native fluorescence of the cellular content during stimulation and other decreases in intracellular Zn^{2+} level besides those associated with secretion. These confounding factors prevented sensitive and selective measurements of secretion in these cells.

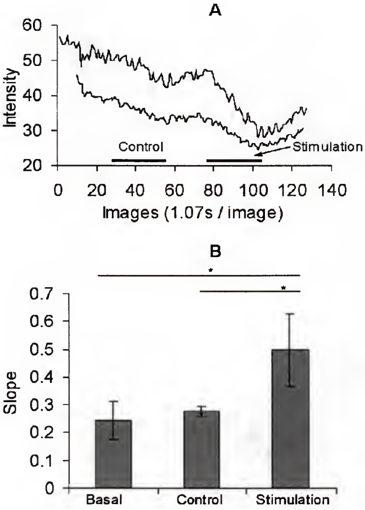

Figure 2-2. Measurements of intracellular Zn^{2+} fluorescence. (A) Intracellular Zn^{2+} fluorescence changes of two different cells. Cells were preloaded with 15 μM Zinquin ester. Images were taken continuously at 1.07 s intervals (32 frame averaged per image). A control buffer and 200 μM carbachol solution were applied for 30 s indicated as the bars underneath the curves. (B) Slopes of fluorescence decrease during three periods, 1) basal (before the application of buffer); 2) control (during the application of buffer); 3) stimulation (during the application of carbachol). Slopes were estimated by linear regression and shown as mean ± standard deviation (S.D., n = 5). Statistical significance of * is $P < 0.05$, which is evaluated by Student's *t* test.

Extracellular Zn^{2+} Measurements with Zinquin Acid

To avoid problems associated with intracellular Zn^{2+} measurements, measurements of extracellular Zn^{2+} concentration changes were explored. For these measurements, the cells were bathed in a solution containing the acid form of Zinquin, which is relatively impermeable to the membrane due to its negative charge at physiological pH, so that Zn^{2+} released from the cell is expected to react with dye resulting in increased fluorescence outside the cell as illustrated in Figure 2-3. This approach is expected to avoid the difficulties of intracellular measurements because intracellular fluorescence does not interfere and photobleached dye can be quickly replaced by dye in the bath.

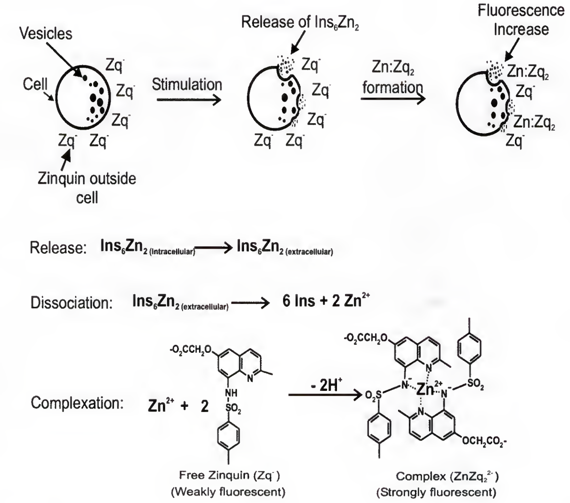

Figure 2-3. Scheme of extracellular measurements of Zn^{2+} efflux. Zn^{2+} co-stored in secretory vesicles with insulin is released by exocytosis. Once exposed to the extracellular milieu, the insulin:Zn^{2+} granule (Ins_6Zn_2) dissolves and dissociates allowing the Zn^{2+} to react with Zinquin acid (Zq^-) to form a fluorescent complex. The detailed sequence of reactions is shown below.

In preliminary experiments, the permeability of cell membrane to Zinquin acid was tested. The relative fluorescence intensities of the cells with no exposure to dye, exposure to 10 μM Zinquin acid, and exposure with 15 μM Zinquin ester for 30 min are compared in Figure 2-4. As expected, the intensity of cells incubated in a buffer containing Zinquin acid is much lower than the cells exposed to Zinquin ester, but is higher than that of autofluorescence. This result indicates that Zinquin acid can permeate the membrane at pH 7.4; however, the permeability is relative low compared to Zinquin ester.

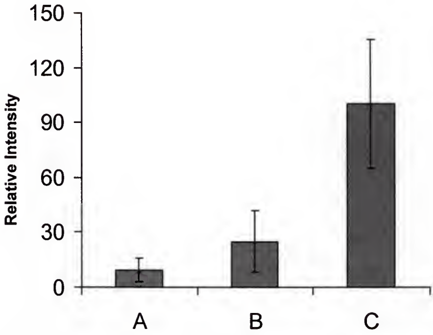

Figure 2-4. Comparison of autofluorescence and Zn^{2+} fluorescence in cells. The relative fluorescence intensities are averages of 15 cells. The error bars shown are ± S.D. (A) Cellular autofluorescence in absence of Zinquin. (B) Cells were bathed in KRB containing 10 μM Zinquin acid. (C) Cells were loaded with 15 μM Zinquin ester.

Figure 2-5 illustrates images of a single cell stimulated with 20 mM glucose in the presence of Zinquin. The images are shown in relative fluorescence intensity ratios against the first image collected in the series in order to highlight the fluorescence changes. The images show that fluorescence dramatically increased at the surface of the cell, primarily in a semi-circular region covering about 50% of the circumference, following the glucose stimulation. The extracellular fluorescence enhancement was not observed in control experiments where the cell was stimulated with KRB (Figure 2-5 B and 2-6). The dynamic changes in fluorescence intensity can be analyzed by drawing ROI around the cell as shown in Figure 2-6. The fluorescence intensities were plotted as a function of time for both outside and inside the cell. With both control and glucose application, fluorescence inside the cell decreased, which may be due to decrease of native cellular fluorescence or Zinquin fluorescence from a small amount of Zinquin that permeated the cell (Figure 2-6). The example shown above is representative of 22 separated experiments.

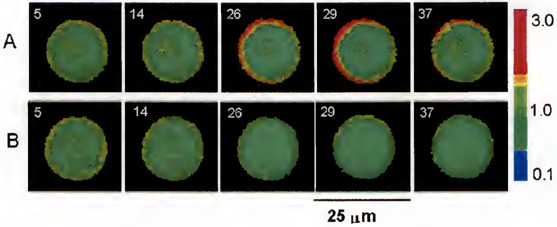

Figure 2-5. Extracellular measurements of Zn^{2+} release. Images are shown in fluorescence intensity ratios against a reference image collected at the beginning of each series. Cells were bathed in KRB containing 10 μM Zinquin acid. Scans were taken continuously and 64 frames were averaged per image (2.13 s per image). The number of each image acquired in the entire series is indicated. (A) Glucose stimulation where 20 mM glucose was applied to the cell by a micropipette (stimulus applied from image 15 to image 29). (B) Control experiment where control solution was applied to the cell by a micropipette (stimulus applied for the same period as (A)).

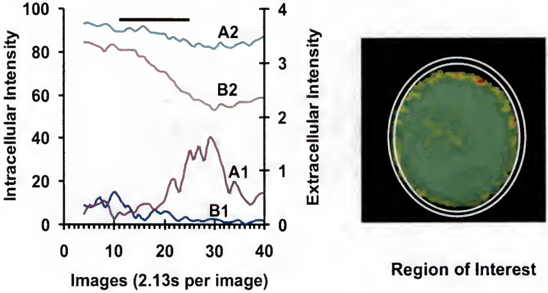

Region of Interest

Figure 2-6. Average fluorescence intensities within regions of interest (ROIs) as a function of time. Images used for analysis were same as in Figure 2-5. The ROI were defined by drawing two circles around the cell as shown in the image. The inner circle defines the region inside the cell. The region between the two circles defines the region outside the cell. A1, B1 are extracellular fluorescence for glucose and control stimulation, respectively. A2 and B2 are intracellular fluorescence for glucose and control stimulation, respectively. Stimulation periods are indicated by the bar above the traces.

To test the hypothesis that increases in fluorescence outside the cell were due to the detection of Zn^{2+} efflux, control experiments were performed in which a cell was stimulated in the presence of tetrakis-(2-pyridylmethyl)ethylenediamine (TPEN), a non-fluorescent Zn^{2+} chelator with higher affinity for Zn^{2+} than Zinquin (Arslan et al., 1985). In these experiments, no fluorescent changes occurred outside the cells even though the same cells exhibited strong signals in the absence of TPEN as illustrated in Figure 2-7 (n = 4). Thus, the signals observed were dependent upon the presence of free Zn^{2+} outside the cell. In addition, no extracellular fluorescence changes were observed in the absence of Zinquin. Finally, the fluorescence changes were not due to the cells moving or membrane swelling as indicated by visual inspection and imaging of the membrane with

FM1-43 during stimulation. The images shown in Figure 2-5 are intensity ratios against the first image of the series. Thus, if the cell moved, then one side of the ratio image would show a decrease in fluorescence (blue color) and the opposite side would show enhanced fluorescence (red color); however, as shown in the figure the side opposite the increase in fluorescence did not give a depression of fluorescence. (When cells are not adhered well to the plate, such artifacts can be observed.) In addition, observations made when the cells were treated with FM 1-43, a styryl dye that fluoresces when partitioned into the cell membrane, support this conclusion. Taken together, these results support the hypothesis that the fluorescent signals observed were due to Zn^{2+} efflux from the cell.

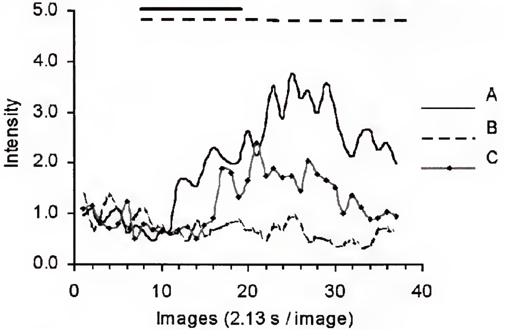

Figure 2-7. Effects of TPEN on detection of Zn^{2+} efflux. Images were acquired and analyzed as in Figure 2-5 and 2-6 and intensity was normalized against the first image in each series. Traces were recorded from the same cell, which was bathed in KRB with 10 μM Zinquin acid. (A) Stimulation with 20 mM glucose (solid bar). (B) Stimulation with solution containing 20 mM glucose and 50 μM TPEN after a 5-min interval (dashed bar). (C) Stimulation with 20 mM glucose again after 5 min. A longer stimulus was used with (B) to maintain TPEN around the cell during the course of secretion.

Correlation between Zn^{2+} Efflux and Exocytosis

The initial observations of Zn^{2+} efflux from single cells evoked by glucose led us to develop the hypothesis that detected Zn^{2+} corresponded to Zn^{2+} co-released with insulin by exocytosis. This hypothesis was tested by using other insulin secretogogues, Ca^{2+}-free experiments, simultaneous amperometric and fluorescence measurements of secretion, and measurements with higher temporal resolution.

Other insulin secretagogues. Similar to the measurements with glucose shown above, treatment of cells with either 30 mM K^+, a depolarizing agent, or 200 μM carbachol, a secretagogue that releases intracellular Ca^{2+} stores to induce exocytosis, caused increases in extracellular Zn^{2+} fluorescence as illustrated in Figure 2-8A. Clear spatial heterogeneous Zn^{2+} release such as that shown in Figure 2-5 was observed in 80% of cells for all insulin secretagogues (n = 58). The active area of Zn^{2+} release typically covers 40-60% of the plasma membrane area and the locations of the active area vary from cell to cell. In most cases, it was observed that extracellular fluorescence enhanced 5-fold or more over basal during stimulation. It has been difficult to quantitate the magnitudes of Zn^{2+} release because the measurements of extracellular signals depend on how the extracellular region is defined (for example, see Figure 2-6). The variation of excitation power and detection efficiency will also affect the magnitudes of the responses. The latency for initiation of Zn^{2+} release and the duration of observed Zn^{2+} release were compared to the corresponding latency and duration of current spikes observed from amperometry detection of 5-HT secretion from single cells (Table 2-1). As shown, the latencies and durations measured by these two techniques agree well. Different latencies were observed for different stimuli using both methods. For example, while K^+ evoked an instantaneous increase in Zn^{2+} release, glucose-induced Zn^{2+} release was delayed with an average latency of 11 s. These differences can be attributed to different mechanisms of inducing release, i.e. K^+ causes an instant depolarization of the cell membrane while glucose induced depolarization only occurs after sufficient metabolism to generate the necessary secondary messengers.

Table 2-1. Comparison of the latency and duration of Zn^{2+} secretion and 5-HT secretion.

Stimuli	Latency (Zn^{2+}) (s)	Latency (5-HT) (s)	Duration (Zn^{2+}) (s)	Duration (5-HT) (s)
K^+	1 ± 2 (n = 8)	0.7 ± 0.6 (n = 8)	34 ± 6 (n = 8)	35.1 ± 8.4 (n = 8)
Carbachol	4 ± 3 (n = 15)	2.3 ± 1.8 (n = 9)	40 ± 6 (n = 15)	38.2 ± 8.4 (n = 9)
Glucose	11 ± 5 (n = 14)	7.0 ± 4.0 (n = 6)	44 ± 9 (n = 14)	47.1 ± 8.9 (n = 6)

*All images of Zn^{2+} release were acquired with a rate of 2.13 s per image and all stimulations were applied for 30 s. Amperometric and fluorescence measurements were performed independently. All means of the latencies and durations of Zn^{2+} efflux and 5-HT secretion are not statistically different as tested by student's *t* test.

While all insulin secretagogues induced Zn^{2+} efflux as expected for the co-release of insulin and Zn^{2+} from β-cells, intracellular fluorescence changes observed were also stimulant dependent. As shown in Figure 2-8B, K^+ caused delayed increase in intracellular fluorescence, whereas the other stimuli caused gradual decreases during stimulation. These results suggest that in addition to depolarizing the membrane, K^+ either increases intracellular Zn^{2+} fluorescence by inducing release of intracellular Zn^{2+} stores or uptake of Zinquin acid, or increases the cell autofluorescence. It is not clear why these differences should occur; however, these results further highlight the impracticality of using intracellular Zn^{2+} changes as a measure of release with Zinquin.

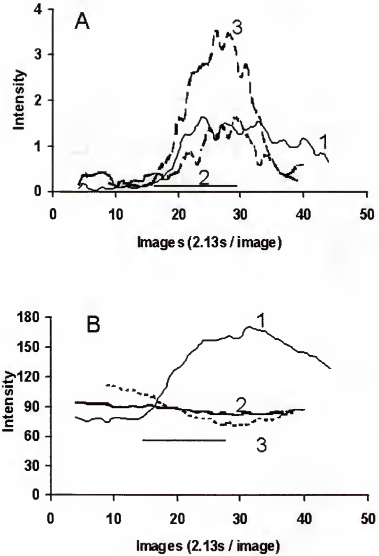

Figure 2-8. Zn^{2+} release induced by different insulin secretagogues. (A) Extracellular fluorescence. (B) Intracellular Fluorescence. Images were acquired and analyzed as in Figure 2-6. Stimuli used were 30 mM K^+ (1), 20 mM glucose (2), and 200 μM carbachol (3). The bar under traces indicates the stimulation period. Traces for different stimuli were not from the same cell. Results are representative for at least ten separate experiments for each stimulant.

Ca^{2+}-dependency of Zn^{2+} efflux. For glucose or K^+ stimulation, insulin secretion is dependent on the presence of extracellular Ca^{2+}. To verify the association of Zn^{2+} release with insulin secretion, Zn^{2+} release due to glucose and K^+ stimulation was measured in a Ca^{2+}-free medium. As expected, the increases in Zn^{2+} fluorescence induced by these secretogogues were dependent upon having Ca^{2+} in the extracellular medium (Figure 2-9).

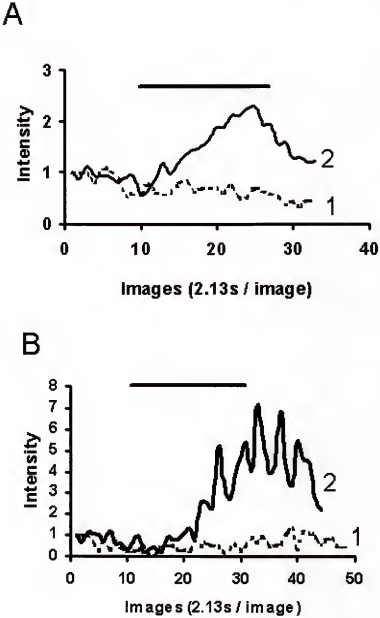

Figure 2-9. Ca^{2+}-dependency of Zn^{2+} efflux. Traces were recorded from the same cell, which was bathed in Ca^{2+}-free KRB containing 10 μM Zinquin acid. The cell was first stimulated by Ca^{2+}-free stimulant (1) and then stimulant containing 2.4 mM Ca^{2+} (2) 5 min after the first stimulation. The bar on the top in each graph indicates the stimulation period. (A) 30 mM K^+ stimulation (n = 3); (B) 20 mM glucose stimulation (n = 5).

Simultaneous amperometric and fluorescence measurements. To further explore the apparent correlation between Zn^{2+} secretion and exocytosis, we attempted simultaneous fluorescence measurements of Zn^{2+} and amperometric measurements of 5-HT secretion at the same cell. (Amperometric detection of 5-HT has been shown to correspond to exocytosis of insulin secretory vesicles at pancreatic β-cells (Aspinwall et al., 1999b)). These measurements were technically difficult for several reasons. First, the electrode blocked observation of Zinquin fluorescence at the cell membrane in the immediate vicinity of the electrode because of the high fluorescence background caused by the electrode; therefore, Zn^{2+} release could not be measured at exactly the same location as 5-HT secretion. Furthermore, the laser scanning induced extremely large current fluctuations in the amperometric measurements due to photoelectric effect of UV laser light (Robinson et al., 1995). As shown in Figure 2-10, large electric noise was observed due to UV laser scanning, which could potentially block the current spikes corresponding to the detection of 5-HT secretion. After examining the frequency of the amperometric trace using a Fourier transform, it was found that the major noise follows a 30 Hz pattern and it can be largely removed using a 30 Hz notch filter (Figure 2-10). The frequency of noise is same as the laser-scanning rate of the confocal system, which uses a raster-scanning mode with each pixel exposed to laser illumination 30 times per second. However, even after Fourier filtering, the noise level in the amperometric measurements was still higher than what was typically achieved. Despite these limitations, it has been possible to simultaneously observe both Zn^{2+} efflux and 5-HT secretion from the same cell using either small electrodes that only covered a portion of the cell membrane (Figure 2-11A) or larger electrodes that covered the top face of the cell (Figure 2-11B).

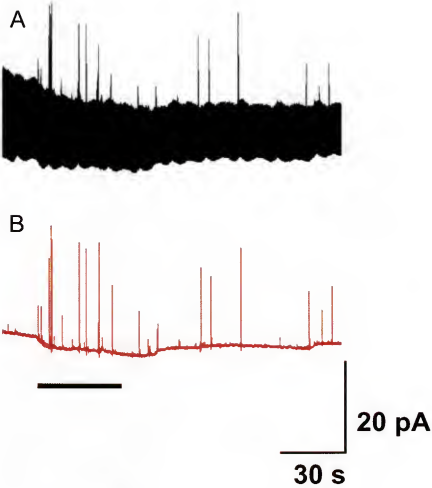

Figure 2-10. Photoelectric noise induced by UV laser scanning. 5-HT secretion from a single cell was monitored by amperometry with a 9 μm diameter carbon fiber microelectrode. The cell was continuously scanned with 351 nm laser line by the confocal system. The cell was stimulated with 30 mM K^+ for 40 s as indicated by the bar under the traces. (A) Amperometric current trace before Fourier filtering. (B) Trace after Fourier filtering with a 30 Hz notch-filter.

If fluorescence was measured in the immediate vicinity of the electrode, the fluorescence and amperometric signals (amperometric signals are current spikes corresponding to detection of bursts of 5-HT released by exocytosis) began and ended in tandem as shown by the pink trace in Figure 2-11A (n = 4). Interestingly, if fluorescence around the whole cell was analyzed, a poorer correlation with the fluorescence signal lasting 2-10 s longer than the amperometric spikes was observed (see black trace in

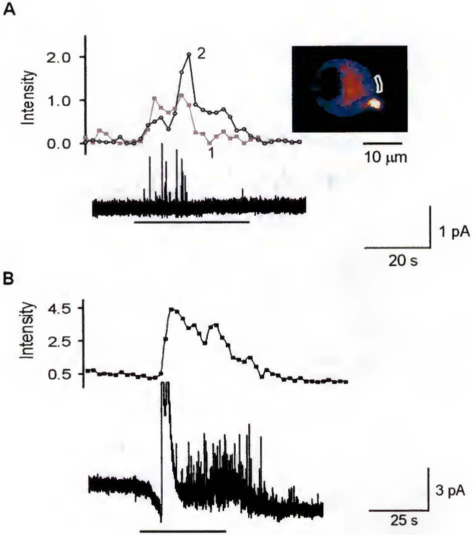

Figure 2-11. Simultaneous fluorescence and amperometric measurements. Images were acquired as in Figure 2-5. Fluorescence and amperometric traces are aligned on the same time axis for a given experiment and bars underneath traces indicate the periods of stimulation. Amperometric traces shown were notch-filtered at 30 Hz. (A) K^+ stimulation during which 5-HT secretion was monitored using a carbon fiber electrode with ~3 μm tip diameter. The inset image is a FM 1-43 labeled cell image. The relatively bright area in the lower right corner indicates the position of the electrode. Fluorescence trace 1 (pink) is the fluorescence intensity measured in a region close to the electrode and indicated by the white outline on the image. Fluorescence trace 2 (black) is obtained from the extracellular region around the entire cell, as in Figure 2-6 (excluding the electrode). (B) Digitonin stimulation during which a carbon fiber electrode with total tip diameter of 30 μm was positioned over the top of the cell. Extracellular fluorescence was measured in an optical section below the electrode. Fluorescent data was from the entire circumference of the cell and presented as in Figure 2-6.

Figure 2-11A). The requirement of detecting fluorescence near the electrode to obtain a good correlation between the Zn^{2+} and 5-HT signals is attributed to the spatially heterogeneous nature of the Zn^{2+} release (Figure 2-5). As a complement to these positive correlations, it has also been observed that if the electrode was positioned around a zone of a cell that did not exhibit Zn^{2+} efflux, no 5-HT secretion was observed ($n = 5$).

Further correlations were attempted using a 9 μm diameter electrode, which could be positioned over the top of the cell and measure release from the entire top face of the cell. When using electrodes of this dimension, good correlations between the onset of 5-HT detection and Zn^{2+} detection were also achieved as illustrated in Figure 2-11B for a digitonin treatment (digitonin induces secretion by permeabilizing the membrane allowing Ca^{2+} entry and stimulation of exocytosis). Here, digitonin was used because it induces relatively large amount of release of insulin granules and gives better signal-to-noise ratio (S/N) for simultaneous measurements. For simultaneous measurements, secretion was observed at 21 different cells using K^+ ($n = 3$), glucose ($n = 8$), carbachol ($n = 6$) or digitonin ($n = 4$) as the stimulant. In all cases, fluorescence and amperometric signals began and ended at the same time within the temporal resolution of the fluorescence measurements.

Measurements of Zn^{2+} efflux with high temporal resolution. If Zn^{2+} release is primarily due to exocytosis, then it would be expected to detect sharp fluctuations in Zn^{2+} concentration near the membrane if the temporal resolution of the measurement was high enough. Most of the images that were collected were acquired at a rate of 2.13 s per image (64 frames averaged per image), which provides clear images but is too slow to observe isolated exocytotic events. To attempt detection of such fluctuations, Zn^{2+}

secretion from cells was measured with image acquisition rates of 4 Hz (8 frames averaged per image). An example of Zn^{2+} efflux measured under these conditions following carbachol stimulation is shown in Figure 2-12. With this rate of image acquisition, the detection limit was estimated to be 0.5 μM (S/N of 3). The montage of images in Figure 2-12A show that during the course of stimulation, strong increases in fluorescence are observed immediately outside the cell and these signals end soon after the stimulation. As with images obtained at lower temporal resolution, Zn^{2+} release is heterogeneous across the surface of the cell with some portions of the cell not generating any signals and others generating nearly continuous signals.

Another feature of the data is that fluorescence measured in small locations on the cell surface occurs in bursts, which is expected if Zn^{2+} is released in packets from individual secretory vesicles by exocytosis (Figure 2-12B). These temporal plots from different parts of the cell further illustrate the highly localized nature of the release. Individual fluorescence bursts have the time courses expected for detection of exocytotic events. In amperometric measurements of insulin release by exocytosis, it has been previously observed that individual current spikes corresponding to the detection of individual exocytotic events had a full-width at half height of 37 ± 27 ms and total duration of 270 ± 165 ms (Kennedy et al., 1996). Based on these observations, Zn^{2+} bursts, if due to single exocytosis events, would be expected to occur within a period of one or two images at 266 ms/image. Indeed, 50% of the bursts that were detected in these small windows lasted only one image and 34% lasted two images. These burst widths should not be taken to represent the time of exocytotic events because the temporal resolution using this approach is at present too poor to adequately sample the spikes or to resolve multiple bursts occurring within a single image. Higher temporal resolution will be required to adequately characterize the spike widths and correlate these fluorescence bursts to isolated exocytotic events. These data simply show that the spikes are narrow enough, within the temporal resolution of the measurements, to be caused by exocytotic release events. The signals observed in Figure 2-12 are typical of experiments at seven different cells.

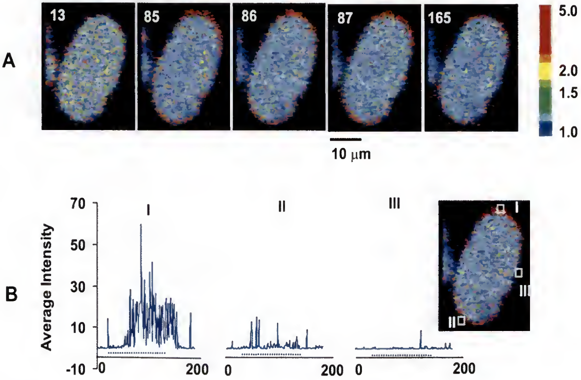

Figure 2-12. Measurements of Zn^{2+} release with images acquired continuously at 266 ms/image (8 frames averaged/image). (A) Montage of 30 × 40 μm ratio images. Images are shown in intensity ratios against the first image in the entire series and the image number is indicated. Images actually show two cells that are connected with touching each other resulting in the oblong shape. Cells were stimulated with 200 μM carbachol from images 30 to 143. Image 13 is a typical image before stimulation. Images 87-89 are a typical series during stimulation and image 160 is a typical image after stimulation. The color bar is indicative of fluorescence ratios against the first image so that the red color at the edge of the cells indicates fluorescence increases corresponding to the detection of Zn^{2+} release. (B) Zn^{2+} release signals measured in three small extracellular regions (4.3 μm^2) as shown in the inset image. Bars underneath each trace indicate application of 200 μM carbachol.

Discussion

Measurement of Zn^{2+} Efflux

The results clearly show that Zn^{2+} efflux can be detected as a decrease in fluorescence within cells loaded with Zinquin ester or an increase in extracellular fluorescence around cells exposed to Zinquin acid. The former approach suffers from several limitations. Most importantly, the large, changing background due to photobleaching of accumulated dye or leakage of the dye results in poor sensitivity. Furthermore, other intracellular changes in Zn^{2+} concentration or autofluorescence, while potentially quite important, confound interpretation of the results as secretion. Perhaps with appropriate optics such as evanescent wave excitation, it may possible to view only vesicular Zn^{2+} and obtain results similar to what has been achieved with other dyes and vesicular labels (Steyer et al., 1997; Rutter, 1999). With the system used here, however, the extracellular measurements were considerably more useful for monitoring secretion for several reasons. First, photobleaching is a minor factor since the laser only illuminates a small region within a relatively large volume of dye solution, therefore, any degraded dye can be rapidly replaced with fresh dye by diffusion. Second, since fluorescence is generated only after Zn^{2+} is released and then reacts with Zinquin, the measurement is made on a low fluorescent background, which aids sensitivity and allows higher resolution measurements to be made.

Correlation with Insulin Secretion

The Zn^{2+} efflux detected extracellularly appears to correspond primarily to Zn^{2+} co-released with insulin by exocytosis as evidenced by the following: 1) signals were induced only by insulin secretagogues in the presence of extracellular Ca^{2+}, 2) enhanced extracellular fluorescence occurs over a time course that matches that for secretory activity as measured by amperometry, and 3) the release of Zn^{2+} occurs in bursts on the time scale expected for exocytotic events.

Active Areas of Secretion and Compound Exocytosis

These initial observations of monitoring Zn^{2+} release reveal several interesting features of β-cell secretory activity. The images collected clearly show heterogeneity in release around single cells. In 80% of the cells that were studied, secretion occurred over 60% or less of the circumference of cell being observed. Previously, several lines of evidence supporting the idea that β-cells are spatially heterogeneous with respect to exocytosis have been reported. For example, electron microscopic studies have revealed that vesicles in β-cells tend to congregate on one side of cells (Bonner-Weir, 1988). In addition, ratio imaging of intracellular Ca^{2+} concentrations has shown that Ca^{2+} increases primarily in certain portions of the cells suggestive of organization of Ca^{2+} channels. These regions were co-localized vesicles detected by quinacrine fluorescence (Bokvist et al., 1995). The physiological significance of spatially heterogeneous release is not clear; however, it has previously been suggested that since within an intact islet the β-cells are oriented with one side facing the blood vessels, then preferential insulin secretion from the side facing the blood vessels would be an efficient route of secretion. The physiological basis of heterogeneous release is also unclear. This heterogeneity may be due to heterogeneity in the Ca^{2+} channel distribution, vesicles, or other aspects of the exocytotic machinery. These results raise the interesting question of how the cell maintains this organization under culture conditions.

The measurements at small portions of the cell with high temporal resolution are also interesting. These measurements show that a large number of exocytotic events can occur from a small space. For example, in Figure 2-12B, 38 peaks or exocytotic events are detected within 40 s. (It is important to realize that the number of spikes detected is a low estimate of the number of exocytotic events since multiple events could occur in the time to collect one frame and be averaged together.) Given that the β-cell secretory vesicles are ~300 nm in diameter (Larsson et al., 1976), the large number of exocytotic events detected from such a small spot is remarkable and suggests that the cells possess a mechanism for generating exocytosis from a small area of cell membrane. A possible explanation for such locally intense exocytosis is compound exocytosis (Paras et al., 2000). In this mode of release, once a vesicle fuses with the plasma membrane, other vesicles deeper in the cell fuse with the fused vesicle forming deep invaginations within the cell. Previous evidence for compound exocytosis has been obtained using electron microscopy at β-cells, which has revealed trains of vesicles fused together at one point on the cell membrane (Orci and Malaisse, 1980). Such a mode of release would allow the cell to release large amounts of target into one direction and at one spot. Given the discussion above, this may be a means of releasing primarily into the blood stream.

Extracellular Detection of Zn^{2+} Release

As a technique for monitoring secretion, the extracellular confocal measurements offer several advantages. As already shown, the measurements are sensitive enough to detect fluctuations due to exocytosis with spatial resolution. In addition, the method allows multiple cells to be observed simultaneously for detection of cellular heterogeneity in responses. This is illustrated by the images in Figure 2-13, which shows simultaneous detection of heterogeneous Zn^{2+} release from three individual cells. Such an approach may be useful for studying communication between cells. For instance, β-cells are believed to synchronize their secretion within an islet and such an approach may allow detection of synchronization between cells as it occurs.

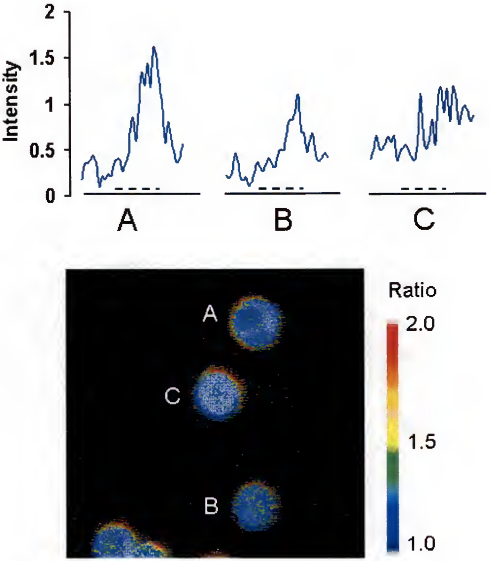

Figure 2-13. Simultaneous observation of Zn^{2+} release from individual cells within the same imaging field. Images were acquired and shown in intensity ratios as in Figure 2-5. Responses of Zn^{2+} release from cell A, B, and C were analyzed as a function of time using regions of interest drawn outside the cells as in Figure 2-6. Cells were stimulated by 20 mM glucose for 30 s as shown by the dash lines under the traces. Each solid line under the traces represents the recording period of 90 s.

In this paper, Zinquin was used to monitor Zn^{2+} efflux as a means of detecting secretory activity at pancreatic β-cells; however, detection of Zn^{2+} release itself may be of interest. Zn^{2+} itself may exert auto-regulatory role in the β-cell insulin secretion by at least three different mechanisms. Zn^{2+} can inhibit glutamate NMDA receptors, which have been found on β-cells (Molnar et al., 1995) and therefore inhibit the release of insulin induced by glutamate. Also, it has been demonstrated that Zn^{2+} activates ATP-sensitive K^+ channels on β-cells and therefore may serve an auto-regulatory role in secretion (Bloc et al., 2000). Furthermore, it has been recently demonstrated that insulin released by β-cells can activate insulin receptors on β-cells and enhance secretion by positive feedback (Aspinwall et al., 1999a). This positive feedback can be inhibited by Zn^{2+}, which complexes the insulin (Aspinwall, et al., 1997). Therefore, further measurements of Zn^{2+} secretion and levels may be important in characterizing the potential role of Zn^{2+} in regulating insulin secretion. Besides its potential effect on the β-cell, Zn^{2+} release may play an important role in neurons such as the hippocampal mossy fibers. In these cells, Zn^{2+} appears to act as a neurotransmitter or neuromodulator and its release play a role in development of Alzheimer's disease as well as excitotoxicity (Huang, 1997; Cuajungco et al., 1997). Therefore, the ability to monitor Zn^{2+} efflux in neuronal systems may also be beneficial in the uncovering the role of Zn^{2+}.

Conclusion

It has been demonstrated that Zn^{2+} efflux from β-cells can be imaged using confocal laser-scanning fluorescence microscopy. The data suggest that Zn^{2+} detected is co-released with insulin and sufficient resolution can be obtained to observe discrete fluctuations in Zn^{2+} levels associated with exocytotic events. This technique provides a novel, non-invasive way to image secretory activity at β-cells with high temporal and spatial resolution. The technique revealed that β-cells are spatially heterogeneous in their release pattern and many events can occur rapidly in a small space suggestive of compound exocytosis. The approach of monitoring messenger release based on fluorescence changes due to a fluorogenic reaction outside the cells could also be applied to Zn^{2+} efflux from other cell types or to other messengers.

CHAPTER 3

SPATIAL ORGANIZATION OF Ca^{2+} ENTRY AND EXOCYTOSIS IN SINGLE MOUSE PANCREATIC β-CELLS

Introduction

Insulin secretion from pancreatic β-cells is triggered by a rise in intracellular Ca^{2+} concentration ($[Ca^{2+}]_i$) that results from opening of voltage-gated Ca^{2+} channels within β-cell plasma membrane (Ashcroft et al., 1994b); however, the spatial organization of Ca^{2+} channels and release sites on β-cells has not been clearly elucidated. Several lines of evidence have suggested that β-cells are polarized and contain specific plasma membrane domains for insulin secretion (Bonner-Weir, 1988; Orci et al., 1989; Lombardi et al., 1985; Cortizo et al., 1990). In an ultra structural study, distribution of secretory granules in partially degranulated β-cells was shown to be polarized with more granules accumulated in the apical portion of the cell (Bonner-Weir, 1988). Observations of localized Ca^{2+} entry through voltage-gated Ca^{2+} channels on pancreatic β-cells have also been reported (Theler et al., 1992; Gylfe et al., 1991; Bokvist et al., 1995; Martin et al., 1997). In one study, co-localization of $_L$-type Ca^{2+} channels and secretory granules was suggested (Bokvist et al., 1995). Taken together, the evidence leads to the view that β-cell exocytosis may be localized to specific membrane domains and exocytotic release sites may co-localize with Ca^{2+} channels. Nevertheless, direct evidence for localized secretion from pancreatic β-cells is still limited. One reason for this dilemma is that measurements of insulin secretion by current techniques lack spatial information.

Amperometry with microelectrodes has previously been used in an effort to spatially map release sites on single pancreatic β-cells (Paras et al., 2000; Bokvist et al., 2000). The amperometric results indicate that exocytosis is confined to part of the cell membrane; however, since a microelectrode is inherently a single-point sensor, an overall picture of exocytosis from a cell cannot be obtained by this approach. Recently, we have developed a confocal fluorescence imaging approach for spatially resolved monitoring of secretion from β-cells (Chapter 2; Qian et al., 2000). In this approach, Zn^{2+} efflux from β-cells is measured as a marker of insulin secretion because β-cell secretory granules co-store Zn^{2+} and insulin (Blundell et al., 1972; Emdin et al., 1980; Gold and Grodsky, 1984; Foster et al., 1993) and subsequently co-release these species during exocytosis (Qian et al., 2000; Formby et al., 1984; Grodsky and Schmid-Formby, 1985; Aspinwall et al., 1997). To detect Zn^{2+} release, cells are incubated in buffer containing Zinquin, a fluorogenic Zn^{2+}-specific fluorophore (Zalewski et al., 1994), while fluorescence signals are monitored by confocal laser-scanning microscopy. When secretion is evoked, the released Zn^{2+} reacts with Zinquin in the extracellular space to form a fluorescent complex, resulting in fluorescence increases at the sites of release on the cell surface. In preliminary experiments with this technique, secretion from single cells was revealed to be localized to one portion of the plasma membrane indicative of an active area of release (Chapter 2; Qian et al., 2000). In this work, the localized secretion from β-cells was further investigated by comparing the spatial relationship of Ca^{2+} entry and exocytotic release sites on β-cells using a combination of Ca^{2+} imaging and Zn^{2+} imaging during treatment with different insulin secretagogues.

Experimental

Chemicals

Zinquin, 2-methyl-8-*p*-toluenesulfonamido-6-quinolyloxy acetic acid, was synthesized and characterized according to an established protocol (Mahadevan et al., 1996). Type XI collagenase, HEPES, and carbachol were from Sigma and used without further purification. Indo-1 free acid, indo-1 AM, and 4-Br-A23187 were from Molecular Probes. All chemicals for islets and cell culture were obtained from Life Technologies. All other chemicals were from Fisher unless noted.

Cell Culture

Pancreatic islets were isolated from 20-35 g CD-1 mice as described in Chapter 2. Briefly, islets were isolated by ductal injection with type XI collagenase and were dispersed into single cells by shaking in dilute trypsin for 6 minutes at 37° C. Cells were plated onto 25 mm diameter coverslips in tissue culture dishes (Corning) and incubated in RPMI 1640 containing 10% fetal bovine serum, 100 U/mL penicillin and 100 μg/mL streptomycin at 37° C, 5% CO_2, pH 7.4. Cells were used for experiments 1 to 2 days after isolation.

Confocal Imaging

All imaging experiments were performed on a Nikon RCM 8000 confocal laser-scanning microscope. All images were stored on an optical disc recorder (TQ-3038F, Panasonic) for later analysis. Cells to be imaged were bathed in Krebs-Ringer buffer (KRB), pH 7.4 containing 118 mM NaCl, 5.4 mM KCl, 2.4 mM $CaCl_2$, 1.2 mM $MgSO_4$, 1.2 mM KH_2PO_4, 20 mM HEPES, 3.0 mM D-glucose and maintained at 37° C. For imaging of Zn^{2+} secretion, 10 μM Zinquin acid was included in the buffer and the typical excitation power used for Zn^{2+} imaging was 70 – 150 μW. Additional experimental details were the same as described in the Experimental section of Chapter 2.

$[Ca^{2+}]_i$ was measured by dual-emission ratio imaging using the calcium indicator indo-1 as described in Appendix B. Briefly, β-cells adhered on coverslips were loaded with 2 μM indo-1 AM in RPMI 1640 at 37° C, 5% CO_2 for 30 min. Dye solution was then replaced with KRB and coverslip with adherent cells was placed onto a 35 mm coverslip holder for immediate use. Indo-1 was excited at 351 nm and its emissions at two wavelengths 405 and 480 nm were separated by a 450 nm cut-off dichroic mirror and recorded on two separate channels using custom-made band-pass filters (405 ± 10 nm and 480 ± 10 nm) from Chroma Technology. The typical excitation power used for indo-1 imaging was 5-20 μW. The intensities detected at these channels were used to generate ratios and $[Ca^{2+}]_i$ can be estimated from the ratios as previously described (Grynkiewicz et al., 1985). A two-point calibration was performed daily following experiments as described in Appendix B to allow the conversion of ratios to $[Ca^{2+}]_i$

Sequential Measurements of Ca^{2+} Transients and Zn^{2+} Secretion

By loading cells with indo-1 AM and incubating cells in KRB containing 10 μM Zinquin, Ca^{2+} transients and Zn^{2+} secretion from same cell can be sequentially monitored. Ca^{2+} transients were measured first using a relatively low laser excitation power (~10 μW) to reduce the possible photobleaching of indo-1 and minimize fluorescence contributed from Zinquin. Following the Ca^{2+} recording, the excitation power was tuned to ~100 μW and the cells were scanned for ~30 s. This procedure was performed to photobleach the indo-1 loaded inside the cell in order to prevent it from interfering with subsequent Zn^{2+} measurements. Elimination of the indo-1 was confirmed by the stabilization of background fluorescence to reduced levels after the scan. Furthermore, no Ca^{2+} changes could be observed after this procedure, which confirms that the desired effect was achieved. After the intracellular fluorescence intensity stabilized, a second stimulation was applied to the cell and Zn^{2+} release was monitored by recording the extracellular Zinquin fluorescence signals.

Data Analysis

Ratio images were directly generated by software on the RCM system. For analysis, images were played back, captured and analyzed using Simca image analysis software (C-IMAGING Systems). For plots of fluorescence intensity as a function of time, regions of interest (ROI) were highlighted and average intensity within each ROI was calculated for a series of images. For dual-channel images of indo-1, images from each channel were played back independently and average intensities within the ROIs as a function of time were calculated independently for each channel. The intensity ratios were calculated after image playback in Microsoft Excel and converted to $[Ca^{2+}]_i$ according to the calibration equation (Grynkiewicz et al., 1985).

Results

Spatially Localized Secretion from Single β-Cells

As shown in Figure 3-1, secretion from single β-cells was spatially localized to one portion of the plasma membrane for all stimuli tested as indicated by fluorescence increases (red color in ratio images) at one portion of the cell circumference. Of the cells with detectable Zn^{2+} secretion signals due to stimulation (n = 78), 80% showed spatially heterogeneous secretion, which was defined as detectable fluorescence increases occurring over ~50% of the cell circumference. As shown in Figure 3-1A, localized secretion was observed for secretagogues that cause Ca^{2+} entry through voltage-gated Ca^{2+} channels, such as K^+ or glucose, and carbachol that releases Ca^{2+} from intracellular stores (Theler et al., 1992). The degree of spatial heterogeneity of secretion was analyzed as percent of cell circumference that exhibited detectable fluorescence enhancement after stimulation. Using this analysis, the active secretion area of the cells comprised 55 ± 14% (n = 11), 49 ± 17% (n = 11), and 53 ± 16% (n = 24) of the total cell circumference for 40 mM K^+, 20 mM glucose, and 200 μM carbachol stimulation, respectively. Thus, no significant difference in the size of active areas between different insulin secretagogues was observed.

To determine if the active secretion area of a cell remained fixed, the same cell was stimulated multiple times by the same insulin secretagogue or stimulated by different secretagogues. As shown in Figure 3-1B, secretion from a single cell was localized to the same region when it was successively stimulated by 20 mM glucose with 5 min interval allowed between two stimulations. Constant release sites on single cells for repetitive glucose stimulation were observed in all cases (n = 5) that were attempted. When cells were stimulated by glucose and carbachol sequentially, the same release sites were also observed for a given cell in all cases (n = 4, data not shown).

Spatially Localized Ca^{2+} Entry in Single β-Cells

The concept of Ca^{2+}-secretion coupling in excitable cells, including pancreatic β-cells, has been well accepted (Penner and Neher, 1988). Therefore, the spatial relationship between localized secretion and increases in $[Ca^{2+}]_i$ is of interest. It has been difficult to observe localized changes in $[Ca^{2+}]_i$ in single cells because Ca^{2+} ions diffuse across the entire cell in less than one second. High temporal resolution is required for spatially resolved calcium imaging.

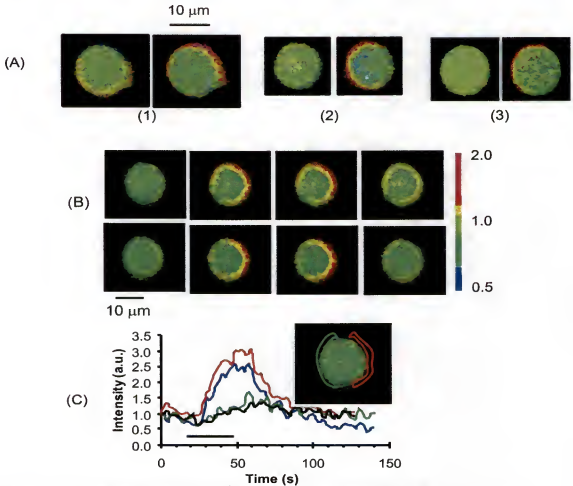

Figure 3-1. Spatially localized Zn^{2+} secretion from single β-cells. (A) Secretion induced by different secretagogues. Images are shown in intensity ratios against a reference image acquired before stimulation. The regions with colors in high ratios (yellow to red) around the cell circumference indicate fluorescence increases over basal, which correspond to the detection of Zn^{2+} secretion. For each stimulant, a basal image and an image during secretion were selected to show the exocytotic release sites. All images were taken at a rate of 2.13 s per image. The stimuli used were (1) 40 mM K^{+}, (2) 20 mM glucose, (3) 200 μM carbachol. (B) Secretion evoked by multiple glucose stimulations. Images in the upper and bottom rows correspond to the 1st and 2nd stimulation, respectively. In each row, an image before stimulation, two images during secretion and an image after secretion were selected. (C) Average fluorescence intensities within the ROIs as a function of time. Image series in B were analyzed using the ROIs shown in the inset image. The top two traces (red and blue) are from the right ROI and the bottom traces (green and black) are from the left ROI. The red and green traces are data from the 1st stimulation and the blue and black traces are data from 2nd stimulation. The bar underneath the traces indicates the application of 20 mM glucose.

In initial experiments, the existence of localized increases in $[Ca^{2+}]_i$ in single β-cells was investigated using indo-1 ratio-imaging with 133 ms temporal resolution. In these experiments, cells were stimulated to depolarize by either 40 mM K^+ or 20 mM glucose. Both stimuli lead to the opening of voltage-gated Ca^{2+} channels on the plasma membrane and Ca^{2+} entry from the extracellular space. Figure 3-2 shows a typical example of Ca^{2+} entry evoked by 40 mM K^+. As in Figure 3-2A, Ca^{2+} entry was observed immediately following stimulation as indicated by increases in $[Ca^{2+}]_i$ in the vicinity of plasma membrane. In less than 1 s after stimulation was applied, increases in $[Ca^{2+}]_i$ can be observed all across the cell, indicative of rapid diffusion of entered Ca^{2+} across the cell. Interestingly, increases in $[Ca^{2+}]_i$ show clear spatial heterogeneity with more pronounced increase at the top side of membrane region (Figure 3-2A, images at 0.1 and 0.3 s), which suggests localized Ca^{2+} entry at this region. The spatial heterogeneity is more apparent in the $[Ca^{2+}]_i$ profiles shown in Figure 3-2B. These profiles show that $[Ca^{2+}]_i$ directly beneath the membrane reaches over 3 μM shortly after stimulation on one portion of the cell perimeter, while on the opposite side of the cell $[Ca^{2+}]_i$ levels only reach ~0.4 μM. The data also show steep $[Ca^{2+}]_i$ gradients moving from the edge of the cell to the interior. The steep $[Ca^{2+}]_i$ gradients disappear following the removal of stimulus. While concentrations over 1 μM were routinely observed near the cell membrane, the average $[Ca^{2+}]_i$ over the entire cell was only ~0.5 μM at the peak response. The actual $[Ca^{2+}]_i$ at the sites of Ca^{2+} entry may be even higher than those shown in Figure 3-2 since the buffering effect of Ca^{2+} indicator may suppress $[Ca^{2+}]_i$ transients (Sala and Hernandez-Cruz, 1990). The high $[Ca^{2+}]_i$ right beneath the plasma membrane may be critical for triggering exocytosis.

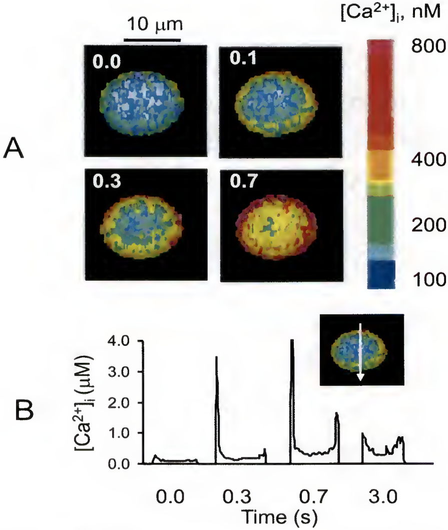

Figure 3-2. Localized Ca^{2+} entry evoked by 40 mM K^+. (A) Ca^{2+} images. Images are shown in $[Ca^{2+}]_i$ as indicated by the scale-bar, which was converted from dual-channel emission intensity ratios. Image acquisition rate was 133 ms per image. The cell was stimulated by 40 mM K^+ at time 0 for one second and the time (in seconds) at which each image was acquired is indicated in each image. (B) $[Ca^{2+}]_i$ profiles at four different points of time. Concentration profiles correspond to the vertical line shown in the inset image.

Spatially localized Ca^{2+} entry such as that shown in Figure 3-2 was observed for 65% cells that responded to 40 mM K^+ (n = 20). Similar localized Ca^{2+} transients were also observed for cells stimulated by 20 mM glucose (n = 9). These results are in agreement with previous studies in β-cells either by voltage-clamp depolarization or by glucose stimulation (Gylfe et al., 1991; Bokvist et al., 1995; Martin et al., 1997). Just as secretion patterns were the same for multiple stimulations, spatial patterns of Ca^{2+} transients evoked by multiple K^+ or glucose stimulations were also the same (data not shown). All of the increases in $[Ca^{2+}]_i$ evoked by K^+ or glucose were inhibited by pretreatment of cells with 20 μM nifedipine, a blocker of $_L$-type voltage-gated Ca^{2+} channels.

When cells were stimulated with 200 μM carbachol, increases in $[Ca^{2+}]_i$ appeared to occur over the entire cell and no obvious spatial localization of $[Ca^{2+}]_i$ changes was observed (data not shown). The $[Ca^{2+}]_i$ responses caused by carbachol were not inhibited by nifedipine treatment. The results confirm that carbachol has a different mechanism for Ca^{2+} mobilization than that of the depolarizing agents such as K^+ and glucose (Theler et al., 1992).

Co-localization of Exocytotic Release Sites and Ca^{2+} Entry

In order to reveal the spatial relationship of localized Ca^{2+} entry and exocytotic release sites, Ca^{2+} transients and Zn^{2+} secretion were measured from the same cell. Attempts to measure Zn^{2+} secretion and $[Ca^{2+}]_i$ simultaneously were unsuccessful because of the emission spectral overlap of indo-1 and Zinquin and the mismatch of excitation powers needed for Ca^{2+} and Zn^{2+} measurements. The latter problem resulted from the requirement that the excitation power for Ca^{2+} measurements must be low (~10 μW) to avoid the photobleaching of indo-1, while for Zn^{2+} measurements a relatively high excitation power (~100 μW) is required to generate enough signal in order to detect relatively small amounts of Zn^{2+} released from the cell. Due to these technical difficulties, a sequential measurement scheme was utilized for detection of secretion and $[Ca^{2+}]_i$ at single cells (see Experimental section). The use of sequential measurements to correlate Zn^{2+} secretion and Ca^{2+} transients spatially is justified because the spatial patterns of secretion and Ca^{2+} transients were maintained the same for multiple stimulations at a given cell.

Figure 3-3 and 3-4 shows the results of typical sequential measurements of Ca^{2+} transients and Zn^{2+} secretion from a β-cell stimulated by 20 mM glucose. The initial Ca^{2+} entry shown in the images of Figure 3-3 is mainly localized at the left side of the plasma membrane. The difference between regions is not as extreme in this case because of lower temporal resolution used. Interestingly, $[Ca^{2+}]_i$ is elevated more in the left side even during the basal state (Figure 3-4A), suggesting some basal Ca^{2+} channel activities.

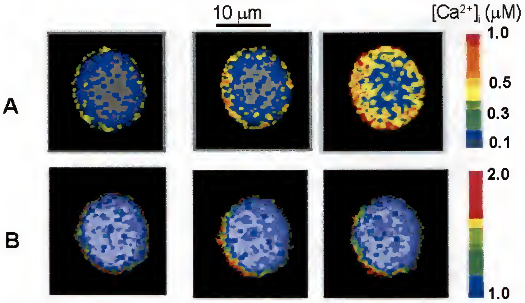

Figure 3-3. Sequential measurements of Ca^{2+} transients and Zn^{2+} secretion from the same cell. (A) Images of $[Ca^{2+}]_i$. (B) Images of Zn^{2+} secretion. Images of Zn^{2+} secretion are shown in intensity ratios as described in Figure 3-1. $[Ca^{2+}]_i$ images were acquired in 2 s interval with an acquisition time of 266 ms for each image. Zn^{2+} images were acquired continuously with 2.13 s per image. The 1st image in each row was taken before stimulation. The 2nd and 3rd Ca^{2+} images show the initial Ca^{2+} entry after stimulation and an overall Ca^{2+} increase over the cell, respectively. The 2nd and 3rd Zn^{2+} images were selected after stimulation, which show the occurrence of Zn^{2+} secretion indicated by fluorescence increases around the cell circumference.

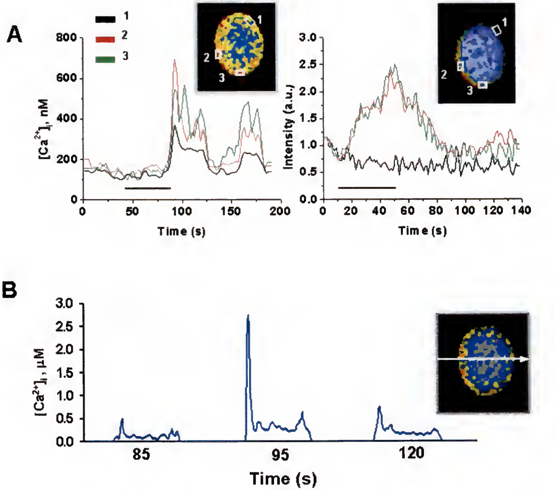

Figure 3-4. Correlation of Ca^{2+} transients and Zn^{2+} secretion from the same cell. (A) Time courses of Ca^{2+} transients (left) and Zn^{2+} secretion (right). The images analyzed are the same as in Figure 3-3. ROIs used for data analysis are shown in the inset images. Traces of different ROIs are in different colors as indicated by the color bars in the left graph. 20 mM glucose was applied for 40 s for both stimulations as indicated by the bars underneath the traces. (B) $[Ca^{2+}]_i$ profiles at three different points of time. The time scale used is same as that in (A). Concentration profiles correspond to the white line shown in the inset image.

Similarly, the Zn^{2+} secretion was only observed at the left side of the membrane covering ~50% of the circumference. The sites of Zn^{2+} secretion correlate well with the sites with the greatest increases in $[Ca^{2+}]_i$ as shown in Figure 3-4A. While increases in $[Ca^{2+}]_i$ could be observed at nearly all points around the cell, secretion was only observed at the points where $[Ca^{2+}]_i$ were at their highest and where the increases in $[Ca^{2+}]_i$ occurred earliest. As shown in Figure 3-4A, although the average $[Ca^{2+}]_i$ at the stimulatory level is only around 300 nM, the $[Ca^{2+}]_i$ at the calcium entry sites can reach μM range as clearly shown in the $[Ca^{2+}]_i$ profiles in Figure 3-4B. The high $[Ca^{2+}]_i$ at the calcium entry sites probably is necessary for triggering exocytosis.

Similar results were observed for eight separate experiments with stimuli that cause Ca^{2+} entry (n = 3 for glucose stimulation, n = 5 for K^+ stimulation). Due to the limitations of the temporal resolution and sensitivity of calcium imaging, occasionally we were not able to identify the Ca^{2+} entry sites as clearly as shown in Figure 3-3. Nevertheless, in all experiments that cells secreted in response to stimulation, the exocytotic release sites correlate well to a region close to plasma membrane with the highest $[Ca^{2+}]_i$ through the entire time course similar to that shown in Figure 3-4A.

Spatially Localized Secretion Independent of Ca^{2+} Channel Activity

Our data show co-localization of exocytotic release sites and Ca^{2+} entry points on the cell membrane. Localized Ca^{2+} entry provides locally high $[Ca^{2+}]_i$, which may be sufficient to confine secretion to the same area of membrane. To determine if localized elevation of $[Ca^{2+}]_i$ was solely responsible for confining secretion to a given membrane region, we tested the effects of 4-Br-A23187, a non-fluorescent Ca^{2+} ionophore, on the spatial distribution of $[Ca^{2+}]_i$ and secretion. Since Ca^{2+} ionophore allows fast transport of Ca^{2+} ions through the plasma membrane, rapid homogeneous Ca^{2+} influx is expected. As shown in Figure 3-5A and 3-5B, treatment of cells with the Ca^{2+} ionophore resulted not in a localized increase in $[Ca^{2+}]_i$, but in a large increase in $[Ca^{2+}]_i$ all around the cell perimeter as expected. Despite the homogeneity of $[Ca^{2+}]_i$ increase all around the cell and the high $[Ca^{2+}]_i$ (> 3 μM) in the vicinity of plasma membrane, Zn^{2+} secretion induced by 4-Br-A23187 was still localized just as those induced by K^+ or glucose stimulation (Figure 3-6A). The active membrane area for secretion evoked by 4-Br-A23187 was 49 ± 13% (n = 7), not significantly different from that observed with other secretagogues. Furthermore, as illustrated in Figure 3-6A and 3-6B, a cell showed the same active area of secretion when it was stimulated by glucose and ionophore sequentially (n = 3).

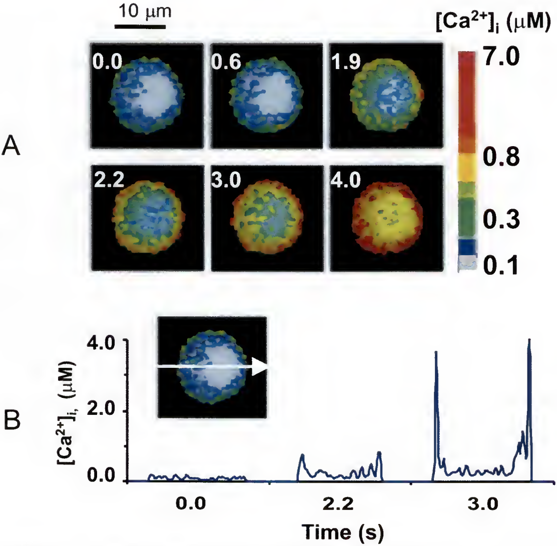

Figure 3-5. Calcium ionophore (4-Br-A23187) induced Ca^{2+} entry. (A) Ca^{2+} images. The cell was stimulated by 20 µM 4-Br-A23187 at time 0 and the time (in seconds) at which each image was acquired is indicated. Images were acquired at a rate of 266 ms per image. (B) $[Ca^{2+}]_i$ profiles at three different points of time. Concentration profiles correspond to the horizontal line shown in the inset image.

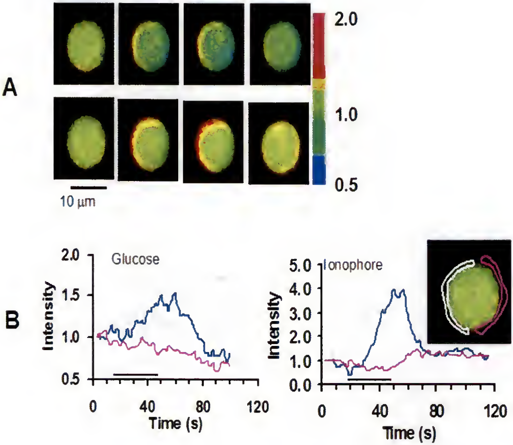

Figure 3-6. Ionophore and glucose induced localized secretion. (A) Images of localized secretion. Images are shown in intensity ratios as in Figure 3-1. The cell was first stimulated by 20 mM glucose (Images in top row). After 5 min, the same cell was stimulated again by 20 µM 4-Br-A23187 (Images in bottom row). In each row, an image before stimulation, two images during secretion and an image after secretion were selected. (B) Average intensities within the ROIs as a function of time. Image series in C were analyzed within the ROIs shown in the inset image. In both plots, the blue traces correspond to the left ROI and the red traces correspond to the right ROI. The bars underneath the traces indicate the application of stimulation.

All experiments with the ionophore were repeated in the presence of 20 µM nifedipine to block any effects of influx through voltage-gated Ca^{2+} channels and comparable results were achieved. Therefore, secretion evoked by ionophore stimulation was independent of Ca^{2+} influx through Ca^{2+} channels, yet secretion was localized to the same membrane region as for other secretagogues.

Discussion

Active Zones of Secretion

We have observed that Zn^{2+} secretion from β-cells, and by inference insulin secretion, is confined to an active area of membrane that comprises ~50% of the cell circumference as visualized by confocal fluorescence microscopy. These data confirm the existence of "hot" zones of secretion reported earlier by amperometry for β-cells and other neuroendocrine cells (Paras et al., 2000; Bokvist et al., 2000; Robinson et al., 1995) and provide the first measurement of the size and organization of these zones. The actual size of the release zones may be smaller than that observed by this approach because Zn^{2+} diffusion from the release spot may enlarge the region where increase in fluorescence is observed. Our data also extend the initial observations made on β-cells by demonstrating that active secretion areas are constant with K^+, glucose, carbachol, and Ca^{2+} ionophore (4-Br-A23187) stimulation. The observation that exocytotic release sites for a single cell are the same even when different stimuli were applied or when the same stimulant was applied to the cell multiple times indicates that the release sites are fixed and regulated by an effect that is downstream of the initial stimulus.

Localization of Ca^{2+} Entry

In addition to localized secretion, we also observed that increases in $[Ca^{2+}]_i$ following glucose and K^+ were greatest at certain regions of the plasma membrane. This result is in agreement with previous reports on imaging of $[Ca^{2+}]_i$ at high temporal resolution in β-cells and adrenal chromaffin cells (Gylfe et al., 1991; Bokvist et al., 1995; Martin et al., 1997; Robinson et al., 1995; Monck et al., 1994). Since Ca^{2+} influx is primarily through $_L$-type Ca^{2+} channels in mouse β-cells (Gilon et al., 1997), these results indicate that the activity of ${}_{L}$-type Ca^{2+} channels is localized as well. The clustering of Ca^{2+}-channels in certain membrane domains on β-cells has also been inferred from patch-clamp recordings, which found that some membrane patches contained 20-30 channels while others only contained 1 or 2 channels (Rorsman et al., 1988).

Localization of Exocytotic Machinery

Our results indicate that the increases in $[Ca^{2+}]_i$ are co-localized with the secretory sites. The co-localization of Ca^{2+} entry sites and exocytotic release sites supports the model that high $[Ca^{2+}]_i$ activates exocytotic machinery at the Ca^{2+} entry sites and triggers exocytosis in those locations. Since Ca^{2+} is a primary triggering signal for exocytosis, the localization of Ca^{2+} entry sites may be sufficient to localize secretion to membrane near the Ca^{2+} channel activity. However, it has been observed that increases of $[Ca^{2+}]_i$ all around the circumference induced by a Ca^{2+} ionophore evoked secretion that was localized to the same portion of membrane as other secretagogues (Figure 3-5 and 3-6). The $[Ca^{2+}]_i$ evoked by the ionophore was sufficiently high to trigger exocytosis in all portions of the membrane as evidenced by the $> 3\ \mu M$ concentration, so a lack of Ca^{2+} was not the limiting factor. This result suggests that other elements of the exocytotic machinery such as vesicles and/or exocytotic proteins are also localized within the cell independent of Ca^{2+} channel activity.

In β-cells, the cytoplasm is filled with insulin secretory granules (Bonner-Weir, 1988) and readily releasable vesicles are only small fraction of total amount of vesicles (Eliasson et al., 1997). Several lines of evidence have suggested that β-cell secretory vesicles may be localized and closely associated with Ca^{2+} channels. A polarity in distribution of insulin granules was observed for partially degranulated β-cells by electron microscopy (Bonner-Weir, 1988). An uneven distribution of secretory granules measured by quinacrine fluorescence was also reported and the region with high density of secretory granules co-localized with Ca^{2+} entry (Bokvist et al., 1995). Finally, synaptotagmin, a vesicular protein involved in exocytosis (Brose et al., 1992; Brown et al., 2000), has recently been demonstrated to be physically associated with Ca^{2+} channels by both *in vitro* binding studies and in *Xenopus* oocytes (Wiser et al., 1996; Wiser et al., 1999). This close association also suggests that readily releasable vesicles are near the Ca^{2+} channels.

In addition to localized vesicles, it is also possible that the plasma membrane exocytotic proteins associate exclusively with the $_L$-type Ca^{2+} channels to create functional zones for exocytosis. Recent studies demonstrated that the plasma membrane proteins syntaxin and SNAP-25 are physically associated with the L_c-type Ca^{2+} channels (Wiser et al., 1996; Wiser et al., 1999). Another study reported that syntaxin 1 was co-localized in the plasma membrane of β-cells with the L_d subtype Ca^{2+} channels (Yang et al., 1999). This physical association could serve as the basis for localized secretion even in the presence of a global increase in $[Ca^{2+}]_i$ evoked by Ca^{2+} ionophore. That is, if the proteins necessary for exocytosis are localized with the $_L$-type Ca^{2+} channels then Ca^{2+} can activate secretion only in these regions.

Figure 3-7 presents a simplified model of localized secretion in β-cell based on the data presented here and other previously reported known protein interactions. Ca^{2+} influx through Ca^{2+} channel provides localized high $[Ca^{2+}]_i$, which trigger interactions of multiple exocytotic proteins including vesicular membrane protein such as synaptotagmin, and plasma membrane proteins such as syntaxin, SNAP-25 and Ca^{2+}

channels (Figure 3-7A; Lang, 1999). Ca^{2+} channels, exocytotic membrane proteins, and/or secretory vesicles are spatially co-localized to a specific region on the plasma membrane of β-cell, which acts as an active zone of secretion (Figure 3-7B).

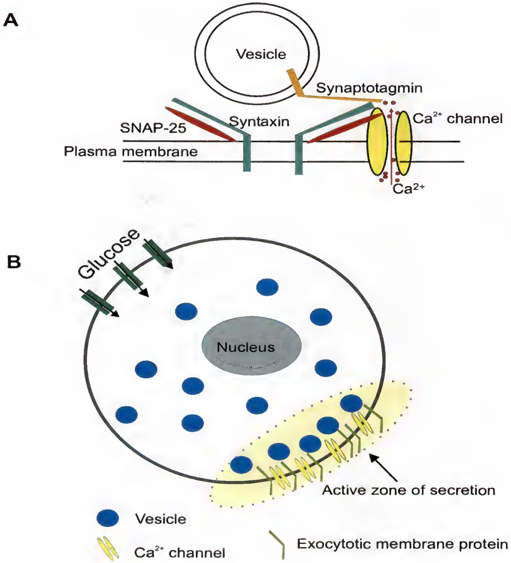

Figure 3-7. A simplified model of localized secretion in β-cell. (A) Interactions of multiple proteins during exocytosis. (B) Active zone of secretion. Ca^{2+} channels, exocytotic membrane proteins, and/or secretory vesicles are spatially co-localized in the active zone of secretion

The data presented here provide further evidence for an organization of β-cells with respect to the activities of the plasma membrane by showing an active secretion area that co-localizes with high Ca^{2+} levels and apparently proteins or organelles necessary for exocytosis. Other work has demonstrated that the GLUT-2 glucose transporter and insulin binding sites are also localized to specific plasma membrane domains, the actin-rich β-cell microvilli (Orci et al., 1989; Bendayan, 1992). Thus, the β-cell may have a "sensing" region and a "secreting" region on the plasma membrane. Further studies are required to determine how this organization is maintained, even by cells in culture, and the advantages of such a spatial organization to the organism.

CHAPTER 4
DETECTION AND IMAGING OF Zn^{2+} RELEASE AT THE LEVEL OF SINGLE EXOCYTOTIC EVENTS

Introduction

Zn^{2+} is a critical element involved in many cellular processes. Whereas most Zn^{2+} in biological systems is tightly bound to proteins, a pool of free ionic Zn^{2+} is also found in cells such as hippocampal neurons (Frederickson et al., 2000) and pancreatic islet cells (Zalewski et al., 1994). In the central nervous system, Zn^{2+} is highly concentrated in the synaptic vesicles of a subset of glutamatergic neurons and is released along with glutamate when vesicles release their contents into the extracellular space by exocytosis (Frederickson et al., 2000). In pancreatic islets, most Zn^{2+} is stored in insulin secretory vesicles and is either labile or in the form of crystals containing hexamers of insulin with two or more Zn^{2+} per hexamer (Blundell et al., 1972). During exocytosis, Zn^{2+} is co-released with insulin from secretory vesicles of β-cell (Emdin et al., 1980; Formby et al., 1984; Gold and Grodsky, 1984; Grodsky and Schmid-Formby, 1985; Foster et al., 1993).

Although much has been learned about the functions of bound Zn^{2+} in metalloenzymes (Lippard and Berg, 1994), the role of free Zn^{2+} and of vesicular Zn^{2+} release in neuronal and endocrine systems remains enigmatic. Zn^{2+} stored and released from synaptic vesicles appears to act as a neurotransmitter or neuromodulator at glutamate synapses (Huang, 1997). Free Zn^{2+} has been shown to influence NMDA (Peters et al., 1987), GABA (Smart et al., 1991) receptors, and a variety of other ion channels on the cell surface (Harrison and Gibbons, 1994). It may also play a role in the development of Alzheimer's disease and excitotoxicity (Cuajungco et al., 1997; Frederickson et al., 2000). Zn^{2+} released from pancreatic β-cells may act as a paracrine agent in promoting islet cell death, especially in hyperinsulinemic states (Kim et al., 2000). Secreted Zn^{2+} may also activate ATP-sensitive K^+ channels on β-cells and therefore serve an auto-regulatory role in secretion (Bloc et al., 2000). Given the potential roles for released Zn^{2+} in modulating neuronal and endocrine functions, it would be of interest to better understand the regulation and dynamics of Zn^{2+} release from these cells.

Release of Zn^{2+} from the secretory vesicles of pancreatic β-cells and the synaptic vesicles of glutamatergic neurons occurs via exocytosis (Howell et al., 1984; Perez-Clausell and Danscher, 1986). It has been demonstrated that exocytotic release of vesicular contents to the extracellular space occurs on the time scale of milliseconds (Travis and Wightman, 1998). The study of Zn^{2+} release from cells, therefore, requires techniques for detection of Zn^{2+} release with high sensitivity and high temporal resolution. Such techniques may be also of value in the fundamental studies of exocytosis, which is vital for understanding both neuronal and endocrine signaling.

Recent advances in Zn^{2+} sensitive fluorescent probes have greatly aided the studies of Zn^{2+} release from cells. Several fluorescent probes and biosensor indicators have been used to measure free Zn^{2+} in pancreatic islets and hippocampal slices, both intracellularly and upon release from these tissues (Zalewski et al., 1994; Budde et al., 1997; Sensi et al., 1997; Thompson et al., 2000; Varea et al., 2001). Recently, a confocal fluorescence imaging approach has been developed for spatially resolved monitoring of Zn^{2+} release from single pancreatic β-cells using extracellular fluorogenic reactions

(Chapter 2; Qian et al., 2000). Since Zn^{2+} and insulin are co-released from pancreatic β-cells by exocytosis (Emdin et al., 1980; Formby et al., 1984; Gold and Grodsky, 1984; Grodsky and Schmid-Formby, 1985; Foster et al., 1993), this approach also serves a novel technique for monitoring insulin secretion from β-cells. In this approach, cells were incubated in buffer containing a fluorogenic Zn^{2+}-specific fluorophore Zinquin (Zalewski et al., 1994), while fluorescence signals were monitored by confocal laser-scanning microscopy. When secretion was evoked by stimulation, the released Zn^{2+} reacts with Zinquin in the extracellular space to form a fluorescent complex, resulting in fluorescence increases at the sites of release on the cell surface. With this approach, the dynamics of Zn^{2+} release from single β-cells can be recorded in a spatially and temporally resolved manner; however, the sensitivity of detection and the temporal resolution were limited due to the relatively low signal levels of the probe Zinquin. In the present study, we report the use of a novel fluorescent Zn^{2+} probe FluoZin-3 and the resulting improvements in the sensitivity and the temporal resolution for detection of Zn^{2+} release from pancreatic β-cells. With the improved sensitivity and temporal resolution, Zn^{2+} release from individual secretory vesicles has been observed and the temporal and spatial characteristics of single exocytotic release events have been examined. This is the first report of temporally resolved measurements of exocytotic release product from individual secretory vesicles by a fluorescence imaging approach.

Experimental

Chemicals

FluoZin-3 was prepared at Molecular Probes as previously described (Gee et al., 2002). Tetrakis-(2-pyridylmethyl) ethylenediamine (TPEN) was from Molecular Probes.

Type XI collagenase, HEPES, and EGTA were from Sigma. Puratronic grade $CaCl_2$ and $MgCl_2$ were from Alfa AESAR. Unless otherwise stated, all chemicals for islets and cell culture were obtained from Life Technologies. All other chemicals were from Fisher unless noted and were of the highest purity possible.

Isolation and in Vitro Culture of Mouse Pancreatic β-cells

Pancreatic islets were isolated from CD-1 mice as described in Chapter 2. Briefly, islets were isolated by ductal injection with type XI collagenase and were dispersed into isolated cells by shaking in 0.025% trypsin/EDTA for 6 min at 37° C. Dispersed cells were plated onto 25 mm diameter coverslips in tissue culture dishes (Corning) and incubated in RPMI 1640 medium containing 10% fetal bovine serum, 100 U/mL penicillin and 100 μg/mL streptomycin at 37° C, 5% CO_2, pH 7.4. Cells were used for experiments 1 to 2 days after isolation.

Spectroscopic Measurements

Fluorescence emission spectra of FluoZin-3 were recorded on a SPEX Fluorolog-3 Fluorescence Spectrometer (Jobin Yvon Inc., Edison, NJ) with a 150 W Xe lamp for excitation. Measurements were performed at 22° C, pH 7.4 in buffered Zn^{2+} solutions containing 20 mM HEPES, 135 mM NaCl, 0.5 μM FluoZin-3, 1.1 mM total EGTA, and 0 – 1.1 mM $ZnCl_2$. All solutions were filtered with 0.2 μm cellulose filter before measurements. Free Zn^{2+} concentration in the buffer was calculated from the equation $K_d = [Zn^{2+}][EGTA]/[Zn^{2+}\text{-}EGTA]$ using the dissociation constant $K_d = 1.1$ nM of EGTA for Zn^{2+} (Sensi et al., 1997). All emission spectra of FluoZin-3 were corrected for blank using a buffer solution without FluoZin-3.

Confocal Imaging

All imaging experiments were performed on a Nikon RCM 8000 confocal laser-scanning microscope with a Nikon 40x, 1.15 NA, UV-corrected water-immersion objective. This system offers an imaging acquisition rate of 30 Hz, i.e. 30 full frames per second. Typically, a number of frames will be averaged to reduce noise in the images. Thus, averaging 32 frames collected at 30 Hz will give an image acquisition rate of 1.07 s per image. Imaging acquisition rate greater than 30 Hz can also be achieved using the band-scanning mode. For example, for a 2-band scanning mode, the original full frame is divided into two equal bands and only one band of choice will be scanned during imaging. Therefore, the image acquisition rate for this scan mode is 60 Hz, which is two times faster than that of full frame scanning. In band-scanning, frames cannot be averaged due to the instrumental limitation. More details of this confocal system can be found in Appendix A.

Zn^{2+} images with FluoZin-3 were acquired with 488 nm excitation and 525 ± 10 nm band-pass emission filters. Zn^{2+} images with Zinquin and UV autofluorescence images were acquired with 351 nm excitation and 480 ± 10 nm emission filters. All images were stored on an optical disc cartridge (TQ-FH332, Panasonic) by an optical disc recorder (TQ-3038F, Panasonic) for later analysis.

Buffer with minimum background Zn^{2+} level was prepared as previously described for imaging experiments (Thompson et al., 2000). Briefly, Kreb's Ringer buffer (KRB, 118 mM NaCl, 5.4 mM KCl, 2.4 mM $CaCl_2$, 1.2 mM $MgSO_4$, 1.2 mM KH_2PO_4, 20 mM HEPES, 3.0 mM D-glucose) was prepared with all ingredients except calcium and magnesium salts. The buffer was then treated with Chelex-100 (Bio-Rad), an ion exchange resin for removing divalent cations, by adding 5 g Chelex-100 per 100 mL buffer and stirred for 2 h. The pH of the buffer was adjusted to 7.4 after Chelex-100 treatment and Puratronic grade $CaCl_2$ and $MgCl_2$ (Alfa AESAR) were added to the final concentrations. During all experiments and solution preparation, glass containers were avoided to minimize metal contamination.

Cells to be imaged were bathed in buffer containing 2 μM FluoZin-3 and maintained at 37° C on the stage of the microscope by a microincubator (Medical Systems, Inc.). Before imaging, the buffer was titrated with a high affinity non-fluorescent Zn^{2+} chelator TPEN to deplete the trace amount of Zn^{2+} present in the buffer in order to reduce background fluorescence. The typical final concentration of TPEN in the buffer was ~200 nM. Stimulation (30 mM K^+ or 20 mM glucose) solutions containing the same concentration of FluoZin-3 as the bathing buffer were applied to the cells by pressure ejection at 3-6 psi from micropipettes positioned ~60 μm from the cells.

Data Analysis

Images were played back from the optical disk cartridge and captured and analyzed using Simca image analysis software (C-IMAGING Systems). For plots of fluorescence intensity as a function of time, regions of interest (ROIs) around the cells were highlighted and average intensities within the ROIs were calculated for a series of images. Intensity profiles and smoothed images were generated by MetaMorph image analysis software (Universal Imaging Corporation). All means are reported as ± 1 standard deviation (S.D.).

Results

Properties of FluoZin-3

FluoZin-3 (Figure 4-1A) is a novel Zn^{2+} specific fluorescent probe that is structurally related to the fluorescent calcium probes fluo-3 and fluo-4 (Gee et al., 2000). These probes are excited by visible light with excitation maximum at 490 nm. The emission spectra of FluoZin-3 and its binding affinity for Zn^{2+} were characterized using buffered Zn^{2+} solutions with increasing free Zn^{2+} concentrations ($[Zn^{2+}]$). The free $[Zn^{2+}]$ is controlled by Zn^{2+}/EGTA buffer as described in the Experimental section. In the absence of Zn^{2+}, FluoZin-3 exhibits nearly no fluorescence, while the fluorescence emission increases dramatically as free $[Zn^{2+}]$ increases (Figure 4-1B). A maximum fluorescence enhancement of ~400-fold was observed at 10 μM free Zn^{2+}. The Zn^{2+} binding affinity of FluoZin-3 was determined by plotting the normalized fluorescence response against free $[Zn^{2+}]$ (Figure 4-1C). The measurements were performed in triplicate using different EGTA/Zn^{2+} buffers and an apparent K_d of 15 ± 2 nM was obtained. The fluorescence response fit to a Hill coefficient of 1, consistent with a 1:1 binding of FluoZin-3:Zn^{2+}. The selectivity of FluoZin-3 for Zn^{2+} over Ca^{2+} and Mg^{2+} was examined by addition of 2.4 mM Ca^{2+} and 1.2 mM Mg^{2+} to the HEPES buffer containing 2 μM TPEN. No obvious fluorescence increase was observed with the addition of these divalent cations until more extracellular Zn^{2+} was added, suggesting that FluoZin-3 fluorescence is Zn^{2+} specific.

Figure 4-2A shows the pH sensitivity of FluoZin-3. In the presence of saturating Zn^{2+} (10 μM), the fluorescence response is stable between pH 6 to 9. The fluorescence decreases as pH drops below 6.0 and fluorescence disappears at pH < 4.0. The pH

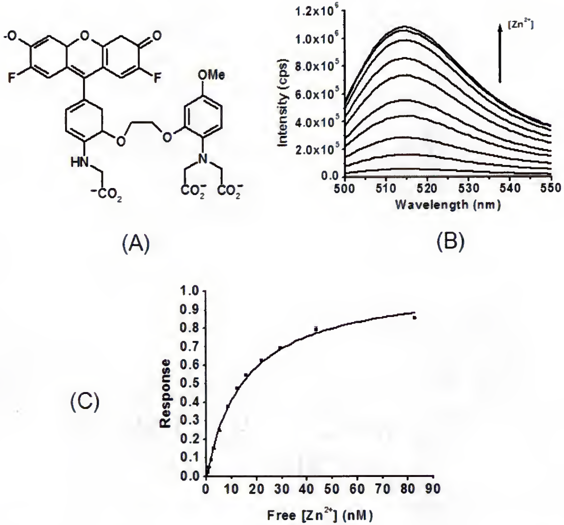

Figure 4-1. The chemical structure of FluoZin-3 and its fluorescence in response to Zn^{2+} binding. (A) Structure of FluoZin-3. (B) Fluorescence emission spectra (excited at 488 nm) of FluoZin-3 (0.5 μM) in buffered Zn^{2+} solutions with free (unbound) Zn^{2+}concentrations of 0, 1, 3, 5, 9, 12, 20, 30, 45, and 80 nM, respectively. For the final spectrum (containing 1.1 mM EGTA and 1.1 mM Zn^{2+}), additional $ZnCl_2$ was added to provide 10 μM free Zn^{2+}. The 1st spectrum almost overlaps with the X-axis indicating the very low fluorescence in the absence of Zn^{2+}. Fluorescence intensity is in arbitrary unit. (C) Normalized fluorescence response as a function of free [Zn^{2+}]. The fluorescence emission intensities at 515 nm (maximum emission) were normalized to the full scale response obtained at 10 μM free Zn^{2+}. An apparent K_d of 15 nM was obtained by analyzing the data with nonlinear least-square fitting.

dependence of the fluorescence response gives an apparent pK_a of 4.8 for FluoZin-3.

This pH dependence correlates exactly with the fluorescence pH dependence of other 2,7-

difluoroxanthen-3-ol-6-ones (Sun et al., 1997b), which lose their fluorescence as the phenolic hydroxyl group ($pK_a = 4.8$) becomes protonated. This behavior indicates that the pH sensitivity of FluoZin-3 is due exclusively to the protonation of the phenolic hydroxyl group on the fluorophore part of the molecule at low pH, and not of the chelator portion.

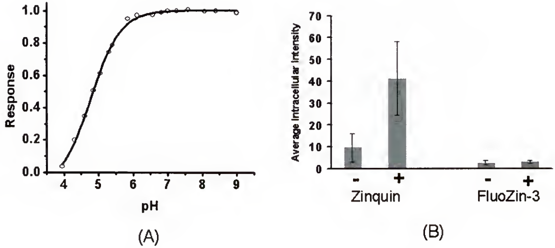

Figure 4-2. pH sensitivity and membrane permeability of FluoZin-3. (A) Dependence of the fluorescence response of FluoZin-3 on the buffer pH. KRB containing 2 μM FluoZin-3 and 10 μM Zn^{2+} were imaged by the confocal system with 488 nm excitation. The average fluorescence intensities were normalized to the full scale response obtained at pH 9. (B) Comparison of the membrane permeability of Zinquin and FluoZin-3. The relative fluorescence intensities were averages of 15 cells. The error bars shown are standard deviations. Cells were incubated in KRB either containing no dyes or containing 10 μM Zinquin or 2 μM FluoZin-3. The symbol '-' indicates the absence of the dye and '+' indicates the presence of the dye. Images used for the left two columns were acquired with 351 nm excitation and 480 ± 10 nm emission filters, while images used for the right two columns were acquired with 488 nm excitation and 525 ± 15 nm emission filter.

The membrane permeability of FluoZin-3 was also investigated since a membrane impermeable probe is of advantage for imaging of Zn^{2+} release from cells by extracellular fluorogenic reactions. As shown in Figure 4-2B, the membrane permeability of the zinc fluorophores Zinquin and FluoZin-3 was compared. Cells incubated with Zinquin shows much higher fluorescence intensity, indicating that Zinquin is permeant to the cell membrane. No obvious fluorescence increase was observed for cells incubated with FluoZin-3, suggesting a minimal membrane permeability of FluoZin-3. The low membrane permeability of FluoZin-3 is expected because FluoZin-3 has four negative charges at biological pH range while Zinquin only has one negative charge.

Imaging of Zn^{2+} Release with FluoZin-3

The use of FluoZin-3 for imaging Zn^{2+} release from isolated β-cells was investigated using K^+ and glucose stimulation. In these experiments, cells were incubated in KRB containing 2 μM FluoZin-3 while fluorescence was monitored by confocal microscopy. As shown in Figure 4-3, when 40 mM K^+ or 20 mM glucose was applied to the cells, large fluorescence increases were observed outside the cells, corresponding to detection of Zn^{2+} release from the cells. Figure 4-3A shows the detection of Zn^{2+} release from a single β-cell following K^+ stimulation, while Figure 4-3B shows Zn^{2+} release from a cluster of four cells following glucose stimulation. Zn^{2+} is co-released with insulin from β-cells by exocytosis to the extracellular space where it reacts with FluoZin-3 to form a highly fluorescent complex FluoZin-3:Zn^{2+}, leading to the observation of fluorescence increases outside the cells.

Several observations support the conclusion that the signals represent the detection of Zn^{2+} co-released with insulin from β-cells by exocytosis. In the presence of a high affinity Zn^{2+} chelator TPEN (50 μM), no fluorescence increases were observed from cells following glucose or K^+ stimulation, confirming that the observed fluorescence enhancements are dependent on the presence of free Zn^{2+} and the formation of the

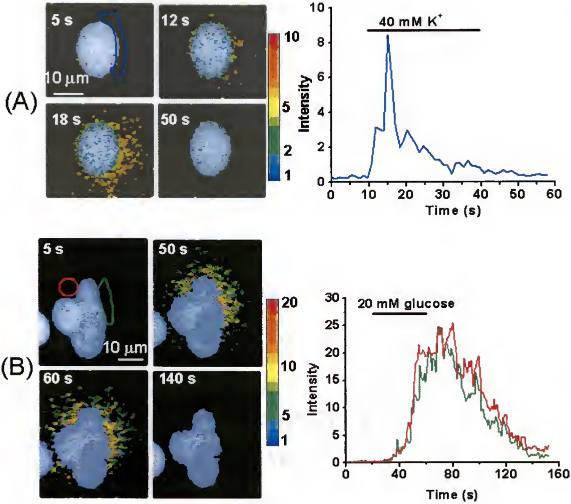

Figure 4-3. Imaging of Zn^{2+} release from isolated pancreatic β-cells. Images are shown in fluorescence intensity ratios against a UV autofluorescence image in order to highlight the extracellular fluorescence enhancements. The time at which each image was acquired is indicated in seconds. All images were acquired at a rate of 1.07 s per image (32 frames averaged per image). The temporal responses were analyzed using regions of interest (ROIs) outside the cells as indicated in the images. The bars on top of the traces indicate the periods of stimulation. (A) Zn^{2+} release from a single cell induced by 40 mM K$^+$ stimulation. (B) Zn^{2+} release from a cluster of 4 cells induced by 20 mM glucose stimulation. The temporal responses were analyzed from the two ROIs shown in the left image and each data trace corresponds to the ROI with the same color.

FluoZin-3:Zn^{2+} complex. The observed fluorescence increases were only induced by insulin secretagogues such as glucose and K$^+$, not by buffer, and the increases were dependent on the presence of extracellular Ca^{2+} as expected for exocytotic release. The possibility of inducing fluorescence increases by local pH changes during exocytosis is also excluded by the pH independence of FluoZin-3:Zn^{2+} fluorescence signals at biological pH range.

Compared to Zinquin, FluoZin-3 offers several advantages for monitoring Zn^{2+} release from cells with the most significant being the improvement in sensitivity. The fluorescence increases seen during stimulated secretion were 32-fold (Figure 4-3A) and 185-fold (4-3B) over baseline while typical measurements with Zinquin yielded only ~5-fold enhancement over baseline. The sensitivity of detection was also examined by a titration calibration with $ZnCl_2$ under the same conditions as the imaging experiments, yielding a limit of detection of ~10 nM of total Zn^{2+}, while previously imaging experiments with Zinquin had a limit of detection of ~0.5 μM. This improvement is attributed to greater sensitivity of the dye and lower background autofluorescence from both the cell and surrounding solution due to the longer wavelength for excitation. Furthermore, as a tetraanionic dye, FluoZin-3 is less permeant to the cell than the monoanionic Zinquin (Figure 4-2B) and creates lower background fluorescence and less fluctuation inside the cells.

The improved sensitivity also facilitates a better characterization for the transport of released Zn^{2+} away from the cells. As shown in Figure 4-3, released Zn^{2+} can be detected at least 20 μm away from the cell surfaces, while in previous work with Zinquin Zn^{2+} was only detected in the immediate vicinity of the cell (1-2 μm away from the cell surface). The transport of released Zn^{2+} was further analyzed using four ROIs with different distances away from the cell surface. As shown in Figure 4-4A, the fluorescence responses decrease as the ROIs move away from the cell, consistent with diffusional transport of released Zn^{2+}. Because of the high Zn^{2+} affinity of FluoZin-3 and 1:1 FluoZin-3:Zn^{2+} binding, the fluorescence response is expected to be proportional to the total [Zn^{2+}] present in the extracellular space if the total [Zn^{2+}] is less than the total FluoZin-3 concentration. To determine the total [Zn^{2+}], a two-point calibration was performed following each experiment, which gave the background fluorescence in the absence of Zn^{2+} (F_{min}) and the maximum fluorescence at saturated Zn^{2+} level (F_{max}). The total [Zn^{2+}] can be calculated using the following equation:

$$\text{total}\,[\text{Zn}^{2+}] = \text{total}\,[\text{FluoZin-3}] \times \frac{F - F_{\min}}{F_{\max} - F_{\min}} \qquad (4.1)$$

where F is measured fluorescence intensity at a given [Zn^{2+}]. The total [Zn^{2+}] at the ROI 1 in Figure 4-4A was 600 nM at peak response and the total [Zn^{2+}] at peak response decreased to 120 nM at the ROI 4. In Figure 4-4B, the profile of total [Zn^{2+}] on a line moving away from the cell surface is presented. The data was fit with a diffusion-controlled model. In this model, Zn^{2+} release was considered as diffusion from an instantaneous point source on a planar surface into a semi-infinite media. At any given point of time, the concentration at a distance *r* from an instantaneous point source into a semi-infinite media is given by (Crank, 1975):

$$\begin{aligned} C(r,t) &= \frac{M}{4(\pi D t)^{\frac{3}{2}}} \exp(-r^2/4Dt) \\ &= C(0,t)\exp(-r^2/4Dt) \end{aligned} \qquad (4.2)$$

where C is the concentration of diffusing substance, which is FluoZin-3:Zn^{2+} complex in this case, D is the diffusion coefficient of FluoZin-3:Zn^{2+} complex, M is the amount of substance (Zn^{2+}) released at time 0. If the concentration is normalized against the concentration at distance 0, the equation becomes

$$C(r,t) = \exp(-r^2 / 4Dt) \tag{4.3}$$

which is the equation used to fit the data in Figure 4-4B. A diffusion coefficient for FluoZin-3:Zn^{2+} complex is taken as 3.4×10^{-6} cm^2/s, a parameter measured for fluorescein-labeled biotin, a compound with similar molecular weight as the FluoZin-3:Zn^{2+} complex, in an aqueous solution (Kamholz et al., 2001). Although the diffusion model used is approximate because the concentration profile at any given moment may be contributed from release of multiple secretory vesicles at different locations on the cell surface, the good correlation between experimental and theoretical data does suggest that the transport of released Zn^{2+} away from the cell is controlled by diffusion.

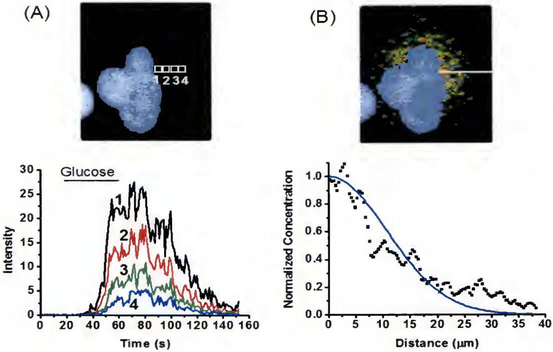

Figure 4-4. Diffusional transport of released Zn^{2+} from cells. (A) The temporal responses of Zn^{2+} secretion were analyzed using the four ROIs (4 μm^2) as indicated as 1, 2, 3, 4 in the image. The traces from top to bottom correspond to the ROI 1, 2, 3, 4, respectively. Images analyzed are same as in Figure 4-3B. (B) Concentration profile at the line shown in the above image. Image used for analysis is at time 50 s. Before analysis, the image was smoothed with a 5 % 5 kernel in order to reduce the pixel-to-pixel noise in the image. The blue curve is the best fitting results using equation 4.3. The correlation coefficient $R^2 = 0.85$.

Another feature of observed Zn^{2+} release is the large fluctuations in detected total $[Zn^{2+}]$ following stimulation as shown in Figure 4-4A. This behavior is expected because Zn^{2+} is released from secretory vesicles as distinct packets by exocytosis. At the temporal resolution used for these experiments (1.07 s per image), it is not possible to resolve release from individual vesicles.

Imaging of Zn^{2+} Release with High Temporal Resolution

In order to resolve Zn^{2+} release from individual secretory vesicles, the improvement in temporal resolution of imaging was investigated. The S/N has been a major concern in high-speed imaging. The high imaging speed often results in short exposure time, where intrinsic statistical noise becomes obvious. Poisson statistics states that if the average result of repeated measurements is n photons per measurement, the chance that any specific measurement is in the range between $n+\sqrt{n}$ and $n-\sqrt{n}$ is only 63% (Pawley, 1995). The confocal microscope used in this work scans a full frame in 33 ms, which gives an exposure time of 135 ns for each pixel. For such short exposure time, high fluorescence signals are required for imaging with good S/N. In previous work with Zinquin, it was not possible to detect Zn^{2+} secretion at this image acquisition rate because the signal level of Zinquin is too low even after Zn^{2+} binding. With the much brighter fluorescence of FluoZin-3, it has been possible to detect Zn^{2+} release with higher temporal resolution and isolated Zn^{2+} release events from cells have been observed.

Observation of isolated Zn^{2+} release events. Figure 4-5 shows Zn^{2+} release from cells measured with an image acquisition rate of 60 Hz. Distinct fluorescence transients with durations between 100 to 300 ms were observed from one localized region but not from other regions around the cells. These fluorescence spikes are due to the detection of rapid changes in total [Zn^{2+}] outside the cells following distinct release events. These sharp changes in [Zn^{2+}] are presumably due to the release of Zn^{2+} in packets from individual secretory granules by exocytosis because the time scale of these fluorescence spikes is expected for individual exocytotic events from β-cells (Huang et al., 1995).

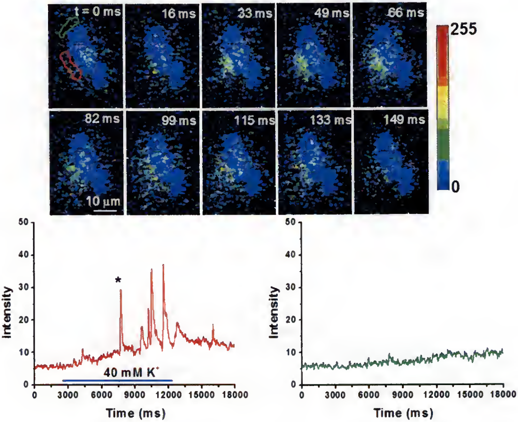

Figure 4-5. Detection of Zn^{2+} release with milliseconds temporal resolution. A cluster of three cells was stimulated by 40 mM K^+ for 10 s and images were acquired continuously at a rate of 16.5 ms per image (60 Hz, 2-band scanning). Images shown are in raw intensities pseudo-colored according to the scale bar on the right. The time courses of Zn^{2+} release were analyzed using the two ROIs the cells as shown in the first image. The traces in the bottom plots correspond to the ROIs in the same color. Images in the montage show the same fluorescence burst as the one marked with '*' in the bottom plot.

The montage in Figure 4-5 shows a series of images corresponding to the marked fluorescence transient, which has a total duration of ~ 150 ms. As shown the images appear to be much noisier than those acquired at lower temporal resolution. The observed Zn^{2+} clouds outside the cell initially appeared at one spot on the cell surface and then became larger and brighter and gradually disappeared as the release event ended and the released Zn^{2+} diffused away from the cell surface. Isolated Zn^{2+} release events similar to those shown in Figure 4-5 were observed in 15 separate experiments when cells were stimulated by 40 mM K^+ stimulation. In all these experiments, either single cells or cell clusters consisting of 2-5 cells were used.

Identification of the site of release. Similar to those observed at lower temporal resolution, the released Zn^{2+} signals can be clearly observed at over 10 μm away from the cell surface (Figure 4-5). Although diffusion of released Zn^{2+} leads to the detection of a large Zn^{2+} cloud, the site of Zn^{2+} release (the source of diffusion) should have the highest $[Zn^{2+}]$. To locate the release site, the data were analyzed by spatially mapping the release site. Identical 2 μm square ROIs along the release site were used to analyze the temporal responses of the release event (Figure 4-6). With the five regions along the cell surface, the response from the middle region (ROI 3) displays the sharpest peak and highest amplitude, suggesting that the release site is localized within this region. As the regions move away from the release site, the detected fluorescence spikes are broader and with lower total $[Zn^{2+}]$ at peak time, which is consistent with the diffusional transport of released Zn^{2+} away from the cell. The same peak broadening and decrease in peak amplitude were observed for regions moving away from the cell surface (ROI 6 and 7 compared to ROI 3). The total $[Zn^{2+}]$ was converted from fluorescence intensities with a calibration performed as described in the earlier section. With images acquired at 60 Hz, the detection limit for total $[Zn^{2+}]$ was estimated to be 40 nM (S/N of 3), which is about four times poorer than that obtained at lower temporal resolution. This behavior is expected due to the increased intrinsic noise as the imaging speed increases.

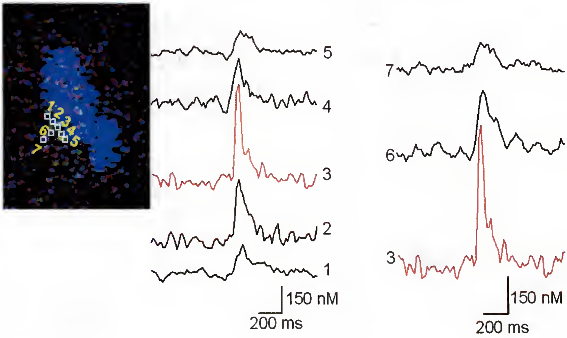

Figure 4-6. Identification of the release site of a single release event. The release event analyzed was same as the one in Figure 4-5 marked with '*'. Seven identical ROIs were aligned outside the releasing area with the ROI 1 to 5 lying against cell surface and ROI 6 and 7 moving away from the cell. The time courses of Zn^{2+} release from all regions are plotted on the same time scale. The amplitudes of the spikes are indicated as total $[Zn^{2+}]$ in nM.

Spatially resolved release events. The spatial and temporal resolution of this technique also allows resolution of events that occur nearly simultaneously but at different points. Figure 4-7 illustrates two release events that occurred within 300 ms of each other but were from two release sites ~8 μm apart. When data were analyzed using a relatively large ROI covering both release sites, the fluorescence spike appears to be resulting from a single release event with a relatively broad peak; however, when data were analyzed by several small ROIs along the release site, two individual release events were resolved and identified. The spatial resolution of this imaging technique, therefore, provides additional resolving power for temporally overlapped release events. In contrast, such temporally overlapped exocytotic events may not be resolved by single-point sensors such as the microelectrodes and patch pipettes used in amperometric and capacitance measurements of exocytosis.

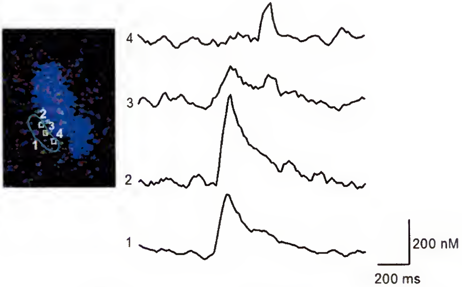

Figure 4-7. Spatially resolved analysis of temporally overlapped fluorescence spikes. The fluorescence spike occurred at the time ~12000 ms in Figure 4-5 was used for this analysis. One large ROI 1 and three smaller ROI 2, 3, and 4 were used for analysis the temporal responses of Zn^{2+} release. The diameter of the small square regions is 2 μm.

Figure 4-8 shows an example of observation of multiple fluorescence spikes from a cell stimulated by K^+. Some of the spikes are not baseline resolved and it is difficult to determine whether each spike corresponds to the detection of one single release event or multiple release events by only examining the temporal trace. By using smaller ROIs to map the release site similar to that in Figure 4-7, it was found that the observed fluorescence spikes were results of at least 22 independent release events (S/N >3). Beside the observation of multiple spikes, a slow increase in baseline intensity was also observed following the stimulation, indicating an increase in Zn^{2+} level around the cell. This slow increase in Zn^{2+} level may be due to the released Zn^{2+} that has not diffused away. Zn^{2+} release events occurred below or above the focal plane may also contribute to this slow increase in Zn^{2+} level.

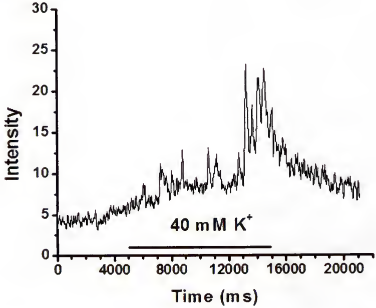

Figure 4-8. Fluorescence spikes evoked by K^+ stimulation. The cell was stimulated with K^+ for 10 s and images were acquired at 60 Hz. Images were analyzed using an ROI around the release site as in Figure 4-5.

Temporal and spatial characteristics of isolated release events. Figure 4-9A shows examples of isolated fluorescence spikes from five different cells. All spikes show a relatively fast rise in total [Zn^{2+}] followed by a slow decay, which is expected for single exocytotic release with a rapid release of the vesicular contents followed by diffusion of the release products from the point of vesicle fusion (Schroeder et al., 1992). The rise time of a spike is defined as the time between the initiation of the spike and the maximum point of the spike. The rise times of spikes were 16-50 ms and the average duration of spikes was 175 ± 50 ms (n = 78 spikes from 15 different cells). In this analysis, only those spikes with S/N >3 and well resolved from their neighboring spikes were used and all analysis was performed using a 2 μm square ROI at the release site. The temporal resolution of these measurements is 16.5 ms, which prevents accurate measurements of the rise times. Despite this limitation, the observed rise times are in good agreement with those measured by amperometry for the detection of insulin secretion from single cells, which gives the typical rise times of 25-40 ms. In previous amperometric measurements, a relatively longer total duration of 270 ± 165 ms was obtained for current spikes that correspond to the detection of insulin release from single vesicles (Huang et al., 1995, Kennedy et al., 1996). The difference between the observed durations could be due to several differences in amperometric detection and fluorescence imaging of exocytotic release events. First, the microelectrode used in amperometry is positioned over the cell surface, which presents a diffusion barrier for the release products, while in this fluorescence measurements, the release product is free to diffuse away from the cell surface. Second, in amperometric measurements, the released electroactive product is consumed at the electrode surface, while the released product is not consumed in fluorescence imaging. Finally, amperometric detected release events could occur as far as 6-10 μm from the electrode surface if the release events originate from the base of the cell and the cell is considered as a hemisphere on a glass coverslip (Jankowski et al., 1993). In contrast, the fluorescence spikes are always analyzed at the site of release. Despite the difference, the durations of observed fluorescence spikes are expected for the detection of Zn^{2+} release from individual exocytotic events.

In Figure 4-9B, the five spikes were normalized and superimposed. Figure 4-9C shows the calculated spike shapes based on an instantaneous point source diffusion model (Equation 4.2), a model previously used to analyze amperometric data corresponding to the detection of single exocytotic events (Schroeder et al., 1992; Jankowski et al., 1993). The diffusion-controlled model predicts much narrower peaks than those observed experimentally. Based on the model, the rise time should be 4 ms for a peak analyzed at 3 μm away from the point source and 16 ms at 6 μm away from the source. Both numbers are significantly shorter than the rise times observed for the fluorescence spikes (Figure 4-9B and 4-9C).

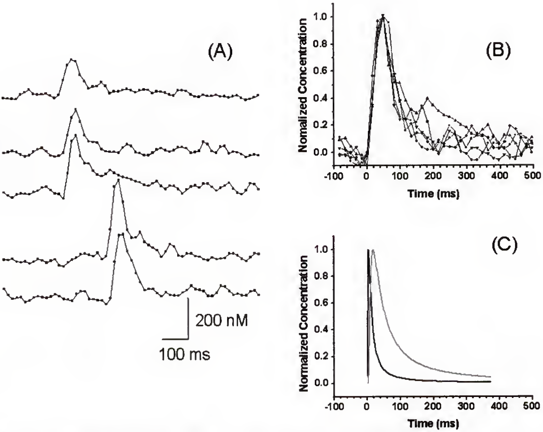

Figure 4-9. Shapes of isolated fluorescence spikes. (A) Examples of isolated fluorescence spikes obtained from five different cells. In all experiments, images were recorded at 60 Hz. The release sites of all release events were identified similarly as that in Figure 4-6 and each spike shown here was analyzed from a region close to the release site. The interval between two adjacent data points in the traces is 16.5 ms. (B) Spikes from (A) normalized by the peak [Zn^{2+}] and superimposed on the same time scale. (C) Diffusion controlled spikes based on the instantaneous point source diffusion model. Traces plotted are the dynamic concentrations at 3 μm and 6 μm away from the point source. Concentrations were calculated from equation 4.2.

Since confocal imaging collects signals from ~ 1-μm-thick slice through the cell and the focal plane is typical positioned in the middle of the cell, it is possible that the actual release sites are located below or above the focal plane. Because all the fluorescence spikes were analyzed with a 2 μm square region close to the release point, it would be expected to observe broader spikes with lower amplitudes due to diffusion if the actual release spot is more than 3 μm below or above the focal plane. In Figure 4-9, the spikes selected were with the narrowest shapes and the largest amplitudes. Therefore, it is reasonable to assume that the release spot is close to the focal plane and the distance between the point of analysis and the actual release point is 1-3 μm for these observed spikes. The rise times of the observed fluorescence spikes, therefore, are much longer than those predicted by diffusion. These data suggest that the release process is not an instantaneous process controlled only by diffusion, but rather a kinetically controlled process.

Besides the temporal characteristics, the spatial characteristics of individual release events have also been examined. In Figure 4-10, the total Zn^{2+} concentration profiles along a line away from the release point were plotted for three different points of time during a single release event. The concentration profiles were compared to those predicted by instantaneous point source diffusion model (gray curves, equation 4.2). As time increases, both the measured and calculated concentration profiles display a decrease in amplitude and a broadening in shape; however, the decrease in amplitude for the calculated curves is greater than that actually observed. For example, for the calculated curves, the maximum concentration at distance 0 and t =50 ms is 5.5-fold less than that at t = 16 ms. In contrast, the measured concentration at distance 0 and t = 50 ms is only 1.4-fold less than that at t = 16 ms. Therefore, the diffusion model fails to predict the temporal changes in concentration. Despite this, if the amplitudes of the calculated curves at t = 50 and 83 ms were normalized to fit the measured concentration profiles, the curves (gray for t = 16 ms, black for t = 50 ms and 83 ms) fit well with the measured concentration profiles at all three points of time with correlation coefficients (R^2) > 0.8.

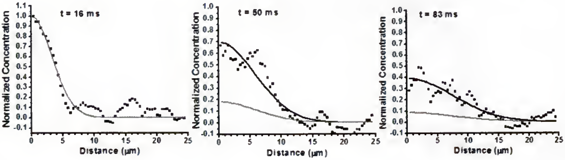

Figure 4-10. Normalized concentration profiles at different times during a single exocytotic release event. The release event analyzed is the same as shown in the montage of Figure 4-5. The image of first observation of the released Zn^{2+} cloud was assigned as t =16 ms (the 3rd image in the montage). The data points corresponds to detected Zn^{2+} concentrations along a line starting from the release point away from cell surface. The concentrations were normalized against the maximum concentration measured at the release spot and t = 16 ms. Images used for analysis were smoothed with a 5 % 5 kernel in order to reduce the pixel-to-pixel noise in the images. All gray curves were calculated from equation 4.2 based on the instantaneous point source diffusion model and normalized against $C(0, t_0)$, where t_0 = 16 ms. For t = 50 ms and 83 ms, the calculated gray lines were normalized to fit the experimental data by multiply a constant for all data points in the curves. The correlation coefficients (R^2) of the fitting are 0.93, 0.89, 0.82 for t = 16, 50, and 83 ms, respectively.

Discussion

With the use of a novel Zn^{2+} fluorophore FluoZin-3, improvements in sensitivity and temporal resolution for the detection of Zn^{2+} release at the single-cell level have been demonstrated. The greater sensitivity and temporal resolution have allowed a better characterization of the dynamics of Zn^{2+} release and the mass transport of released Zn^{2+} in the extracellular space. With a temporal resolution of 16.5 ms, isolated fluorescence bursts have been observed from individual cells following K^+ stimulation. These isolated fluorescence spikes appear to be due to the detection of Zn^{2+} concentration pulses generated by the release of Zn^{2+} in packets from individual secretory vesicles by exocytosis. The following characteristics of observed fluorescence spikes summarize the evidence that support this conclusion:

i) Rapid release of vesicular Zn^{2+} by exocytosis should lead to a Zn^{2+} concentration pulse with the highest Zn^{2+} concentration at the site of release and the released Zn^{2+} should diffuse away rapidly from the cell surface. Consistent with this hypothesis, the fluorescence spike has the highest amplitude and sharpest shape when analyzed at a region close to the site of release, while the amplitude decreases and peak width increases when analyzed in regions away from the site of release (Figure 4-5).

ii) The rise times and durations of observed fluorescence spikes are expected for the detection of individual exocytotic events (Huang et al., 1995; Kennedy et al., 1996).

iii) Large heterogeneity in peak $[Zn^{2+}]$ of isolated fluorescence spikes has been observed (Figure 4-11), which presumably reflects different amounts of Zn^{2+} released from vesicles. The average peak $[Zn^{2+}]$ at the site of release for the observed fluorescence spikes is 150 ± 95 nM (n = 78, Figure 4-11). This heterogeneity is consistent with previous observation of large variation in the vesicle sizes by electron microscopy (Larsson et al., 1976). An average diameter of 300 ± 61 nm was reported for vesicles in human β-cells. Large heterogeneity in spike areas was also observed in amperometric detection of insulin secretion (Huang et al., 1995), suggesting the heterogeneity in the amount of insulin contained within individual vesicles.

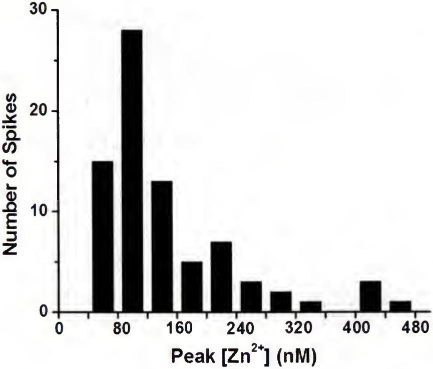

Figure 4-11. Distribution of peak [Zn^{2+}] of isolated fluorescence spikes. Total 78 spikes from 15 cells were analyzed.

In addition to above characteristics, all the spikes used for analysis are isolated from their neighboring spikes and have smooth shapes expected for release from single vesicles. If a single fluorescence spike actually results from two release events that occurred within 200 ms, with the additional spatial resolving power of this imaging technique, it could be resolved into individual spikes as shown in Figure 4-7 if these events are generated from different points. Given the low frequency of spike occurrence in some cells following K$^+$ stimulation, the probability of two release events occurring at the same release site within 200 ms is low if the exocytotic process is stochastic (Wightman et al., 1991). For those cells with a high frequency of spike occurrence, the fluorescence spikes are not baseline resolved (See example in Figure 4-8). In these cases, it would be difficult to determine whether a given spike is resulting from single vesicle or multiple vesicles. Taken together, these results strongly support the hypothesis that the isolated fluorescence spikes observed during stimulated Zn^{2+} release from individual β-cells correspond to the detection of Zn^{2+} release in packets from individual secretory vesicles by exocytosis.

The temporal and spatial characteristics of isolated fluorescence spikes have been examined and compared to the results generated from an instantaneous point source diffusion model. The shapes of observed concentration profiles for a given release event agree well with the diffusion results (Figure 4-10), which suggests the released Zn^{2+} ions are transported away from the cell surface by diffusion. However, the diffusion model failed to predict the temporal characteristics of individual release events. First, the spikes predicted by diffusion are much narrower than the measured fluorescence spikes (Figure 4-9). Second, the measured changes in amplitudes of the concentration profiles at different points of time are much less than those expected from diffusion (Figure 4-10). Finally, when fluorescence spikes are analyzed at different distances from the release sites, the decrease in peak $[Zn^{2+}]$ with increasing distance is less than that expected by diffusion. For example, when spikes were analyzed at the site of release and 3 μm away from the release sites, the peak $[Zn^{2+}]$ show only an average of 1.8-fold of difference, while the diffusion model predicts at least 7-fold of difference in peak $[Zn^{2+}]$. Taken together, these data suggest that the vesicular release process is not an instantaneous diffusion-controlled process, but rather a kinetically controlled process. Previous results with amperometric measurements of insulin secretion have also suggested that the kinetics of insulin release is controlled by the dissolution and dissociation of the insulin-Zn^{2+} solid complex (Aspinwall et al., 1997). Vesicular Zn^{2+} release would be expected to have the same release kinetics as insulin due to the co-storage and co-release of Zn^{2+} and insulin. Our results suggest that this kinetically controlled process occurs on a time scale of approximately 16-50 ms based on the measurements of rise times of fluorescence spikes. Because all fluorescence spikes were analyzed from regions in the vicinity (1-3 μm) of the release sites and the rise times predicted by diffusion are < 4 ms at such distances, the observed rise times of fluorescence spikes reflect the time scale of the kinetically controlled process.

To our knowledge, the work presented here provides the first temporally resolved measurements of chemical release resulting from individual exocytotic events by fluorescence imaging. Previously, amperometry with microelectrodes has provided such temporal resolution in monitoring chemical secretion from single cells, even at the level of single exocytotic events (Chow et al., 1992; Chen et al., 1994; Wightman et al.; 1991; Huang et al., 1995). As a technique for monitoring exocytosis, this imaging approach will be complementary to amperometry. Amperometry is limited to the detection of electrochemical active species, while this approach is so far limited to Zn^{2+}. With the development of fluorescent probes for other compounds, this approach could potentially be used for monitoring secretion of other chemical species from living cells. One advantage of this fluorescence imaging approach for measuring exocytosis is its spatial resolution. It has been possible to examine the spatial characteristics of an individual exocytotic event such as the release site, the spike shapes at different distances from the release site (Figure 4-6), and the concentration profiles in the extracellular space (Figure

4-10). It has been not possible to attain such spatial information from individual exocytotic events by amperometry with a microelectrode since a microelectrode is inherently a single-point sensor. Furthermore, since Zn^{2+} is co-secreted product with insulin from pancreatic β-cells and with glutamate from zinc-containing hippocampal neurons, this technique should be a novel tool for the fundamental studies of exocytosis on these cell types and for monitoring the kinetics of Zn^{2+} and insulin secretion, or Zn^{2+} and glutamate secretion at the single-cell level with high temporal resolution.

CHAPTER 5

TEMPORAL AND SPATIAL PATTERNS OF OSCILLATORY Zn^{2+} SECRETION FROM CLUSTERS OF PANCREATIC β-CELLS AND ISLETS OF LANGERHANS REVEALED BY FLUORESCENCE IMAGING

Introduction

Pancreatic islets store Zn^{2+} at a high concentration relative to other tissues (Zalewski et al., 1994). Most islet Zn^{2+} is associated with secretory granules and is either labile or in the form of crystals containing hexamers of insulin with two or more Zn^{2+} per hexamer (Blundell et al., 1972). Free Zn^{2+} has also been detected in the extra-granular space of β-cells where it may act as a reservoir for the granules (Figlewicz et al., 1984). Another, albeit much less significant source of islet Zn^{2+} is granules of α-cells (Kristiansen et al., 2001). The complete role of Zn^{2+} in islets has yet to be elucidated. Zn^{2+} in β-cell granules is believed to be important for stable storage of insulin within vesicles prior to release by exocytosis. During exocytosis, Zn^{2+} is also co-released with insulin from secretory granules of β-cell (Emdin et al., 1980; Formby et al., 1984; Gold and Grodsky, 1984; Grodsky and Schmid-Formby, 1985; Foster et al., 1993). Zn^{2+} released from β-cells may act as a paracrine agent in promoting pancreatic islet cell death, especially in hyperinsulinemic states (Kim et al., 2000). Secreted Zn^{2+} may also activate ATP-sensitive K^+ channels on β-cells and therefore serve an autoregulatory role in secretion (Bloc et al., 2000). Given the potential role for released Zn^{2+} in affecting islet function, it is of interest to better understand the regulation and dynamics of its secretion from islet cells.

Because Zn^{2+} is co-stored and co-released with insulin, it is expected that the dynamics of its release would be the same as those for insulin. Dynamics of insulin secretion have been studied extensively and are quite complex. *In vivo* insulin levels are pulsatile (Lang et al., 1979; Polonsky et al., 1988a) and loss of regular oscillations in insulin release is an early symptom of type 2 diabetes (Polonsky et al., 1988b; O'Rahilly et al., 1988). Secretory oscillations with a period of 2-5 min have been reproduced *in vitro* with groups of islets and single islets, indicating that the oscillations involve a mechanism inherent to the islets (Gilon et al., 1993; Bergsten and Hellman, 1993b; Bergsten et al., 1994; Barbosa et al., 1998). In addition to secretory oscillations, oscillations in intracellular free Ca^{2+} concentration ($[Ca^{2+}]_i$) have also been observed in islets and cell clusters (Valdeolmillos et al., 1989; Santos et al., 1991; Gylfe et al., 1991; Jonkers et al., 1999). The secretory oscillations appear to be driven by oscillations in $[Ca^{2+}]_i$ as temporal correlation between secretory oscillations and slow $[Ca^{2+}]_i$ oscillations has been observed by simultaneous measurements of $[Ca^{2+}]_i$ and insulin secretion from single islets (Gilon et al., 1993; Bergsten et al., 1994; Gilon and Henquin, 1995).

Oscillatory patterns of insulin and Zn^{2+} secretion may be more complex than those previously observed because $[Ca^{2+}]_i$ in islets display patterns other than the slow oscillations including fast pulses with a period of 10-20 s and fast oscillations superimposed on slow oscillations (Valdeolmillos et al., 1989; Bergsten et al., 1994). It has been problematic to correlate the faster $[Ca^{2+}]_i$ fluctuations to insulin secretion due to the difficulty of measuring insulin release at the required temporal resolution using classical immunoassays (Rosario et al., 1986; Gilon et al., 1993; Bergsten and Hellman, 1993a); however, fast oscillations in insulin secretion have been reported (Bergsten and Hellman, 1993b). In addition, good correlation between fast oscillations in $[Ca^{2+}]_i$ and secretion was observed by amperometric measurement of 5-HT secretion (the 5-HT was loaded into the islets by a prior incubation) from single islets (Barbosa et al., 1998).

In this work, we have investigated the spatial and temporal characteristics of oscillatory Zn^{2+} secretion from islet cell clusters and single islets using a recently developed fluorescence imaging approach (Chapter 2; Qian et al., 2000). In the method, cells are incubated in buffer containing a membrane impermeant, fluorogenic Zn^{2+} specific indicator. When Zn^{2+} is released into the extracellular space, it reacts with the Zn^{2+} indicator to form a fluorescent complex, which is detected by confocal fluorescence microscopy. With this approach, Zn^{2+} secretion from single β-cells has been previously monitored to study the spatial organization of exocytosis at β-cells (Chapter 3; Qian and Kennedy, 2001). More recently, we have described the improvements in sensitivity and temporal resolution of this approach with the use of a novel Zn^{2+} probe FluoZin-3 (Chapter 4; Gee et al., 2002). The goal of this work is to characterize the spatial and temporal patterns of Zn^{2+} release, and by inference insulin release, from islets and islet cell clusters using the improved imaging approach.

Experimental

Chemicals

FluoZin-3 was prepared at Molecular Probes as previously described (Gee et al., 2002). Type XI collagenase, HEPES, nifedipine, and thapsigargin were obtained from Sigma. Tetrakis-(2-pyridylmethyl) ethylenediamine (TPEN) and Fura Red acetoxymethyl ester (AM) were from Molecular Probes. Unless otherwise stated, all chemicals for islets and cell culture were obtained from Life Technologies. All other chemicals were from Fisher unless noted and were of the highest purity possible.

Isolation and in Vitro Culture of Mouse Islets and β-cells

Pancreatic islets were isolated from CD-1 mice as described in Chapter 2. Briefly, islets were isolated by ductal injection with collagenase and handpicked under a dissecting microscope. For islet study, 1 to 5 islets were directly plated onto a 25 mm diameter coverslip in tissue culture dish (Corning). For isolated cell study, islets were dispersed into single cells and cell clusters by shaking in 0.025% trypsin for 6 min at 37° C and were plated onto 25 mm diameter coverslips in tissue culture dishes. Islets and dispersed cells plated on coverslips were incubated in RPMI 1640 medium containing 10% fetal bovine serum, 100 U/mL penicillin and 100 μg/mL streptomycin at 37° C, 5% CO_2, pH 7.4. Islets were used for experiments 3 to 7 days after isolation. Dispersed cells were used for experiments 1 to 2 days after isolation.

Confocal Imaging of Cells and Islets

All imaging experiments were performed on a Nikon RCM 8000 laser scanning confocal microscope (See description in Appendix A). A Nikon 40x, 1.15 NA, UV-corrected water-immersion objective was used for imaging dispersed cells and a Nikon 20x, 0.75 NA objective was used for imaging single islets.

Kreb's Ringer buffer (KRB, 118 mM NaCl, 5.4 mM KCl, 2.5 mM $CaCl_2$, 1.2 mM $MgSO_4$, 1.2 mM KH_2PO_4, 20 mM HEPES, 3.0 mM D-glucose) with minimum background Zn^{2+} level for imaging was prepared as previously described (Chapter 4; Thompson et al., 2000). Cells or islets to be imaged were bathed in KRB containing 2 μM FluoZin-3 and maintained at 37° C on the stage of the microscope by a microincubator (Medical Systems, Inc.). For imaging cell clusters, the buffer was titrated with a high affinity non-fluorescent Zn^{2+} chelator TPEN to deplete the trace amount of Zn^{2+} present in the buffer in order to reduce background fluorescence. The typical final concentration of TPEN in the buffer was ~200 nM. For imaging islets, the buffer was used without addition of TPEN. For short periods of stimulation, secretagogues were applied to the cells by pressure ejection at 3-6 psi from micropipettes positioned ~60 μm from the cells. Stimulation (30 mM K^+ or 20 mM glucose) solutions contained the same concentration of FluoZin-3 as the bathing buffer. For continuous stimulation with an elevated concentration of glucose, cells were either directly incubated in buffer containing the desired concentration of glucose or incubated in buffer containing 3mM glucose and aliquot of concentrated glucose (1 M) was added to obtain the desired concentration at the time of stimulation.

Zn^{2+} images with FluoZin-3 were acquired with 488 nm excitation and 525 ± 10 nm band-pass emission filter. UV autofluorescence images were acquired with 351 nm excitation and 480 ± 10 nm emission filters. All images were stored on an optical disc cartridge (TQ-FH332, Panasonic) by an optical disc recorder (TQ-3038F, Panasonic) for later analysis.

Simultaneous Imaging of Zn^{2+} Secretion and Intracellular Ca^{2+} Concentration

Cells adhered on coverslips were loaded with 3 μM Fura Red AM, a red emission Ca^{2+} indicator, for 40 min in RPMI medium at 37° C, 5% CO_2. After loading, cells were washed with KRB twice and incubated in KRB containing 2 μM FluoZin-3. Both FluoZin-3 and Fura Red are excited at 488 nm, but their emission maximums are at 516 nm and 655 nm, respectively. Therefore, FluoZin-3 Zn^{2+} signal and Fura Red Ca^{2+} signal can be simultaneously recorded at two separated channels using a 550 nm cut-off dichroic mirror and a 525 ± 10 nm band-pass filter for FluoZin-3 detection and a 595 nm long-pass filter for Fura Red detection. Under these experimental settings, no interference in fluorescence between these two dyes was observed.

Data Analysis

Images for analysis were played back from the optical disk cartridge and captured and analyzed using Simca image analysis software (C-IMAGING Systems). For plots of fluorescence intensity as a function of time, regions of interest (ROI) around the cells or covering the cells were highlighted and average intensities within the ROIs were calculated for a series of images. For simultaneous measurements of $[Ca^{2+}]_i$ and Zn^{2+} release, FluoZin-3 and Fura Red signals were analyzed independently by playback images in single-channel mode. ROIs used for Fura Red signal analysis were drawn covering the cells, while ROIs were drawn outside the cells for FluoZin-3 signal analysis. Since Fura Red is a single-wavelength dye and its fluorescence decreases as $[Ca^{2+}]_i$ increases, changes in $[Ca^{2+}]_i$ were expressed as inversed F_0/F_1 ratios, where F_0 was the fluorescence intensity of the initial image during the recording (Guerineau et al., 1998; Aspinwall et al., 2000). The increase in F_0/F_1 ratio indicates an increase in $[Ca^{2+}]_i$ All means are reported as ± 1 standard error of the mean (SEM).

Results

Zn^{2+} Secretion Induced by Short Periods of Stimulation

Zn^{2+} secretory dynamics from cell clusters was first investigated with short periods of stimulation. Preliminary results of Zn^{2+} secretion from small cell clusters induced by glucose stimulation have been described in Chapter 4. Here, characterization of the Zn^{2+} concentrations outside the cells as well as in the interstitial spaces within cell clusters were attempted. Figure 5-1A shows an example of Zn^{2+} secretion from cell cluster induced by short period of glucose stimulation. Large increases in fluorescence due to the detection of released Zn^{2+} in the extracellular space were observed upon stimulation. The total Zn^{2+} concentrations detected in the extracellular space were estimated by a two-point calibration as described in Chapter 4. Using this approach, the maximum Zn^{2+} level detected for the ROI close to the cell was ~400 nM and it decreased to ~100 nM at the ROI 20 μm away from the cell surface (Figure 5-1A). The maximum Zn^{2+} concentration observed in a 3 × 3 μm ROI at the active releasing area of cells was highly variable with a range of 60 nM to 600 nM and an average of 160 ± 90 nM (n = 35 cell clusters). Zn^{2+} release signals could also be occasionally observed in the interstitial spaces of cell clusters (Figure 5-1B). The increases in fluorescence observed inside the cluster can be interpreted as detection of Zn^{2+} released into interstitial spaces within the cluster since the focal point of the images was at the middle of the cells. As with the signals observed at the periphery, these increase during the stimulus and quickly dissipate as the stimulus is removed. The fluorescence intensities observed in the interstitial spaces of cell clusters are frequently higher than those observed outside the cells (Figure 5-1B), indicating some released Zn^{2+} trapped in these regions.

Simultaneous Measurements of $[Ca^{2+}]_i$ and Zn^{2+} Secretion

Simultaneous monitoring of Zn^{2+} secretion and $[Ca^{2+}]_i$ was achieved by using FluoZin-3 and the intracellular Ca^{2+} indicator Fura Red (Kurebayashi et al., 1993). As shown in Figure 5-2, correlated responses in $[Ca^{2+}]_i$ and Zn^{2+} secretion from small clusters (5 to 15 cells) were observed when cells were stimulated by a brief application of high K^+ or glucose. Stimulation with 40 mM K^+ induced an immediate rise in $[Ca^{2+}]_i$ while secretion followed the initial rise in $[Ca^{2+}]_i$ with a latency of 3 ± 1 s (n = 6). Stimulation with 20 mM glucose resulted in a relatively slow and delayed rise in $[Ca^{2+}]_i$ with secretion following the initial rise in $[Ca^{2+}]_i$ with a latency of 14 ± 2 s (n = 22).

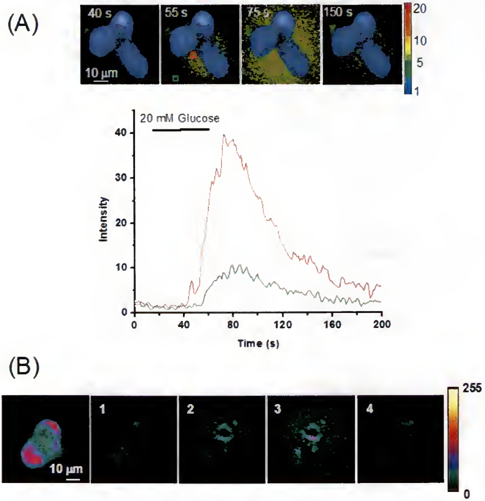

Figure 5-1. Imaging of Zn^{2+} secretion from β-cells. (A) Secretion observed in the extracellular space. Images are shown in fluorescence intensity ratios against a UV autofluorescence image in order to highlight fluorescence enhancements. All images were acquired at 1 Hz. The time of each image acquired is indicated in seconds. The temporal responses were analyzed using two identical ROIs (3 × 3 μm^2) outside the cells as indicated in the 2nd image. (B) Secretion observed in the interstitial spaces within a cell cluster. Images shown are in raw intensities pseudo-colored according to the scale-bar on the right. The image on the left is an autofluorescence image of the cells acquired with UV excitation. Other images are Zn^{2+} images. Image 1 was acquired under basal conditions. Images 2, and 3 were acquired after 20 mM glucose was applied and image 4 was acquired 2 min after the removal of stimulation.

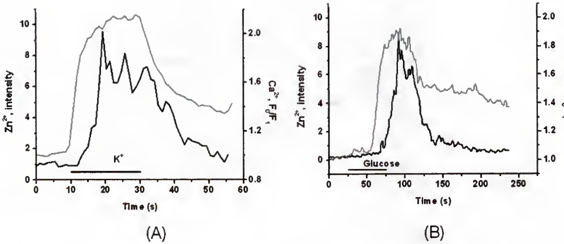

Figure 5-2. Simultaneous measurements of $[Ca^{2+}]_i$ and Zn^{2+} secretion from small clusters of β-cells. (A) 40 mM K^+ stimulation. (B) 20 mM glucose stimulation. Cells were stimulated for a short period as indicated by bars under the traces. Images were acquired at 1 s per image pair. Zn^{2+} signals were analyzed as direct intensities as indicated by the left Y-axis in each graph and $[Ca^{2+}]_i$ was expressed as F_0/F_1 indicated by the right Y-axis in each graph. The $[Ca^{2+}]_i$ traces in both graphs are in gray color.

Figure 5-3 illustrates an imaging experiment for simultaneous detection of $[Ca^{2+}]_i$ and Zn^{2+} release from cells stimulated by 15 mM glucose for longer period of time. For these experiments, glucose was spiked into the buffer at the time indicated to give a final concentration of 15 mM. The results illustrate cell-to-cell heterogeneity in secretion, as the top cell gave a strong secretion signal whereas the bottom cell had little secretion. This heterogeneity was common with clusters in that frequently only a few cells of the cluster were observed to give Zn^{2+} release. In contrast, the $[Ca^{2+}]_i$ responses in all cells had similar amplitudes (data not shown) in agreement with previous reports that $[Ca^{2+}]_i$ responses are well synchronized and relatively homogeneous in clusters (Gylfe et al., 1991; Jonkers et al., 1999).

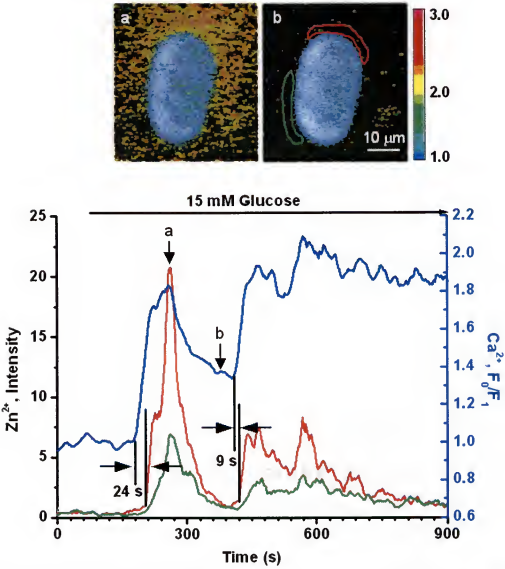

Figure 5-3. Biphasic Zn^{2+} secretion from a cell cluster stimulated by 15 mM glucose. Images shown are in dual-channel intensity ratios of FluoZin-3 fluorescence against Fura Red fluorescence. The time at which each image was acquired is indicated by an arrow above the traces. Image pairs of Ca^{2+} and Zn^{2+} were acquired at 1 Hz. Zn^{2+} signals were analyzed using ROIs shown on the right image and Ca^{2+} signals were analyzed using a ROI covering the entire cluster. Ca^{2+} and Zn^{2+} signals were plotted as in Figure 5-2. Zn^{2+} traces (red and green) correspond to the ROIs in the same colors. The time differences between the rise in $[Ca^{2+}]_i$ and secretion are indicated.

The temporal responses shown in Figure 5-3 illustrate that $[Ca^{2+}]_i$ and Zn^{2+} release were well correlated. As with the shorter stimulations, the delay between the initial rise in $[Ca^{2+}]_i$ and the initial rise in secretion was 13 ± 3 s (n = 11). The biphasic response shown in Figure 5-3 was observed for 5 out of 11 clusters with a transient first phase of release lasting 245 ± 40 s and a sustained second phase of release. Other clusters either displayed only a transient release or a sustained release phase. Frequently, the second phase of release gradually decreased to basal level after ~15 min even though the $[Ca^{2+}]_i$ was still fairly high, as shown in Figure 5-3. These different patterns are probably at least partially affected by the method of stimulation. Achieving a 15 mM glucose level requires adding a spike of glucose that has a higher concentration. Thus, the cells are likely exposed to higher concentrations of glucose as the spike is diluted. (This method of stimulation was used since all measurements were performed in a quiescent solution instead of a perfusion system. This approach avoids the expense associated with constantly perfusing the dye over the cells.)

Oscillations in Zn^{2+} Secretion from Cell Clusters

In some experiments, the cells were placed directly in buffer containing 15 mM glucose. For these cells, oscillations in $[Ca^{2+}]_i$ and Zn^{2+} release were typically observed (Figure 5-4). In the continuous presence of 15 mM glucose, correlated oscillations in $[Ca^{2+}]_i$ and secretion were observed for most clusters, although a minority of clusters (3 out of 17) did not respond to glucose in either $[Ca^{2+}]_i$ and secretion. Regular oscillations with an average period of 36 ± 10 s in $[Ca^{2+}]_i$ and secretion were observed from 50% of the clusters. Although the oscillations in $[Ca^{2+}]_i$ maintained a constant amplitude, the amplitude of oscillations in secretion were more variable. Oscillations in both $[Ca^{2+}]_i$ and secretion were abolished by the addition of 20 μM nifedipine, a Ca^{2+}-channel blocker (Figure 5-4A). The release of Zn^{2+} was well synchronized between different regions of a cluster as illustrated by the oscillations of release occurring simultaneously in 4 ROIs around the cluster (Figure 5-4A). The secretion observed from all ROIs correlates well to $[Ca^{2+}]_i$ as each increase in Zn^{2+} release corresponds to an elevation in $[Ca^{2+}]_i$ (see Figure 5-4B). Synchronous secretion between different regions and close correlation of $[Ca^{2+}]_i$ and secretion were observed in all clusters even regular oscillations did not occur. Interestingly, the latency between secretion and initial increase in $[Ca^{2+}]_i$ was much shorter at 2 ± 1 s during oscillations compared to the latency of 13 ± 3 s between the initial rise in $[Ca^{2+}]_i$ and secretion when increasing glucose from 3 to 15 mM.

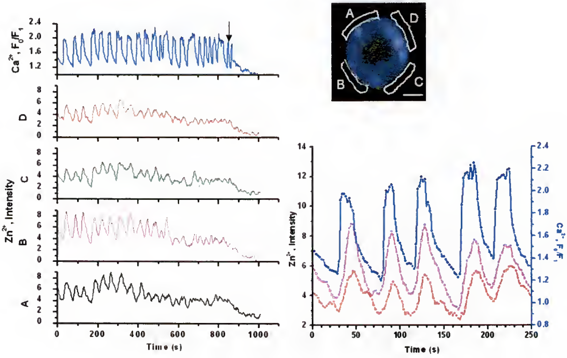

(A) (B)

Figure 5-4. Synchrony of Zn^{2+} secretion between different regions and synchrony between $[Ca^{2+}]_i$ and secretion from a cluster of ~15 cells. (A) Synchronous oscillations in secretion from four ROIs and $[Ca^{2+}]_i$. Image pairs of Ca^{2+} and Zn^{2+} were acquired at 0.5 Hz. Ca^{2+} signals (F_0/F_1) were analyzed by a ROI covering the entire cluster and Zn^{2+} signals in intensities were analyzed by four ROIs around the cluster as shown in the image. The arrow above the top trace indicates the addition of 20 μM nifedipine. (B) A detailed view of the relationship between $[Ca^{2+}]_i$ and Zn^{2+} secretion from two ROIs. The $[Ca^{2+}]_i$ trace is plotted in blue. The pink Zn^{2+} trace corresponds to region B and the red Zn^{2+} trace corresponds to region D.

Secretion of Zn^{2+} from Single Islets

Complex patterns of oscillations in secretion. The dynamics of Zn^{2+} secretion from single islets of Langerhans were investigated next using this imaging approach. Attempts to record secretion and $[Ca^{2+}]_i$ simultaneously in islets using confocal imaging were not successful apparently due to a combination of poor light penetration into the islets and weak fluorescence of Fura Red. When glucose was increased from 3 to 15 mM, biphasic Zn^{2+} secretion from islets was typically observed as shown in Figure 5-5A.

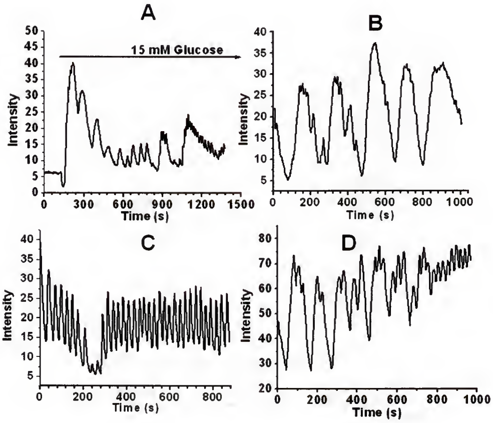

Figure 5-5. Oscillatory Zn^{2+} secretion from single islets of Langerhans. (A) Biphasic secretion from an islet when glucose was increased from 3 mM to 15 mM. (B) Slow oscillations. (C) Fast oscillations. (D) Fast oscillations superimposed on slow oscillations. For B, C, and D, islets were in the continuous presence of 15 mM glucose throughout the recording. All images were acquired at 0.5 Hz and signals in Zn^{2+} secretion were analyzed by drawing circular ROI with a width ~15 μm around the entire islet.

In the continuous presence of 15 mM glucose, regular oscillations in Zn^{2+} secretion were observed for 33 out of 47 islets. The oscillatory pattern varied with 22 islets displaying slow oscillations (average period of 154 ± 12 s, Figure 5-5B), 11 islets displaying fast oscillations (average period of 21 ± 3 s, Figure 5-5C), and 5 islets displaying a mixed pattern (Figure 5-5D). In three cases, slow oscillations developed into fast oscillations during the observation time. Islets without regular oscillations either showed sustained secretion or irregular oscillations in secretion.

Glucose-induced transient decrease in secretion. When Zn^{2+} secretion was monitored during the transition from 3 to 15 mM glucose, a transient decrease in Zn^{2+} level was frequently observed (12 of 15 islets) as shown in Figure 5-5A and 5-6. The basal fluorescence in islet imaging can be interpreted as the detection of a combination of the trace amount of Zn^{2+} in the buffer and basal secretion of Zn^{2+} from the islets. As shown, the addition of buffer had no obvious effect on basal fluorescence intensity, while the addition of glucose induced a transient decrease in basal fluorescence indicative of a decrease in Zn^{2+} release from the islets. The transient decrease in Zn^{2+} release was observed for 12 of 15 islets with an average period of decrease of 54 ± 10 s. A similar glucose-induced transient decrease in $[Ca^{2+}]_i$ for both islets and dispersed β-cells has been previously reported (Gylfe, 1988; Grapengiesser et al., 1988; Gilon and Henquin, 1992; Yada et al., 1992; Roe et al., 1994; Chow et al., 1995). This decrease in $[Ca^{2+}]_i$ has been shown to be inhibited by thapsigargin (Roe et al., 1994), a specific inhibitor of sarcoplasmic and endoplasmic reticulum Ca^{2+}-ATPases (SERCA), suggesting that the glucose-induced decrease in $[Ca^{2+}]_i$ is due to stimulation of SERCA activity. Our results show that the presence of 4 μM thapsigargin completely abolished the decrease in Zn^{2+}

secretion (Figure 5-6B, n = 6), leading to the conclusion that the transient decrease in secretion is due to a transient decrease in $[Ca^{2+}]_i$ induced by glucose. A similar glucose-induced decrease in insulin secretion was reported when insulin secretion measured in suspensions of β-cells (Lund et al., 1989; Nilsson et al., 1988). The results here confirm this observation and extend it to single islets and Zn^{2+} release.

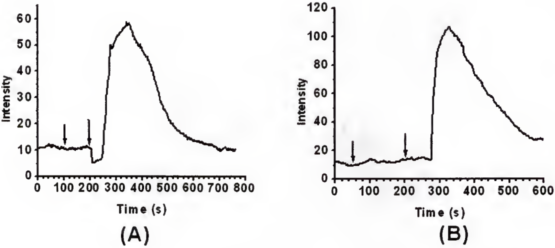

Figure 5-6. Transient decrease in basal Zn^{2+} secretion induced by 15 mM glucose. Images were acquired and analyzed as in Figure 5-5. Islets were initially incubated in KRB with 3 mM glucose. In both graphs, the 2nd arrow indicates the addition of glucose to increase the glucose concentration from 3 mM to 15 mM and the 1st arrow indicates the addition of the same amount of buffer. (A) An islet incubated in buffer without thapsigargin. (B) An islet incubated in buffer containing 4 μM thapsigargin.

Spatial synchrony and spatial heterogeneity of secretion. The spatial synchrony and heterogeneity of secretion were examined in single islets by analyzing Zn^{2+} release in different ROIs around the islets. As shown in Figure 5-7, spatial synchrony was high, similar to that observed in cell clusters, as release occurs simultaneously in all fours ROIs around the islet. Oscillations disappear immediately following the addition of nifedipine, a Ca^{2+}-channel blocker. Although diffusional mixing between regions may occur since

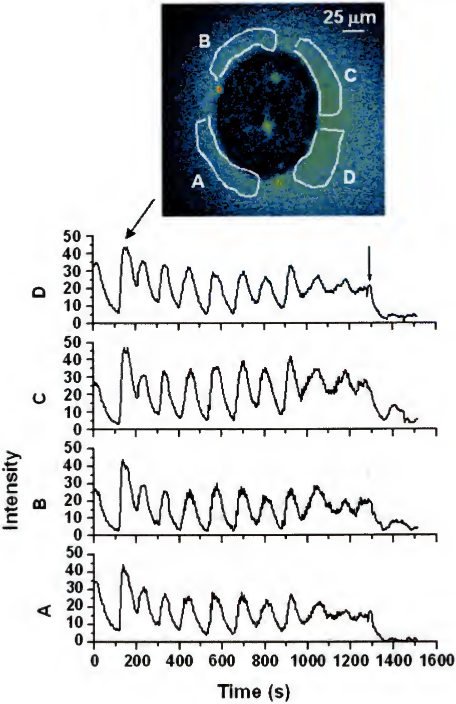

Figure 5-7. Spatially synchronized oscillations in Zn^{2+} secretion from a single islet. The islet was in the continuous presence of 15 mM glucose. All images were acquired at 0.5 Hz and the dynamics of Zn^{2+} secretion were analyzed using four ROIs surrounding the islet. The image shown is in raw intensity as in Figure 5-1B. The image shown was acquired when Zn^{2+} secretion was at a maximum, as indicated by the arrow. The addition of 40 μM nifedipine is indicated by the arrow above the top trace.

signals are measured in extracellular regions, the well-synchronized signals between regions far from each other (such as region A and C) without any time discrepancy are good evidence for spatially synchronized release of Zn^{2+} from islets. Although in this example only slow oscillations with a period of 100 s were observed, well-synchronized fast oscillations with a period of 10-30 s were also observed from single islets (data not shown). Spatially synchronized release of Zn^{2+} was observed for all islets with oscillations in secretion even when the oscillatory release from the islets was irregular.

Although the release was synchronized between different regions, the magnitude of release was frequently highly heterogeneous around islets. As shown in Figure 5-8, much larger signals of Zn^{2+} secretion were observed from the top of the islet than the bottom throughout the entire time course of oscillations. This spatial heterogeneity in Zn^{2+} secretion can also be noticed from the regions inside the islets. As shown in the images, the upper part within the islet has higher fluorescence intensities than the lower part within the islet; however, the secretion signals observed from both ROIs are well synchronized.

With the confocal imaging conditions used for these experiments, all fluorescence signals were collected from an optical section of ~2 μm thickness at the focal plane. The fluorescence signals observed inside the islet should correspond to the detection of released Zn^{2+} at interstitial spaces since the focal position for islet imaging was typically 20-40 μm above the bottom of islet. In order to verify whether the observed spatial heterogeneity of secretion in the two-dimensional optical section is representative of the secretion pattern from the whole islet, imaging through the whole islet was performed using Z-axis scanning. Figure 5-9 shows selected images of Zn^{2+} secretion from an islet at different focal positions. As shown, images at different focus planes have similar patterns of spatial heterogeneous secretion with the upper side secreted most. Spatially heterogeneous secretion was observed for 43 out of 47 islets with the active releasing region randomly at one side of the islet. The fluorescence intensities at the active regions were typically over 2-fold higher than those at relatively inactive regions. The spatially heterogeneous pattern for a given islet was maintained through the entire time course of oscillations.

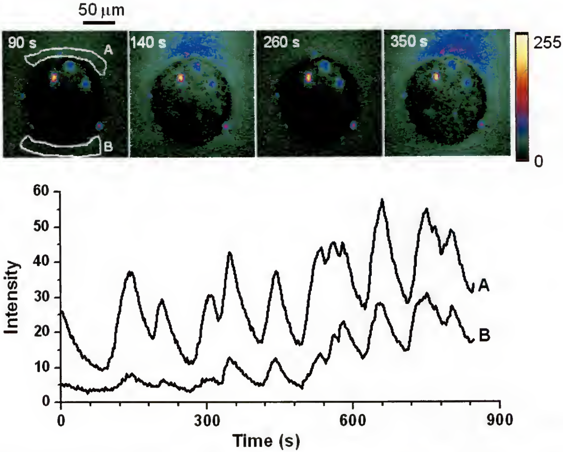

Figure 5-8. Spatial heterogeneity in Zn^{2+} secretion from a single islet. The islet was in the presence of 15 mM glucose. All images were acquired at 0.5 Hz and the images in the montage are shown in raw intensity as indicated by the scale bar. The time at which each image was acquired is indicated in seconds in each image. Temporal responses of Zn^{2+} secretion shown in the bottom plot were analyzed using the two ROIs as shown in the first image. The bright fluorescence spots inside the islet are cells with broken membranes and stained by FluoZin-3.

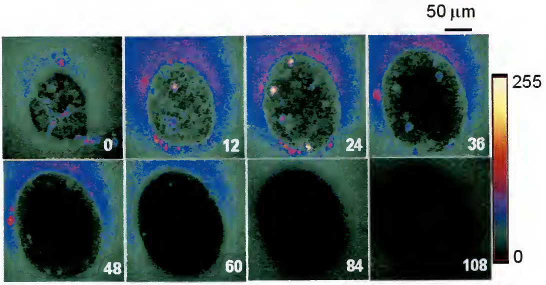

Figure 5-9. Images of Zn^{2+} secretion from an islet at various focal positions. Images were recorded with Z-axis scanning using 4 μm step size during sustained secretion. Images are shown in raw intensity. The brighter fluorescence on the top of the islet indicates more active release of Zn^{2+} from that region. The focal position of the 1st image is assigned as 0 μm and selected images as the focal positions moving up into the islet are shown in this montage. The number in each image indicates the focal position in microns as compared to 1st image.

Discussion

Using a novel imaging approach, we have characterized the temporal and spatial patterns of Zn^{2+} secretion from islet cell clusters and single islets in response to glucose and K^+. The data are consistent with the hypothesis that Zn^{2+} is co-released with insulin by exocytosis of secretory granules insofar as the released Zn^{2+} is well correlated to increases in $[Ca^{2+}]_i$ and follows patterns that have previously been observed for insulin secretion in perfusion systems with direct measurements of insulin by immunoassay. These data extend our knowledge of Zn^{2+} secretory patterns by demonstrating that its release is correlated with fast oscillations in $[Ca^{2+}]_i$. In addition, it has been demonstrated that Zn^{2+} release is synchronized around groups of cells, yet is heterogeneous with some cells much more active than others. It is expected that insulin secretion would follow similar patterns.

Coupling of $[Ca^{2+}]_i$ and Secretion

Simultaneous imaging of $[Ca^{2+}]_i$ and Zn^{2+} secretion demonstrated a good temporal correlation between $[Ca^{2+}]_i$ and secretion from cell clusters. The correlation includes the observation of well-synchronized oscillations in $[Ca^{2+}]_i$ and secretion from cell clusters (Figure 5-4) with the rise of $[Ca^{2+}]_i$ slightly preceding the rise in secretion. In addition, the complex patterns of oscillations in secretion from islets are similar to those previously reported for oscillations in $[Ca^{2+}]_i$ (Valdeolmillos et al., 1989; Bergsten et al., 1994). Taken together, these data support the view that oscillations in $[Ca^{2+}]_i$ drive secretory oscillations.

The observation that the $[Ca^{2+}]_i$ rise precedes the rise in secretion is not surprising because $[Ca^{2+}]_i$ is accepted as a proximal triggering signal for exocytosis (Ashcroft et al., 1994b). The latencies between the rise of $[Ca^{2+}]_i$ and secretion can be interpreted as the time required for $[Ca^{2+}]_i$ to reach the threshold necessary for triggering exocytosis. In supporting this hypothesis, the latencies observed are dependent on the modes of stimulation, thus the latency was ~3 s for K^+ stimulation and ~14 s for glucose stimulation. K^+ stimulation induces a continuous membrane depolarization leading to rapid Ca^{2+} influx, whereas glucose induces spikes of depolarization leading to a slower Ca^{2+} influx compared to K^+ so that it takes longer time to reach the threshold of $[Ca^{2+}]_i$. The latencies of K^+ stimulation agree with previous amperometric data (Smith et al., 1995), but are much longer than those when exocytosis was measured by the capacitance method (Ämmälä et al., 1993; Bokvist et al., 1995). In capacitance measurements, cells are stimulated by a voltage-clamp depolarization, usually to 0 mV, so a shorter latency than that induced by K^+ or glucose is expected due to the larger Ca^{2+} influx induced by such a large depolarization. It has also been observed that the latencies are dependent on the occurrence of a previous rise in $[Ca^{2+}]_i$. The average latency observed during oscillations in clusters is only ~2 s, which is much shorter compared to the latency of ~13 s between the initial rise of $[Ca^{2+}]_i$ and secretion in the first phase of secretion for glucose stimulation. During oscillations, the $[Ca^{2+}]_i$ is maintained at higher level than basal so that it takes a shorter time to reach the threshold when a Ca^{2+} influx is induced.

A glucose-induced transient decrease in basal Zn^{2+} secretion from single islets has also been observed prior to the stimulated increase. Similar decreases in $[Ca^{2+}]_i$ have been observed and attributed to ATP-induced activation of SERCA activity (Roe et al., 1994; Chow et al., 1995). Our results show that inhibition of SERCA with thapsigargin treatment also inhibits the observed decrease in Zn^{2+} secretion, suggesting a link between basal $[Ca^{2+}]_i$ and Zn^{2+} secretion. Since basal $[Ca^{2+}]_i$ appears to be too low to cause Ca^{2+}-dependent exocytosis, it is unclear how a decrease in basal $[Ca^{2+}]_i$ would decrease basal secretion. It is possible that, although the average basal $[Ca^{2+}]_i$ is low, microdomains of high $[Ca^{2+}]_i$ exist near the plasma membrane that trigger basal levels of exocytosis (Ämmälä et al., 1993; Bokvist et al., 1995; Qian et al., 2001; Chapter 3). Activation of SERCA would lower $[Ca^{2+}]_i$ in the cell and therefore increase the concentration gradient for Ca^{2+} that enters, allowing a rapid dissipation of the entering Ca^{2+} and reducing the probability of high $[Ca^{2+}]_i$ microdomains. Further investigations are required to confirm this hypothesis. In summary, all of these measurements are consistent with tight coupling of $[Ca^{2+}]_i$ and Zn^{2+} secretion and provide further evidence for the co-release of Zn^{2+} and insulin by exocytosis.

Spatial Synchrony and Spatial Heterogeneity of Secretion

Calcium imaging has previously revealed that oscillations in $[Ca^{2+}]_i$ are well synchronized and relatively homogeneous between all regions within clusters (Gylfe et al., 1991; Jonkers et al., 1999; Jonkers et al., 2001) and islets (Santos et al., 1991; Gilon and Henquin, 1992; Valdeolmillos et al., 1993; Gilon and Henquin, 1995). Our results demonstrate the Zn^{2+} secretion is also synchronized within an islet or islet cell clusters (Figures 5-4, 5-7, and 5-8). Thus, the coordination of cellular activity extends beyond Ca^{2+} entry into cells to secretory steps. These results support the view of an islet or cell cluster as a functional secretory syncytium (Santos et al., 1991; Valdeolmillos et al., 1993).

Although Zn^{2+} secretion occurs in synchrony around an islet or cell cluster, it tended to be heterogeneous in magnitude (Figures 5-3, 5-4, and 5-8). This may suggest some functional heterogeneity with regard to secretory activity among β-cells within an islet. The concept of functional heterogeneity of islet β-cells has been suggested previously, but remains controversial. A pronounced heterogeneous distribution of glucokinase among β-cells within the islet was revealed by immunohistochemical techniques (Jetton and Magnuson, 1992). Studies on isolated β-cells have showed different thresholds for glucose-induced insulin response (Schuit et al., 1988; Pipeleers et al., 1994). However, this result is inconsistent with previous work using ratiometric Ca^{2+} imaging that has revealed fairly homogeneous Ca^{2+} changes among cells in islets or clusters (Santos et al., 1991; Gylfe et al., 1991; Valdeolmillos et al., 1993; Jonkers et al., 1999). Imaging of NAD(P)H levels in islets with multi-photon microscopy has also revealed homogeneous metabolic responses within an intact islet (Bennett et al., 1996). Without direct measurements of secretion from individual β-cells within the islet, functional heterogeneity of β-cells cannot be ruled out. Although there may be some functional heterogeneity in β-cell secretion, other possible explanations should also be considered. Uneven distribution of non-β-cells and β-cells in the islet could lead to the heterogeneous secretion that was observed. It is also possible that cells contain variable amounts of Zn^{2+}, which would contribute to the heterogeneity of release. Further study is required in order to understand the basis and physiological significance of heterogeneous secretion among from different cells within islets and cell clusters.

Imaging of Zn^{2+} Release as a Technique for Monitoring Secretory Dynamics

In this work, Zn^{2+} release has been imaged; however, given the co-storage and co-release of Zn^{2+} and insulin, the results are likely reflective, at least qualitatively, of insulin secretory dynamics as well. Since a quantitative comparison of endogenous Zn^{2+} release and insulin release has yet to be made, it is unknown whether Zn^{2+} measurement could be used as a quantitative surrogate for insulin secretion. For example, differences of Zn^{2+} and insulin distribution among secretory granules could lead to some variation in the ratio of the amount of Zn^{2+} and insulin released over time.

The novel observations made with this approach demonstrate the utility of imaging techniques for studying secretion and intercellular communication. Such methods should be a useful complement to traditional biochemical approaches for monitoring secretory dynamics. Insulin secretion is typically monitored from a suspension of cells or islets with low temporal resolution and without spatial resolution

(Rosario et al., 1986; Bergsten and Hellman, 1993b). Although techniques with high temporal resolution, such as amperometry with microelectrodes and capacitance measurements, have been used for monitoring secretion from single cells (Ämmälä et al., 1993; Huang et al., 1995), it has been difficult to use these techniques for long term monitoring of secretion. In addition, these techniques do not allow multiple cells to be monitored simultaneously, which is possible with an imaging method. The combination of high temporal and spatial resolution of this method made it possible to resolve fast pulses of secretion (10-30 s period) from single islets and cell clusters, synchronous release from multiple cells, and heterogeneity of secretion among groups of cells. At present the method is limited by not providing the same level of quantitative information of insulin secretion as immunoassays. Another advantage of this method is the ease of coupling with a Ca^{2+} indicator such as Fura Red for simultaneous monitoring of $[Ca^{2+}]_i$ and secretion. In summary, the versatility of this technique in monitoring the dynamics of secretion from single β-cells, clusters and single islets with high sensitivity, temporal and spatial resolution will make it a valuable tool for physiological studies of secretion.

CHAPTER 6

ROLES OF INSULIN RECEPTOR SUBSTRATE-1, PHOSPHATIDYLINOSITOL 3-KINASE, AND RELEASE OF INTRACELLULAR Ca^{2+} STORES IN INSULIN-STIMULATED INSULIN SECRETION IN PANCREATIC B-CELLS

Introduction

Insulin secreted by pancreatic β-cells is the primary regulator of serum glucose concentrations in mammals. While substantial progress has been made in elucidating the mechanisms responsible for normal regulation of insulin secretion from the β-cell, many aspects of this process remain unclear. In particular, chemical and physiological interactions between cells within the islet exert an important level of control in the physiological regulation of insulin secretion, which is not entirely understood. Both hormonal and neuronal influences within islets may modulate β-cell activity and insulin secretion *in vitro* and *in vivo* (Schuit et al., 1989; Norman and Litwack, 1997; Moens et al., 1996). Although such influences have been demonstrated, the existence of significant autocrine effects of insulin on β-cells remained controversial for many years because a variety of studies yielded conflicting evidence on the modulation of insulin secretion by insulin in whole islets or *in vivo*. Recently, however, a variety of new methods have been utilized that demonstrate potent and possibly clinically important autocrine actions of insulin.

Several recent studies have indicated that β-cells express components of insulin signaling systems including insulin receptors (Verspohl and Ammon, 1980; Gazzano et al., 1985; Rothenberg et al., 1995), insulin receptor substrates (IRS-1 and IRS-2)

(Harbeck et al., 1996; Velloso et al., 1995; Sun et al., 1997a), phosphatidylinositol 3-kinase (PI3-K) (Alter and Wolf, 1995; Gao et al., 1996), and protein kinase B (PKB) (Holst et al., 1998). Evidence has also been obtained indicating that insulin released by glucose can activate these components in addition to other proteins in the cells. Insulin binds to receptors on the surface of β-cells (Verspohl and Ammon, 1980; Patel et al., 1982) and activates tyrosine phosphorylation of insulin receptors (Rothenberg et al., 1995), insulin receptor substrates (Velloso et al., 1995), and PHAS-I (Xu et al., 1998a). Furthermore, maximum glucose-stimulated production of phosphatidylinositol 3,4,5-triphosphate (PIP_3), a major product of PI3-K activity, coincides with the early peak phase insulin secretion in islets and clonal β-cells (Alter and Wolf, 1995). Thus, autocrine activation of the β-cell insulin receptors and several downstream proteins has been demonstrated.

Some of the physiological consequences of insulin receptor activation at β-cells have recently been revealed. Activation of the insulin signaling pathway in β-cells leads to initiation of insulin synthesis at both transcriptional and translational levels, increasing the cellular content of releasable hormone in primary and clonal β-cell cultures (Xu et al., 1998a; Xu and Rothenberg, 1998b; Leibiger et al., 1998). In βTC6-F7 cells transfected to overexpress the insulin receptor, basal and glucose-stimulated insulin secretion was enhanced compared to kinase negative controls (Xu and Rothenberg, 1998b). In another report, clonal cells lacking the IRS-1 protein showed both decreased insulin content and glucose-stimulated secretion (Kulkarni et al., 1998). These latter studies suggest that insulin can exert positive control over synthesis and/or secretion. Direct evidence for the effects of insulin on insulin secretion has been obtained by application of exogenous insulin to isolated β-cells and detecting secretion by amperometry with microelectrodes (Aspinwall et al., 1999a). These data illustrate that insulin evokes insulin secretion mediated by the insulin receptor and that such positive feedback occurs during glucose stimulation. This report also showed that insulin could evoke an increase in intracellular free Ca^{2+} concentration ($[Ca^{2+}]_i$). A recent study with clonal β-cells demonstrated that overexpression of IRS-1 and insulin receptor elevated $[Ca^{2+}]_i$ levels and enhanced fractional insulin secretion (Xu et al., 1999), in good agreement with the studies on application of exogenous insulin. More recently, a similar stimulatory effect was observed for an insulin mimetic drug L-783, 281 on insulin secretion from isolated β-cells (Roper et al., 2002).

The potential *in vivo* significance of positive autocrine feedback on insulin secretion and synthesis was revealed in experiments in which the gene for the β-cell insulin receptor was inactivated by use of the Cre-loxP system (Kulkarni et al., 1999b). Mice lacking the β-cell insulin receptor had lowered insulin response to glucose and impaired glucose tolerance, suggesting an important role for autocrine signaling in insulin secretion and glucose homeostasis *in vivo*. Further evidence for the importance of autocrine action was obtained when a polymorphism in IRS-1 in humans was associated with impaired insulin secretion and pathology of some forms of type 2 diabetes (Porzio et al., 1999). The identical polymorphism expressed in clonal β-cells reduced glucose and sulfonylurea-stimulated insulin secretion.

The evidence so far has established that insulin activates the insulin receptor and that this effect results in enhanced insulin synthesis and insulin secretion. Derangement in this process leads to impaired insulin secretion similar to that seen in type 2 diabetes.

Such results suggest a potential link between the symptoms of insulin resistance and impaired insulin secretion found in type 2 diabetes. Given the potential significance of autocrine activation of insulin secretion and $[Ca^{2+}]_i$ changes, some of the important elements that couple an insulin stimulus to insulin secretion and $[Ca^{2+}]_i$ changes were investigated and the source and temporal characteristics of the $[Ca^{2+}]_i$ changes were further characterized in this work. The correlation of insulin-stimulated $[Ca^{2+}]_i$ responses and secretion was also investigated by simultaneous measurements of Zn^{2+} secretion and $[Ca^{2+}]_i$ changes using a recently developed fluorescence imaging approach (Chapter 4 and 5).

Experimental

Chemicals

Type XI collagenase, HEPES, thapsigargin, wortmannin, nifedipine, U73122, U73343, bisindolylmaleimide I, and bovine insulin were obtained from Sigma and used without further purification. Fluo-4 AM, Fura Red AM, and FluoZin-3 were from Molecular Probes. Unless otherwise stated, all chemicals for islet and cell culture were obtained from Life Technologies. All other chemicals were from Fisher unless noted and were of highest purity available.

Isolation and *In Vitro* Culture of Mouse β-Cells

Pancreatic islets were isolated from 20-35 g CD-1 mice as described in Chapter 2. Briefly, islets were isolated by ductal injection with collagenase type XI and dispersed into single cells by shaking in dilute (0.025%) trypsin/EDTA for 6 min at 37° C. Cells were cultured on 35 mm tissue culture dishes (Nunclon) or 25 mm glass coverslips at 37° C, 5% CO_2, pH 7.4, in RPMI 1640 containing 10% fetal bovine serum (FBS), 100

U/mL penicillin and 100 μg/mL streptomycin and used on days 1 to 2 following isolation.

Culture of IRS-1 (+/-) and IRS-1 (-/-) Cells

Cell lines expressing the IRS-1 protein and IRS-1 specific knockouts were derived from breeding wild-type and IRS-1 (-/-) mice with mice expressing the SV40 T antigen (RIP-Tag) on a β-cell specific promoter similar to the procedure used by Efrat et al. (1988) to derive βTC3 cells. Tumors from 12 to 14 week old RIP-Tag/IRS-1(+/-) and RIP-Tag/IRS-1(-/-) mice were manually dissected and placed in Dulbecco's Modified Eagle's Media (DMEM) supplemented with fetal calf serum, penicillin and streptomycin. The tumor capsule was disrupted, and the cells were gently dispersed with forceps. Tumor cells were purified by gravity sedimentation and seeded in a 48-well plate containing DMEM. IRS-1 (+/-) and IRS(-/-) clonal cells were grown to approximately 80% confluence and split 1:3 in DMEM supplemented with 20% FBS. βTC3 cells were cultured in 200 mL tissue culture flasks in DMEM containing 25 mM d-glucose, 10% fetal bovine serum, 100 U/mL penicillin and 100 μg/mL streptomycin at 37° C, 5 % CO_2. Cells were passaged with 0.05% trypsin/EDTA at 70% confluence and plated onto 35 mm tissue culture plates (Nunclon) for single cell experiments. Cells were used on days 2-4 following passage.

Amperometric Detection of Exocytosis

Microelectrodes were constructed of carbon fibers sealed in glass micropipettes as described in Chapter 2 and elsewhere (Huang et al., 1995; Aspinwall et al., 1997). Prior to use, electrodes were polished to a 45° angle and cleaned. Amperometric measurements were made by positioning microelectrodes ~1 μm from a cell and applying stimulant from a micropipette ~30 μm from the cell as described elsewhere (Chapter 2; Aspinwall et al., 1997). All experiments were performed with cells at 37° C incubated in pH 7.4 Kreb's Ringer buffer (KRB) containing 118 mM NaCl, 5.4 mM KCl, 2.4 mM $CaCl_2$, 1.2 mM $MgSO_4$, 1.2 mM KH_2PO_4, 3 mM *d*-glucose and 20 mM HEPES. Stimulant solutions (100 nM insulin, 17 mM glucose, or 200 μM tolbutamide) were prepared by diluting appropriate stock solutions into KRB.

Amperometry was performed using a battery to apply potential to a SSCE reference electrode. For measurements of 5-HT secretion, dispersed β-cells were incubated in tissue culture media containing 0.5 mM 5-HTP 16 h at 37° C, 5% CO_2, pH 7.4. Cells were used for secretion experiments immediately after loading. For detection of 5-HT the potential at the working electrode was 0.65 V vs. SSCE. Data were low pass filtered at 100 Hz and collected at 500 Hz using a personal computer (Gateway 2000 P5-166) via a data acquisition board (Axon Instruments, DigiData 1200B). For amperometric data analysis, current spikes were used only if the signal-to-noise ratio (S/N) was >10.

Confocal Imaging of $[Ca^{2+}]_i$ and Zn^{2+} Secretion

All imaging experiments were performed on a Nikon RCM 8000 laser scanning confocal microscope (See Appendix A for detail of the system). A Nikon 40x, 1.15 NA, UV-corrected water-immersion objective was used for all imaging. Cells to be imaged were bathed in KRB and maintained at 37 °C on the stage of the microscope by a microincubator (Medical Systems, Inc.).

The calcium indicator fluo-4 was used for imaging of $[Ca^{2+}]_i$. Prior to $[Ca^{2+}]_i$ imaging experiments, 25 mm coverslips containing adherent cells were loaded with 1 μM fluo-4 AM in KRB for 30 min at 37 °C. Dye solution was then replaced with KRB, and coverslips with adherent cells were placed into a 35 mm coverslip holder for immediate use. Images were acquired with a 525 ± 10 nm band-pass filter using the 488 nm excitation line of the laser. Imaging of Zn^{2+} secretion was performed as described in the Experimental section in Chapter 4. Briefly, cells are bathed in KRB containing 2 μM FluoZin-3 and images were acquired with 488 nm excitation and 525 ± 10 nm band-pass emission filter.

Simultaneous measurements of Zn^{2+} Secretion and $[Ca^{2+}]_i$ were achieved using the combination of FluoZin-3 and Fura Red, a long emission Ca^{2+} indicator as described in Chapter 5. Briefly, cells were loaded with 3 μM Fura Red AM for 40 min in RPMI 1640medium at 37 °C. After loading, cells were washed with KRB twice and incubated in KRB containing 2 μM FluoZin-3. Dual channel images were acquired with 488 nm excitation and collected at two separated channels using a 550 nm cut-off dichroic mirror and a 525 ± 10 nm bandpass filter for FluoZin-3 detection and a 595 nm long-pass filter for Fura Red detection.

All images were stored on an optical disc cartridge (TQ-FH332, Panasonic) by an optical disc recorder (TQ-3038F, Panasonic) for later analysis.

Image and Data Analysis

Images were played back from the optical disk cartridge, captured and analyzed using Simca image analysis software (C-IMAGING Systems) in combination with an 8-bit frame grabber. Regions of interest (ROI) were drawn by free hand and applied to a series of images. The average intensity of the ROI was measured as a function of time. ROIs used for fluo-4 or Fura Red signal analysis were drawn covering the cells, while ROIs were drawn outside the cells for FluoZin-3 signal analysis. Because both fluo-4 and Fura Red are single-wavelength dyes, their emission is a function of both $[Ca^{2+}]_i$ and dye concentration. $[Ca^{2+}]_i$ changes were therefore expressed as F_1/F_0 ratios for fluo-4 and F_0/F_1 ratios for Fura Red, where F_0 was the fluorescence intensity of the initial image during the recording (Guerineau et al., 1998). The use of different ratios for fluo-4 and Fura Red in data analysis is because fluo-4 fluorescence increases as $[Ca^{2+}]_i$ increases while Fura Red fluorescence decreases as $[Ca^{2+}]_i$ increases. The amount of insulin secretion measured by amperometry was analyzed as spikes per stimulation. All means are reported as ± standard error of the mean (SEM). Statistical differences between means were evaluated using a two-tailed Student's *t*-test.

Thapsigargin, Wortmannin, Nifedipine, U73122 and Bisindolylmaleimide I Treatments

For amperometric experiments, mouse β-cells were stimulated with 100 nM insulin and exocytosis of 5-HT detected by amperometry to establish viability. Following successful repetitive stimulation with insulin, 100 nM wortmannin, 1 μM thapsigargin, 20 μM nifedipine, 10 μM U73122, or 2 μM bisindolylmaleimide I was added to the buffer and allowed to incubate for 5 to 10 minutes. The same cell was then stimulated again with insulin in the presence of the chemical added.

For the $[Ca^{2+}]_i$ imaging experiments, cells were stimulated by 100 μM tolbutamide for 5 s to establish viability. Cells that responded to tolbutamide were then stimulated with 100 nM insulin and temporal changes of $[Ca^{2+}]_i$ were monitored by fluo-4 fluorescence. Treatment with inhibitors was similar as in amperometric measurements. Before insulin stimulation, a control KRB stimulation was applied to the cell to ensure Ca^{2+}changes and insulin secretion were not due to artifacts associated with the buffer application.

Results

Insulin-stimulated Ca^{2+} Release from Intracellular Stores

It had been previously reported that application of insulin to dispersed β-cells evoked a rise in $[Ca^{2+}]_i$ (Aspinwall et al., 1999a). Our initial experiments were to further characterize this change in $[Ca^{2+}]_i$ at single cells. As shown in Figure 6-1, application of 100 nM insulin, but not buffer solution, results in increased $[Ca^{2+}]_i$ as monitored by fluo-4 fluorescence. Figure 6-1C illustrates further analysis of the images shown in Figure 6-1 (A and B) as a plot of relative fluorescence intensity (F_1/F_0) within the cell as a function of time. Insulin induced increases in $[Ca^{2+}]_i$ were observed in 37 of 85 cells tested. All cells that were included in this sampling had first responded with a $[Ca^{2+}]_i$ rise after tolbutamide stimulation. The cells that responded to insulin displayed a variety of temporal patterns of $[Ca^{2+}]_i$ changes (Figure 6-2). Of the 37 cells that responded to insulin, 9 (24%) exhibited biphasic or oscillatory response similar to that in Figure 6-1C or 6-2D, 9 cells (24%) showed a transient peak response (Figure 6-2A), 14 cells (38%) generated an elevated plateau of $[Ca^{2+}]_i$ which lasted more than one minute after stimulation (see Figure 6-2B), and 5 cells (14%) had a slow increase of $[Ca^{2+}]_i$ that did not peak or plateau after 2 min (see Figure 6-2C). The maximum $[Ca^{2+}]_i$ increase induced by insulin was significantly smaller than that typically induced by a depolarizing stimuli, 200 μM tolbutamide (see Figure 6-2, D and E), and occurred with a much slower onset than that observed with tolbutamide. The latency of responses to insulin was 12 ± 10 s, whereas that for tolbutamide was 1.5 ± 1 s. The heterogeneity of temporal pattern is similar to that reported previously for single cell studies of $[Ca^{2+}]_i$ changes induced by glucose in β-cells (Theler et al., 1992).

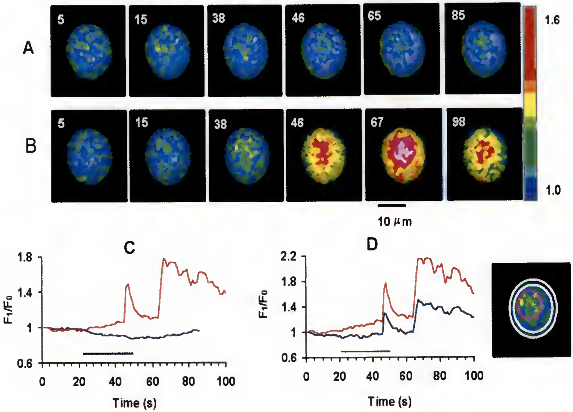

Figure 6-1. $[Ca^{2+}]_i$ changes in response to insulin stimulation. Confocal images were collected at the rate of 1.07 s per image using the fluorescent Ca^{2+} indicator, fluo-4 and shown in intensity ratios against the initial image in the series as described in text. Image series are A) control stimulation with KRB, and B) stimulation with 100 nM insulin for the same cell. Stimulant was applied from 22 to 52 s. The ratio values are indicated by colors as on the scale bar. The number embedded in each image indicates the time in seconds that the image was collected. Note intracellular intensity increase at 38 s and the much greater intensity increase in the cell interior in (B). C) Time course of changes in $[Ca^{2+}]_i$ in response to insulin stimulation (red line) and control (blue line) for the cell above. Relative fluorescence intensity (F_1/F_0) was obtained by drawing a ROI around the entire cell and applying the ROI to the entire series. The bar underneath traces indicates the period of application of 100 nM insulin. (D) Comparison of the responses in $[Ca^{2+}]_i$ in the interior region (red line) and the edge of the cell (blue line). The ROIs are indicated in the image, where the region inside the red circle is used as the interior region and the region between the concentric white circles is used as the edge region.

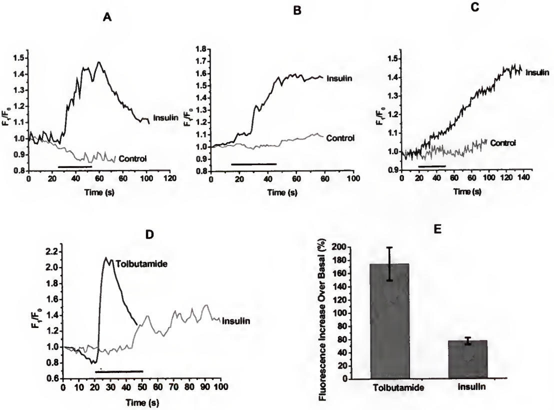

Figure 6-2. Different patterns for the time course of $[Ca^{2+}]_i$ response to insulin stimulation as monitored by fluo-4 fluorescence. Images were acquired and analyzed as in Figure 6-1. (A) Example of a cell with transient peak response due to insulin stimulation. (B) Example of a cell with plateau of $[Ca^{2+}]_i$ increase in response to insulin. (C) Example of cell with a slow increase in $[Ca^{2+}]_i$ after insulin stimulation. (D) Comparison of responses induced by insulin and tolbutamide from a cell that exhibited an oscillatory response to insulin. (E) Comparison of maximal increase caused by application of 200 µM tolbutamide for 5 s compared to application of 100 nM insulin at same cells. Bars in A-D indicate the application of stimulant to the cell. Solid bar is for application of 100 nM insulin and dashed bar is for 200 µM tolbutamide. Control in A, B, and C is application of KRB to the cell for the same time as the insulin. Five minutes was allowed between stimulations at a cell.

The relatively low success rate for insulin stimulation compared with tolbutamide stimulation is apparently due to cellular heterogeneity and the difficulty of detecting insulin induced signals. Cells that did not respond to insulin (n = 48) only gave a 72 ± 11% increase in $[Ca^{2+}]_i$ with tolbutamide stimulation, whereas cells that did have a positive response to insulin (n = 37) averaged a 215 ± 38% increase in $[Ca^{2+}]_i$ with tolbutamide stimulation. Thus, the non-responding cells also had a statistically significant ($p < 0.001$) lower Ca^{2+} response to tolbutamide. Furthermore, the magnitude of the peak Ca^{2+} response for insulin stimulation is small, averaging < 30% that of the tolbutamide (Figure 6-2E). This small signal means that the insulin induced responses are more difficult to detect than tolbutamide induced responses. Thus, some of the cells that were counted as not responding may simply have had small responses that were not detectable. This conclusion is supported by the fact that the non-responding cells consistently yielded lower $[Ca^{2+}]_i$ responses to tolbutamide.

In 18 (~50%) of the cells that responded to insulin, the $[Ca^{2+}]_i$ increase appeared initially in the interior of the cell rather than at the edge of the cell (Figure 6-1B). In the remaining cells, the $[Ca^{2+}]_i$ increase was observed simultaneously all across the cell, suggesting that the temporal resolution of the measurement was too low to locate the initiation of $[Ca^{2+}]_i$ because of rapid diffusion of the Ca^{2+} ions in the cytoplasm. A plot of the relative intensities (F_1/F_0) for the cell interior and the cytoplasm near the cell membrane is compared in Figure 6-1D, which shows a higher $[Ca^{2+}]_i$ increase in the interior region. The observation of larger $[Ca^{2+}]_i$ increase in the cell interior is in contrast to Ca^{2+} imaging performed with depolarizing stimuli, such as glucose, which display higher $[Ca^{2+}]_i$ increases at the edge of the cell because of Ca^{2+} entry through L-type Ca^{2+} channels (Chapter 3; Theler et al., 1992; Qian et al., 2001). The apparent localization of the Ca^{2+} changes observed following application of insulin suggests that the increase in $[Ca^{2+}]_i$ is a result of mobilization from intracellular Ca^{2+} stores. This conclusion was further supported by the observation that the magnitude of $[Ca^{2+}]_i$ changes were

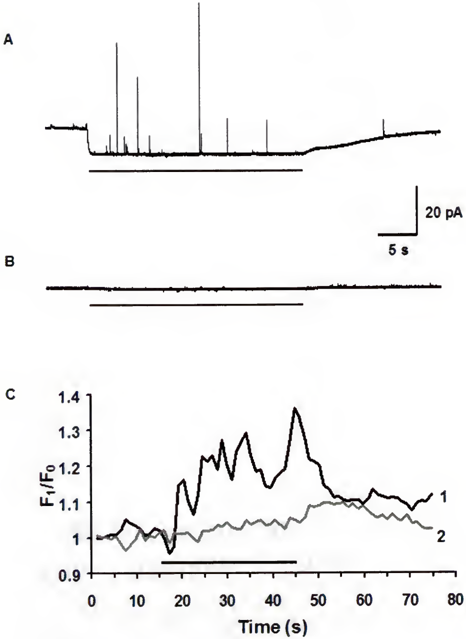

Figure 6-3. Effects of thapsigargin on insulin-stimulated insulin secretion and $[Ca^{2+}]_i$ changes. (A) Amperometric detection of 5-HT exocytosis from single β-cell upon stimulation with 100 nM insulin in the absence of thapsigargin. (B) Amperometric detection of 5-HT exocytosis from same cell as in (A) after 5 min incubation with 1 μM thapsigargin. (C) Typical insulin induced $[Ca^{2+}]_i$ traces of a cell in the absence of thapsigargin (1) and a cell that had been incubated with 1 μM thapsigargin for 5 min (2) before stimulation. Bars under traces indicate application of stimulant. Fluorescent data were collected and plotted as in Figures 6-1 and 6-2.

unaffected by removing extracellular Ca^{2+} from the imaging buffer or by including 20 μM nifedipine, a blocker of $_L$-type voltage-gated Ca^{2+} channels, in the buffer (see Figure 6-4B). In addition, cells treated with 1 μM thapsigargin, a potent inhibitor of the SERCA pump that depletes endoplasmic reticulum (ER) stores of Ca^{2+}, had significantly lower insulin-induced $[Ca^{2+}]_i$ changes (see Figure 6-3C and 6-4B) than control cells. These data suggest that the increase in $[Ca^{2+}]_i$ evoked by insulin is a result of Ca^{2+} release from intracellular stores, especially the ER.

Requirement of Intracellular Ca^{2+} Mobilization for Insulin-stimulated Exocytosis

After observing intracellular Ca^{2+} mobilization following insulin stimulation, the possible requirement of Ca^{2+} mobilization on insulin-stimulated exocytosis was investigated. Exocytosis was monitored by amperometrically detecting release of 5-HT that had been allowed to accumulate in the secretory granules of the β-cells. The 5-HT method was used instead of direct detection of insulin at a modified electrode (Huang et al., 1995) because of the relative simplicity of this approach, especially for autocrine studies. The validity of the 5-HT method has been established by previous studies that demonstrated: 1) detection of exocytosis with a variety of insulin secretagogues (Aspinwall et al., 1997; Smith et al., 1995; Zhou and Misler, 1996); 2) that insulin and 5-HT are released exclusively from the same vesicles (Aspinwall et al., 1999b); and 3) that direct detection of insulin and detection of 5-HT give comparable results for insulin stimulation (Aspinwall et al., 1999a). As seen in Figure 6-3A, application of 100 nM insulin to a single β-cell results in detection of a series of current spikes at the microelectrode indicative of exocytosis and subsequent detection of packets of 5-HT diffusing to the electrode. Incubation of cells with 1 μM thapsigargin completely abolished insulin-induced exocytosis in all cells tested (n = 4, Figures 6-3B and 6-4A). In addition, insulin-stimulated insulin secretion, measured as number of exocytosis events detected per stimulation per cell, was not significantly affected by removal of extracellular Ca^{2+} or by treatment with 20 μM nifedipine (Figure 6-4A). The results from the thapsigargin treatment suggest an important role for Ca^{2+} released from the ER in evoking secretion. In addition, the Ca^{2+}-free and nifedipine results indicate a minor, if any, role for extracellular Ca^{2+} entering the cell in insulin activation of exocytosis.

Involvement of IRS-1 in Insulin-Stimulated Exocytosis and Increases in $[Ca^{2+}]_i$

It has been previously demonstrated that insulin-stimulated insulin secretion in β-cells is mediated by β-cell insulin receptors (Aspinwall et al., 1999a). Insulin receptor substrates are intimately coupled to the insulin receptor and hence the insulin signaling pathway (White, 1997). To investigate the potential involvement of IRS-1 in autocrine activation of β-cell secretion, insulin-stimulated insulin secretion and $[Ca^{2+}]_i$ changes in wild-type βTC3 cells (IRS-1 +/-) and IRS-1 knockout cells (IRS-1 -/-) have been measured as illustrated in Figure 6-5. It has been observed that much like primary β-cells, wild-type cells exhibited insulin-induced exocytosis and $[Ca^{2+}]_i$ changes. Wild-type cells stimulated with 100 nM insulin evoked detectable exocytosis in 16 of 33 cells attempted. In the IRS-1 knock-out cells, no secretory activity was detected upon application of 100 nM insulin (25 of 25 cells) (Figure 6-5C), even though these same cells exhibited secretion from tolbutamide stimulation (Figure 6-5C). Insulin-induced increases in $[Ca^{2+}]_i$ were observed in 7 of 16 wild-type cells. The various patterns of $[Ca^{2+}]_i$ increase seen with primary β-cells were also seen with the wild-type cells. No increase in $[Ca^{2+}]_i$ was observed for IRS-1 knockout cells (13 of 13 cells) following

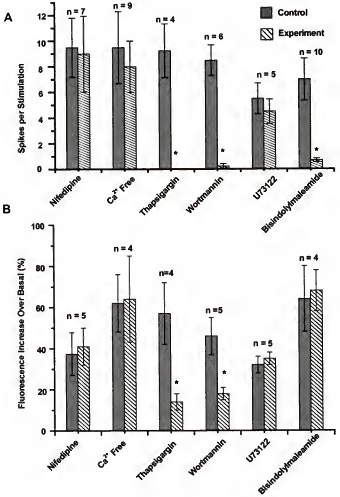

Figure 6-4. Summary of the effect of experimental manipulations on insulin stimulated exocytosis (A) and $[Ca^{2+}]_i$ increases (B). (A) For insulin-stimulated exocytosis, secretion was quantified as the number of exocytotic events detected. "Control" bars represent average number of spikes detected before addition of drugs. "Experiment" bars represent average number of spikes detected after addition of drugs. Statistically significant difference between control and experimental bars is indicated by *. Number of cells used for each experiment is indicated over the bars. (B) $[Ca^{2+}]_i$ increases were plotted as the maximal percent increase over the basal level. The number of cells for each condition is given over the bars. Only cells with an increase in $[Ca^{2+}]_i$ were used in averaging. All controls are measurements in the absence of drugs except the control for U 73122 is in the presence of U73343, a structural analog of U73122. Statistically significant difference between the control and the experimental bars is indicated by *. In all cases, 100 nM insulin was applied for 30 s. The following concentrations of inhibitors were used: 20 μM nifedipine, 1 μM thapsigargin, 100 nM wortmannin, 10 μM U73122, 10 μM U73343 and 2 μM bisindolylmaleamide I. Statistical significance of differences from control: $* = P < 0.01$.

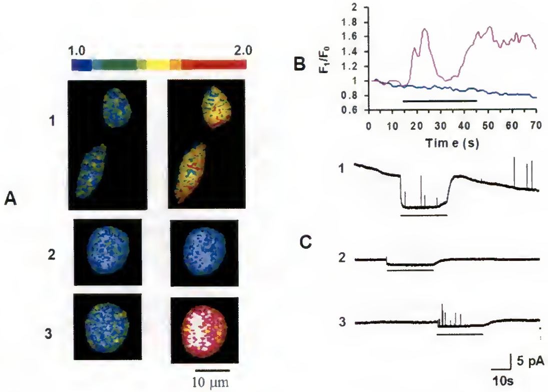

Figure 6-5. Effect of IRS-1 on insulin-stimulated insulin secretion and $[Ca^{2+}]_i$ changes in βTC3 cells. (A) $[Ca^{2+}]_i$ images before and after stimulation. 1) βTC3 IRS-$1^{+/-}$ (control) cell stimulated with 100 nM insulin, 2) IRS-$1^{-/-}$ cell stimulated with 100 nM insulin, and 3) the same IRS-$1^{-/-}$ cell stimulated with 200 µM tolbutamide. (B) Typical $[Ca^{2+}]_i$ traces of a βTC3 wild-type cell (red line) and IRS-1 knockout cell (blue line). The bar underneath traces indicates the application of 100 nM insulin. (C) Detection of insulin-stimulated exocytosis in IRS-$1^{+/-}$ (control) and IRS-$1^{-/-}$ βTC3 cells. Detection of accumulated 5-HT secretion from: 1) βTC3 IRS-$1^{+/-}$ cell stimulated with 100 nM insulin, 2) IRS-$1^{-/-}$ cell stimulated with 100 nM insulin, and 3) IRS-$1^{-/-}$ cell stimulated with 200 µM tolbutamide. Data in 2) and 3) are from same cell. Bars under current traces indicate application of stimulant. Ca^{2+} images were acquired and analyzed as in Figure 6-1.

insulin stimulation, but all the cells used for insulin stimulation showed a $[Ca^{2+}]_i$ increase following 200 µM tolbutamide stimulation (Figure 6-5A). To summarize, in wild-type βTC3 cells, insulin evoked exocytosis and $[Ca^{2+}]_i$ changes with a similar frequency and magnitude to that observed in primary cells; however, in the IRS-1 knockout βTC3 cells, insulin did not evoke either $[Ca^{2+}]_i$ changes or exocytosis. These results illustrate a critical role for IRS-1 in mediating the autocrine $[Ca^{2+}]_i$ changes and insulin secretion.

Wortmannin Sensitivity of Insulin-stimulated Exocytosis and $[Ca^{2+}]_i$ Response

After observing IRS-1 involvement in insulin stimulation of exocytosis in the β-cell, the role of PI3-K in insulin-stimulated secretion and $[Ca^{2+}]_i$ changes in primary β-cells was investigated. Following repetitive stimulation with 100 nM insulin to ensure that a cell responded to insulin, β-cells were incubated with 100 nM wortmannin, a potent inhibitor of PI3-K, for 5 min. As shown in Figure 6-4A, wortmannin completely abolished exocytosis from the β-cells, suggesting the requirement of PI3-K activation in the insulin-stimulated insulin secretion pathway. The requirement of PI3-K activation was also investigated for insulin stimulated $[Ca^{2+}]_i$ changes. In the presence of 100 nM wortmannin, the insulin-induced Ca^{2+}-response was significantly reduced (Figure 6-4B).

Roles of Phospholipase C (PLC) and PKC in Insulin-stimulated Insulin Secretion

The activation of PI3-K leads to production of PIP_3, which could activate PLC-γ (Bae et al., 1998; Falasca et al., 1998) and lead to release of Ca^{2+} from inositol 1,4,5-trisphosphate (IP_3)-sensitive Ca^{2+} stores. The effect of PLC activation on insulin-stimulated insulin secretion was investigated by using the PLC inhibitor U73122. As shown in Figure 6-4A, in the presence of the inhibitor, secretion was reduced to 82% of control, however, the difference was not statistically significant. In the calcium measurements, U73343, a structural analog of U73122, was used as a control. U73343 does not inhibit PLC. No difference between the effect of U73122 and U73343 control was observed (Figure 6-4B). In a positive control, treatment with U73122 completely abolished the secretory and Ca^{2+} response evoked by carbachol stimulation, which is known to release Ca^{2+} through the PLC-IP_3 pathway. These data suggest that PLC is not involved in the insulin-stimulated exocytosis signaling pathways.

Next, the effects of PKC inhibition on insulin-stimulated insulin secretion and $[Ca^{2+}]_i$ changes were investigated. As shown in Figure 6-4, treatment of cells with the PKC inhibitor bisindolylmaleimide I completely abolished the insulin-stimulated insulin secretion, but had an insignificant effect on $[Ca^{2+}]_i$ changes evoked by insulin. These data indicate that activation of PKC is not required for Ca^{2+} mobilization, but is strongly involved in the secretory effect induced by insulin.

Correlation of Insulin-stimulated $[Ca^{2+}]_i$ Responses and Secretion

The data shown above suggest critical roles of $[Ca^{2+}]_i$ in insulin-stimulated secretion because any treatments (IRS-1 knockout, PI3-K inhibition, thapsigargin treatment) that eliminate increases in $[Ca^{2+}]_i$ also eliminate secretion. In order to better correlate insulin-stimulated $[Ca^{2+}]_i$ responses and secretion, simultaneous measurements of $[Ca^{2+}]_i$ and secretion from isolated β-cells have been attempted. In these measurements, a recently developed fluorescence imaging approach was used for monitoring secretion from β-cells because the difficulty in coupling amperometry to $[Ca^{2+}]_i$ imaging. In the method, Zn^{2+} release from β-cells is measured as a marker of insulin secretion because β-cell secretory granules co-store Zn^{2+} and insulin and subsequently co-release these species during exocytosis (Emdin et al., 1980; Formby et al., 1984; Gold and Grodsky, 1984; Foster et al., 1993; Qian et al., 2000). The detail of this approach has been described in Chapter 4 and Chapter 5. Briefly, cells are incubated in buffer containing a membrane impermeant, fluorogenic Zn^{2+} specific indicator FluoZin-3. When Zn^{2+} is released into the extracellular space, it reacts with FluoZin-3 to form a fluorescent complex, which is detected by confocal fluorescence microscopy. Using this approach, fluorescence enhancements due to the detection of Zn^{2+} secretion from cells were observed when cells were stimulated by 100 nM insulin (n = 12). These data provide further evidence of insulin-stimulated insulin secretion besides those observed by amperometric detection.

Simultaneous measurements of Zn^{2+} secretion and $[Ca^{2+}]_i$ were performed using FluoZin-3 and the intracellular Ca^{2+} indicator Fura Red as described in Chapter 5. As shown in Figure 6-6, insulin-stimulated Zn^{2+} secretion and $[Ca^{2+}]_i$ responses are well correlated (n = 4). In some cases, Zn^{2+} secretion disappears shortly following the removal of stimulus although $[Ca^{2+}]_i$ remains elevated for several minutes after the stimulation (Figure 6-6B). This could be due to the depletion of readily releasable secretory granules by stimulated secretion. The well correlated responses in $[Ca^{2+}]_i$ and Zn^{2+} secretion further support the critical roles of $[Ca^{2+}]_i$ in insulin-stimulated secretion.

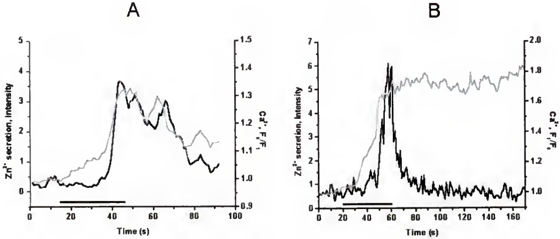

Figure 6-6. Simultaneous measurements of $[Ca^{2+}]_i$ and Zn^{2+} secretion from isolated β-cells. Cells were stimulated with 100 nM insulin for a short period as indicated by bars under the traces. Images were acquired at 1 s per image pair. Zn^{2+} signals were analyzed as direct intensities as indicated by the left Y-axis in each graph and $[Ca^{2+}]_i$ was expressed as F_0/F_1 indicated by the right Y-axis in each graph. The $[Ca^{2+}]_i$ traces in both graphs are in gray.

Discussion

The discovery that β-cell insulin receptors play a role in normal regulation of insulin secretion provides a potential direct link between impaired insulin secretion and insulin resistance in type 2 diabetes (Aspinwall et al., 1999a; Kulkarni et al., 1999b; Rutter, 1999; Taylor, 1999). Investigation of the signal transduction mechanisms by which insulin exerts the stimulatory effect on insulin secretion from the β-cell is therefore essential. Our data have shown that insulin-stimulated insulin secretion is mediated by functional insulin receptors (Aspinwall et al., 1999a), IRS-1, and PI3-K activation. Activation of these substrates by insulin in β-cells has previously been reported (Leibiger et al., 1998; Xu et al., 1999), and the results presented here illustrate that these effects are directly linked to insulin secretion and increases in $[Ca^{2+}]_i$. Our data also demonstrate that insulin-stimulated increases in $[Ca^{2+}]_i$ and secretion from isolated β-cells are temporally well correlated.

The increase in $[Ca^{2+}]_i$ evoked by insulin appears to be mediated by release of Ca^{2+} from intracellular Ca^{2+} stores based on the localization of the increase, the effects of thapsigargin, and the occurrence of $[Ca^{2+}]_i$ changes in the absence of extracellular Ca^{2+}. The release of intracellular Ca^{2+} requires activation of IRS-1/PI3-K; however, the complete biochemical mechanism is not clear. The study with PLC inhibitor indicates that Ca^{2+} release does not result from PIP_3 activation of PLC via PI3-K; however, because multiple isoforms of PLC exist and the inhibitor used may not cross-react with all isoforms (Zawalich et al., 1995), it is not possible to completely rule out a role for any isoform of PLC in the insulin signaling pathway. One possible explanation of the increases in $[Ca^{2+}]_i$ is due to the inhibition of SERCA pumps on the ER. IRS-1 has been shown to interact with SERCA proteins (Algenstaedt et al., 1997) and it has recently been demonstrated that overexpression of IRS-1 in the clonal β-cell line βTC6-F7 inhibits the uptake of Ca^{2+} into ER, possibly by inhibition of the SERCA pump (Xu et al., 1999). Supporting this notion, it has been observed that $[Ca^{2+}]_i$ changes induced by insulin were initiated slower than that observed with the depolarizing stimulant tolbutamide and had a prolonged lifetime, frequently not returning to baseline after 2 minutes. This would be expected for release occurring by inhibition of the pump since release would essentially occur by "leaking" from ER into the cytosol; however, further experiments would be needed to establish this link.

An important question is whether the increased $[Ca^{2+}]_i$ evoked by insulin is required for the detected exocytosis. In our experiments, it has been found that any treatment that eliminated the $[Ca^{2+}]_i$ increase (IRS-1 knockout, PI3-K inhibition, thapsigargin treatment) also eliminated secretion. An important coupling point between $[Ca^{2+}]_i$ increases and exocytosis in β-cells is PKC. PKC can be activated by Ca^{2+} (Ashcroft, 1994a), and its activation can elicit exocytosis in β-cells independent of entry of Ca^{2+} from the extracellular environment (Eliasson et al., 1996). Our data would support the hypothesis that IRS-1/PI3-K mediated increases in $[Ca^{2+}]_i$ are necessary for insulin-evoked exocytosis and that the $[Ca^{2+}]_i$ changes and secretion are linked at least by PKC, if not at other points in the regulated exocytosis pathway.

It has been shown that inhibition of PI3-K blocks both the $[Ca^{2+}]_i$ increase and exocytosis evoked by insulin. PI3-K may be involved in releasing intracellular Ca^{2+} through an interaction with the ER, and the resulting rise in $[Ca^{2+}]_i$ may be sufficient for activating secretion; however, we cannot rule out that PI3-K has other roles in activating exocytosis. Several lines of evidence suggest that phosphorylated products of phosphatidylinositol play critical functions in the regulation of membrane trafficking along the secretory pathway (De Camilli et al., 1996; Shepherd et al., 1996). PI3-K also forms an essential link between the insulin receptor and glucose transporter translocation and intracellular vesicular trafficking (Cheatham et al., 1994). In addition, PI3-K has been shown to be involved in regulated exocytosis in adrenal chromaffin cells by an interaction with the actin cytoskeleton independent of any effects on Ca^{2+} (Chasserot-Golaz et al., 1998). A direct link between PI3-K and the late granule docking step of regulated exocytosis was also suggested from a recent report that synaptotagmin interacts with PIP_2 and PIP_3 in a Ca^{2+}-dependent manner (Schiavo et al., 1996). Thus, the involvement of PI3-K in autocrine activation of insulin secretion opens up a number of possible routes for secretion regulation in β-cells.

Figure 6-7 presents a summary of the possible pathways for the effects of insulin on $[Ca^{2+}]_i$ and insulin secretion within the β-cell based on the data presented here. Autocrine activation of insulin secretion in the β-cell is mediated by activation of IRS-1 and PI3-K. PI3-K or its phosphatidylinositol products may be involved, with Ca^{2+}, in direct activation of the exocytosis machinery of the cell. IRS-1/PI3-K also appears to evoke release of Ca^{2+} from the ER, by an as yet unknown mechanism. The Ca^{2+} may be directly involved in activating exocytosis; however, our data favor a requirement for PKC activation. Although our results have emphasized autocrine activation of an insulin receptor/IRS-1 pathway, previous investigations have demonstrated a significant role for IRS-2 activation as well. Increased insulin biosynthesis may be mediated by autocrine activation of IRS-2 (Leibiger et al., 1998). In addition, mice with IRS-2 gene knock-outs show defects in islet development (Withers et al., 1998) and IRS-2 in β-cells may mediate IGF-1 receptor effects on β-cell development and peripheral insulin signaling (Withers et al., 1999).

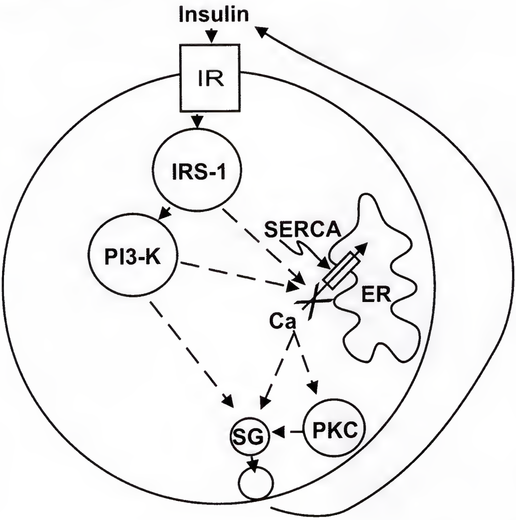

Figure 6-7. Summary of insulin signaling pathway involved in autocrine activation of secretion in pancreatic β-cell. Solid lines indicate established effects or interactions, whereas dashed lines indicate events with unclear mechanism. Insulin applied exogenously or released from secretory granules (SG) binds the insulin receptor (IR), which activates IRS-1/PI3-K leading to release of intracellular Ca^{2+} from the ER, possibly via an inhibition of the SERCA pump. Increased $[Ca^{2+}]_i$ leads to insulin secretion mediated by PKC. The possibility also exists for a more direct involvement of PI3-K in activating exocytosis.

Our data have identified some important contributors to the observed activation of insulin secretion and increased $[Ca^{2+}]_i$ evoked by insulin at the β-cell. These mechanisms are presumably activated by insulin released during normal glucose stimulation *in vivo.* The importance of these effects for normal glucose homeostasis has been demonstrated by the glucose intolerance and reduction of first phase glucose-stimulated insulin secretion in mice lacking the β-cell insulin receptor (Kulkarni et al., 1999b) and impaired insulin secretion associated with IRS-1 polymorphisms (Porzio et al., 1999). Further studies are needed to understand the linkage between effects regulated by glucose versus insulin and possible interactions of insulin with metabolism in the β-cell. Defects in any of the components of the insulin signaling pathway could be involved in impaired insulin secretion and insulin resistance seen in diabetes; however, the actual role of autocrine regulation in diabetes remains to be determined.

CHAPTER 7
SUMMARY AND FUTURE DIRECTIONS

Summary

A novel approach has been developed for spatially and temporally resolved monitoring of Zn^{2+} secretion from pancreatic β-cells using extracellular fluorogenic reactions and confocal laser-scanning fluorescence microscopy. The results strongly support the hypothesis that Zn^{2+} and insulin are co-released from β-cells via exocytosis based on the following observations: 1) Zn^{2+} release is evoked by various insulin secretagogues and the time courses of Zn^{2+} release from single cells agree well with those of exocytotic release measured by amperometry with microelectrodes; 2) Zn^{2+} release is Ca^{2+} dependent and the dynamics of Zn^{2+} release correlate well with the dynamic changes in intracellular Ca^{2+} concentrations, as expected from calcium-secretion coupling; 3) Zn^{2+} and 5-HT secretion from the same cells are well correlated as revealed by simultaneous amperometric and fluorescence measurements; 4) Zn^{2+} release measured with higher temporal resolution (16.5 ms) displays isolated bursts of release with each burst lasting for 100-300 ms, consistent with exocytotic release of individual secretory vesicles; 5) Zn^{2+} release from clusters of cells and islets of Langerhans shows complex patterns of oscillations, which agrees with previous studies of insulin secretion using RIA. Therefore, the detection of Zn^{2+} release from β-cells provides a novel approach for studying exocytosis and indirect way for monitoring insulin secretion from these cells.

This fluorescence imaging approach offers several advantages for monitoring secretion from β-cells including its high sensitivity, high temporal and spatial resolution. It is the first technique that provides spatially and temporally resolved measurements of exocytotic release process from single secretory vesicles. The temporal and spatial characteristics of individual release events from single vesicles have been characterized, which reveals that Zn^{2+}/insulin release from secretory granules is a kinetically controlled process. It is also the first technique reported that has the versatility for monitoring secretory activity from single β-cells, clusters of multiple β-cells, or single islets of Langerhans. This versatility will greatly expand the applications of this technique. Another advantage of this method is the ease of coupling with a Ca^{2+} indicator such as Fura Red for simultaneous measurements of $[Ca^{2+}]_i$ and secretion. At present, this approach also suffers from several limitations. First, this technique does not provide the same quantitative information as immunoassays. Second, the temporal resolution of this technique is still not so good as that provided by amperometry. A comparison of the characteristics of this technique with amperometry and RIA or ELISA is summarized in Table 7-1.

Several applications that are only possible with the temporal resolution and spatial resolution of this technique have been demonstrated. One of these applications is the study of the spatial organization of β-cell exocytosis, which is made possible with the spatially resolved measurements of secretion at the single-cell level. It has been observed that secretion from single β-cells is localized to an active area of plasma membrane that comprises ~50% of the cell circumference and this active area of secretion is co-localized with Ca^{2+} channels on the membrane. These data suggest that β-cells possess a spatial organization of exocytosis in which Ca^{2+} channels, exocytotic membrane proteins and/or secretory vesicles are spatially co-localized in an active zone of secretion on the plasma membrane.

Table 7-1. Comparison of the imaging approach, amperometry, and RIA or ELISA for monitoring secretion from pancreatic β-cells.

	Fluorescence imaging	Amperometry	RIA or ELISA*
Mass sensitivity	< 1 amol	< 1 amol	100 amol or more
Temporal resolution	16.5 ms	μs to ms	20 s
Spatial resolution	~1 μm	Dependent on the size of electrode, but it is single-point measurement	N/A
Quantitative?	Difficult to quantitate the exact amount of release from cells	Amount of release can be quantitated according to Faraday's Law	Quantitative
Applications	Single cells, cell clusters, single islets	Single cells only	Single islets or a population of cells or islets
Throughput	Multiple cells per measurement	One cell per measurement	Laborious

* Westerlund et al., 2001.

The temporal and spatial patterns of Zn^{2+} secretion from clusters of cells or single islets of Langerhans have also been investigated with this approach. Complex patterns of oscillatory secretion from islets and cell clusters including those fast pulses with a period of 10-30 s have been observed. With previous techniques, it was not possible to resolve these fast pulses of secretion due to the limited temporal resolution. With the spatially resolved measurements of secretion from multiple cells, the temporal relationships of secretion from different cells and the heterogeneity of secretion can be examined. Zn^{2+} secretion from islets and cell clusters appears to be spatially synchronized among different regions, yet spatially heterogeneous in amplitudes. These observations suggest that cells in islets or clusters communicate with each other leading to the apparent synchrony in response. The mechanisms of such cellular communication are still unclear and warrant further studies.

In this work, Zn^{2+} release is monitored as an indirect measure of insulin secretion from pancreatic β-cells. Since Zn^{2+} is endogenous release product from both pancreatic β-cells and zinc-containing hippocampal neurons, the capability of detection of Zn^{2+} release at the level of single exocytotic event by this technique would be valuable for fundamental studies of exocytosis in these cells. The detection of Zn^{2+} release from cells itself would also be of interest for uncovering the potential roles of Zn^{2+} release in endocrine and neuronal signaling.

Finally, this work presents a novel approach for the detection of secretion based on rapid extracellular fluorogenic reactions and fluorescence imaging. Development of new fluorescence probes for other compounds and other reaction schemes may allow this approach to be a general route to the detection of secretion from many types of cells. Besides physiological studies, the speed and simple set-up of this imaging method may also have applications in high throughput drug screening. For example, the technique applied to β-cells may prove to be a valuable cell-based assay for rapidly screening compounds that elicit insulin secretion as potential diabetic drugs.

Future Directions

Investigation of Cell-to-cell Communication in Synchronized Secretion

The observation of spatially synchronized Zn^{2+} secretion among different regions in cell clusters and islets suggests that the islet or cell cluster functions as a single unit, where β-cells operate in a coordinated fashion to release insulin synchronously. This hypothesis is also supported by the observation of synchronized oscillations in $[Ca^{2+}]_i$ among cell clusters and islets (Gylfe et al., 1991; Santos et al., 1991; Valdeolmillos et al., 1993). It is still unclear how such coordination among islet β-cells is maintained. β-cells within islets are coupled by gap junctions, which allow the transfer of ions and small molecules between coupled cells. Several studies have suggested that the gap junctional coupling between β-cells may be important for synchronized oscillations in secretion and $[Ca^{2+}]_i$ (Meissner, 1976; Meda et al., 1982). Recently, however, several studies suggest that gap junctions are not required for synchronized oscillations in $[Ca^{2+}]_i$ in response to glucose (Bertuzzi et al., 1999; Squires et al., 2000) and a diffusible factor was proposed for such synchronization in $[Ca^{2+}]_i$ responses (Grapengiesser et al., 1999). It is of interest to gain a better understanding of the mechanisms underlying the coordinated β-cell activities since a breakdown in such coordination could lead to a loss in oscillatory secretion, which is considered as an early symptom in type 2 diabetes.

The fluorescence imaging approach developed in this work provides a unique opportunity to study cell-to-cell communication due to its capability of monitoring secretion from multiple cells simultaneously with good spatial resolution. When an islet is exposed to a glucose challenge, synchronized secretory responses can be monitored by correlating the temporal responses from different regions within the islet. The possibility of diffusible factors in synchronized secretion may be revealed by imaging secretion simultaneously from several clusters of cells or islets that are close to each other, but not physically connected. The roles of gap junctions in synchronized secretion can also be investigated by using different drugs that disrupt gap junctions, while examining the spatial synchrony of secretion with an islet or cluster under such conditions. With these studies, it may be possible to reveal the mechanisms behind synchronized secretion from islet β-cells.

Autocrine Effect of Insulin on Insulin Secretion

The potential autocrine effect of insulin on its own secretion has remained controversial for decades because many studies yielded conflicting evidence on the modulation of insulin secretion by insulin in whole islets or *in vivo*. Most early studies show that glucose-stimulated insulin secretion from rat islets and perfused pancreas is suppressed in the presence of exogenous insulin, leading many to believe that insulin has an inhibitory effect on insulin secretion (Ammon and Verspohl, 1976; Iversen and Miles, 1971). Recently, however, several lines of evidence have suggested that insulin has a positive feedback on its own secretion. Direct evidence for the stimulatory effect of insulin on insulin secretion has been obtained by application of exogenous insulin to isolated β-cells and detecting secretion by amperometry (Aspinwall et al., 1999a). Our data presented in this work have demonstrated insulin-stimulated insulin secretion is mediated by functional insulin receptors, IRS-1, and PI3-K activation (Aspinwall et al., 2000). The positive effect on insulin secretion from isolated β-cells has also been demonstrated by activating the insulin receptor signaling pathway with an insulin mimetic drug L-783, 281 (Roper et al., 2002) or with long-term insulin treatment (Xu et al., 2000). Nevertheless, recent studies on intact islets still generate conflicting results. While in one report the activation of the insulin receptor pathway by L-783, 281 has been shown to have an inhibitory effect on glucose-stimulated insulin secretion from human pancreatic islets (Persaud et al., 2002), the other report shows L-783, 281 enhances glucose-stimulated insulin secretion from mouse pancreatic islets (Westerlund et al., 2002). The reasons for these controversies are not clear, but this picture may be complicated by the different types of species, the types of preparations, and the different techniques for monitoring secretion that have been used.

Despite the controversy about the effect of insulin on insulin secretion, the potential *in vivo* significance of such autocrine effect has been well demonstrated by targeted inactivation of insulin receptors in pancreatic β-cells (Kulkarni et al., 1999b). Mice lacking insulin receptors in β-cells suffer insulin secretory defects similar to those found in human patients in NIDDM, suggesting an important role of autocrine signaling in insulin secretion and glucose homeostasis *in vivo*. The imaging technique developed in this research is applicable to the monitoring insulin secretion from both isolated β-cells and intact islets. It may be possible to unveil the controversial autocrine effect of insulin by monitoring insulin secretion from different cell preparations from different species by using one single technique. This work would be of great interest due to the potential role of autocrine signaling *in vivo.*

Monitoring of Zn^{2+} Release from Neurons

Large amounts of Zn^{2+} are present in the brain, yet the roles of Zn^{2+} in brain functions are still unknown (Huang, 1997). Zn^{2+} is highly concentrated in the synaptic vesicles of a subset of glutametergic neurons such as hippocampal mossy fibers. Large amounts of Zn^{2+} are thought to be released along with glutamate via exocytosis, so it has been hypothesized that Zn^{2+} could play an important neuromodulatory roles at glutamate synapses. The released Zn^{2+} has been shown to influence NMDA, GABA, and opiate receptors and play a role in the development of Alzheimer's Disease and excitotoxicity (Frederickson et al., 2000). Given the potential roles of released Zn^{2+} in synaptic signaling, it would be of interest to investigate the kinetics and biophysics of Zn^{2+} release from neurons.

So far, little is known about the kinetics of Zn^{2+} release from neurons. For example, it is often assumed that Zn^{2+} and glutamate are co-released from glutametergic neurons; however, the co-release of these substances has never been directly demonstrated or characterized. In this work, a novel, sensitive imaging approach has been demonstrated for monitoring Zn^{2+} release at the single cell level with high temporal and spatial resolution. It will be interesting to apply this imaging technique to investigate the temporal and spatial characteristics of neuronal Zn^{2+} release. Functional roles of Zn^{2+} release may be revealed by this study.

APPENDIX A
NIKON RCM 8000 CONFOCAL LASER-SCANNING SYSTEM

Introduction of the System

Nikon RCM 8000 confocal system is an integrated video-rate confocal laser-scanning microscope (CLSM) that has been specifically designed for real-time fluorescence ratio imaging. The system consists of a Nikon Diaphot 300 inverted microscope, a Coherent INNOVA Enterprise argon ion laser (351 and 488 nm), an Omnichrome argon-krypton ion laser (488 and 568 nm), confocal mechanical unit, photomultiplier tubes (PMT) as detectors, and computer control units. This system is capable of performing high-speed point-scanning at 30 full-frames (512 × 486 pixels per frame) per second, which is the standard RS-170 video rate.

Figure A-1 shows the optical layout of this microscope. The laser excitation beams (351, 488, or 568 nm) are selected by separate excitation filters and made coincident by reflection mirrors. The input beam then passes through a spatial filter, which also acts as a beam-expander, to generate a fully collimated beam (not shown). The mechanic shutter of laser is software controlled. The input beam is then reflected by the excitation dichroic mirror and enters the scanner. The scanner consists of a resonant galvanometer for horizontal scanning (scanning the horizontal line at 15.7 kHz) and a linear servo galvanometer for vertical scanning (scanning the vertical line at 30 Hz). The interlaced scanning by these two galvanometers allows the beam to scan 30 full-frames per second. The precise positions of the beam are sensed by optical feedback from an independent reference beam (not shown) and processed by complex electronics and computer software. The details of the beam scanning in this instrument have been previously described (Tsien and Bacskai, 1995).

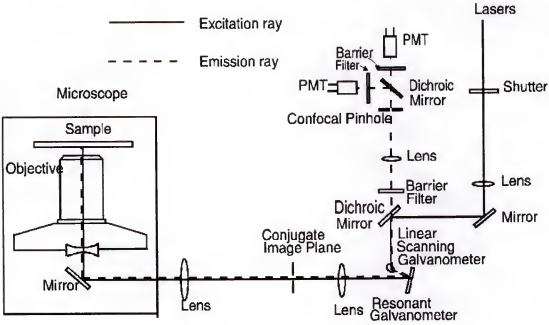

Figure A-1. Optical layout of Nikon RCM 8000 confocal laser-scanning microscope. The entire diagram is a top view, except for the microscope portion. (Adapted from Tsien and Bacskai, 1995).

The excitation beam is then relayed into the microscope objective by several relay lenses and focused onto the sample by the objective. The Nikon CF Fluor 40x, NA 1.15 water immersion objective is used for most imaging experiments. This objective is specifically designed for this confocal system as an integral part of the chromatically corrected optical path (UV and Visible 340-768 nm). The water immersion objective is of advantage because it eliminates the spherical aberration caused by the mismatch of refractive indices, which is especially obvious for imaging thick samples such as pancreatic islets. The 40x objective has a working distance ~200 μm. The imaging field of view is ~150 μm with the 40x objective, corresponding to approximately 0.3 μm/pixel for both the x and y directions with image dimensions of 512 × 486 pixels.

The emission light from the sample is recollected by the objective and relayed back through the same lenses, and de-scanned by the galvanometers and transmitted through the excitation dichroic mirror. It is then focused onto the confocal aperture, an adjustable iris diaphragm with four different sizes. If the confocal aperture is bigger, it will allow more light to pass onto the detector; however, the confocality is compromised, reducing the spatial resolution, especially the Z-axis resolution. The emission light passing through the confocal aperture is either reflected onto one PMT by the emission dichroic mirror or pass through onto the other PMT. The two detection channels allow for simultaneous monitoring of the fluorescence at two different wavelengths and emission ratio imaging.

The detected signals are digitized using an 8-bit analog-to-digital converter and images are generated and displayed in 256 gray levels by the imaging processor. The control units for imaging operation and processing include a main confocal control unit and a control workstation. The main control unit, which runs on an OS9 operating system, controls all the electric elements in the confocal mechanical unit and has built-in image processors (MAX VIDEO) that process images at high speed. The workstation is connected to the main control unit by local area network and controls the RCM 8000 system and image file management and data analysis by RCM software. The images can be recorded online using an Optical Monochrome Disc Recorder (OMDR) from Panasonic. The OMDR can record 30 images per second.

Imaging Operation

Image Acquisition Modes

With two detection channels available, the confocal system provides both single-channel and dual-channel acquisition modes. Single-channel acquisition is commonly used to monitor the dynamic changes in fluorescence intensities for samples that only have one emission maximum wavelength. Dual-channel acquisition is designed to simultaneously monitor changes in fluorescence intensities at two different emission wavelengths. In this acquisition mode, a pair of images is generated for one full-frame scan. Since the OMDR is a monochrome image recorder, all images stored are in gray-scale. Pseudo-color ratio images can be generated by the RCM software for both single-channel and dual-channel acquisition modes. Ratio images are of advantage in term of image presentation because changes in fluorescence intensities are highlighted by colors. To generate ratio images in single-channel acquisition mode, one image is used as a reference image and all subsequent images are presented as ratios against the reference image so that changes in fluorescence intensities with respect to the reference image are presented in different colors. In dual-channel ratio imaging, the ratios are intensities at one channel (short emission wavelength) against those at the other channel (long emission wavelength).

For quantitative measurements, dual-channel (dual-wavelength) emission ratio imaging is of advantage compared to single-channel imaging because dual-channel ratios cancel out the uneven dye content in the sample and changes in instrumental sensitivity such as variation in laser excitation power and detection efficiency. One example of dual-channel emission ratio imaging is the use of ratiometric dye indo-1 for the quantitative imaging of intracellular Ca^{2+} concentrations (See Appendix B for details).

Scanning Modes

The confocal system offers several scanning modes including full-frame scanning, band scanning, line scanning, and z-axis scanning. In most imaging applications, the full-frame scanning mode is used. With this scanning mode, the temporal resolution is limited to 33 ms because the scanning rate is 30 frames per second. If time resolution is less critical than the signal-to-noise ratio (S/N), a number of frames are typically averaged to generate one image. For example, a 16-frame average will give an image acquisition rate of ~500 ms per image. Band scanning and line scanning modes are only used when high temporal resolution is required. In band scanning mode, the full frame is divided into a number of identical bands and the laser beam scans only one band of choice. For example, the scan area of an 8-band scanning is 1/8 of the full frame, which will allows the beam to scan the entire band 240 times per second, i.e. 240 images per second. The 8-band scanning provides the highest temporal resolution in band scanning mode. In line scanning mode, the vertical scanning galvanometer is turned off and the horizontal line is scanned at 15.7 kHz. Therefore, sub-millisecond temporal resolution can be achieved with this confocal imaging system if the S/N allows. In both band scanning and line scanning modes, frame averaging cannot be performed.

Selection of Optical Filters

Optical filters are integral components of the confocal microscope. Good selection of optical filters improves the specificity and sensitivity of measurements. As in Figure A-1, filters used in the system include excitation filters used for selecting specific laser line, the excitation and emission dichroic mirrors, and barrier filters following the dichroic mirrors. All filters are accessible for modification or replacements. Most filters used are custom-made from Chroma Technology. The choice of filters depends on the excitation and emission wavelengths of the fluorophores of interest. For example, the Ca^{2+} fluorophore indo-1 is excited at 351 nm and it has two emission maximums at 405 and 480 nm. In this case, a 340 ± 30 nm band-pass filter is used to allow 351 nm laser line to pass for excitation while rejecting light at other wavelengths from the argon ion laser. A 380 nm cut-off excitation dichroic mirror is used, which allows the 351 nm excitation beam to be reflected toward objective while allowing emitted fluorescence > 380 nm to pass. The emitted fluorescence of indo-1 is split by a 450 nm cut-off dichroic mirror to separate detection channels. If autofluorescence or background fluorescence of the sample is a problem, 405 ± 10 and 480 ± 10 nm band-pass filters will be used for each detection channel to reduce the background fluorescence. While the use of these band-pass filters will greatly reduce background fluorescence, it also reduces signals from indo-1. Band-pass filters should be used only if an improvement in signal-to-background (S/B) is expected.

Optimization of Imaging Performance

Ideal imaging experiments should have high detection sensitivity and high spatial and temporal resolution. In reality, however, these three parameters often cannot be achieved at the same time. For example, temporal resolution is usually compromised in order to improve spatial resolution and detection sensitivity. There are many factors that directly affect the imaging performance. Probably the most important factors are proper alignment of the optical system (discussed in a later section) and good selection of optical filters. Some other parameters that directly affect the imaging performance include excitation power, detector gains, confocal pinhole size, and image acquisition rate. All four parameters are required to be routinely optimized for good imaging performance. The optimization of excitation power and detector gain is common for all fluorescence imaging. The excitation power is optimized in compromise with the signal levels and photobleaching. In this confocal setup, the excitation power is tuned either by adjusting the laser output power or by using the neutral density filter wheel. The detector gains are optimized to have signal levels in the linear dynamic range. Too high a gain will lead to high noise level and may have saturated signals. The size of the confocal pinhole will affect the spatial resolution of imaging and the signals. The smaller pinhole (if not smaller than the diffraction limit) leads to greater Z-axis resolution, but it reduces the amount of light to be detected. If background fluorescence is not a problem, an increase in the size of pinhole will increase the detection sensitivity with little loss in Z-axis resolution. In many situations, a large pinhole may be required to get more signal when there is limited light level. Temporal resolution is important in dynamic imaging studies and is dependent on the image acquisition rate. Since this confocal system is a point-scanning system, the exposure time for each pixel is only ~130 ns during one full-scan. In this situation, intrinsic noise is square root of signal based Poisson statistics (Pawley, 1995) so that S/N is usually poor if the signal is not high. For slow imaging experiments, the S/N is improved by averaging a number of frames. If high temporal resolution is required, the system needs to be optimized to have high signals and low dark noise from the detector in order to get good S/N. This is typically done using relatively high laser excitation power and low detector gain.

Data Analysis and Image Presentation

Dynamic changes in fluorescence intensities are analyzed off-line by Simca image analysis software (C-IMAGING Systems). Images stored in the OMDR are played back using the playback function of the RCM software. During playback, images are captured from the display screen by 8-bit image grabber and intensities are analyzed by the Simca software. The rate of image playback is 1.13 s per frame and the capture rate in Simca should be set at the same interval. Regions of interest (ROIs) with any shapes can be drawn and plots of average fluorescence intensities as a function of time within ROIs will be displayed during image capturing. Intensity data can be saved as MS EXCEL files for further analysis. For dual-channel images, images are played back in single-channel mode and average intensities with ROIs as a function of time are analyzed independently for each channel. If ratios of dual-channel images will be used, the ROIs used for both channels need to be the same and the images for each channel should be captured on the same time scale.

Ratio images and image montages can be directly generated by the RCM software. Images generated by the RCM system need to be converted and exported as TIFF images for any presentation on PC. To do this, all images of interest will be resaved on the hard drive of the control unit after being played back from the OMDR. All processing for the exported TIFF images is performed using Adobe Photoshop (Version 6.0). To make AVI format movies, a series of images will be imported to MetaMorph Software (Universal Imaging Corporation) using the build stack function and images can be linked and saved as AVI movie files. If a series of Z-axis scanning images is available, 3-D reconstruction can also be performed with the build stack function of

MetaMorph. The intensity profiles of individual images can also be analyzed by MetaMorph.

Instrumental Maintenance

Alignment

The most important maintenance to be performed in this confocal system is the alignment of the laser beam and pinhole aperture positions to achieve the best sensitivity for detection. As shown in Figure A-1, the confocal pinhole needs to be aligned to the position where it allows emission light from the focal point of the sample to pass. The other important alignment is to align the position of laser beam so that it will pass through the spatial filter in the middle of the beam-expander (diagram not shown). Both pinhole and laser beam position are adjusted by two optical alignment screws. To perform an alignment, a standard homogeneous sample such as 500 nM fluorescein is used. A good alignment is achieved when the brightest image and relatively homogeneous intensities in the field of view are observed.

Lasers

The argon ion laser head is cooled to 30° C by the Liquid/Liquid Coolflow system during all operations. The water circulated within the laser head is distilled water and is filtered through a 5 μm pore prefilter (Fisher, Item number: 09034162). If contamination on the filter is obvious, both the filter and circulation water need to be replaced. During daily operation, the laser is warmed up at full power for at least 30 min to optimize the gas pressure in the laser tube. The krypton-argon ion laser uses an air-cooling system. Once the laser is turn-off, the air-cooling system needs to continue running for at least 5-10 min. Standby function is recommended for both lasers during periods that no images are acquired. A routine check of the maximum laser emission power for both lasers is required. If an obvious drop in laser emission power is observed, realignment of the laser mirrors will be necessary (see manuals for procedures).

APPENDIX B
CONFOCAL IMAGING OF INTRACELLULAR FREE Ca^{2+} CONCENTRATIONS

Fluorescent Ca^{2+} Probes

Ca^{2+} is an important secondary messenger in a variety of cells. Numerous cellular functions are regulated by Ca^{2+}. The regulatory role of Ca^{2+} in secretion of neurotransmitters and hormones is just one of the examples (Augustine, 2001). Studies of intracellular Ca^{2+} dynamics have been greatly aided by the development of Ca^{2+} sensitive fluorescent probes mainly by Tsien and colleagues (Grynkiewicz et al., 1985; Minta et al., 1989) and scientists at Molecular Probes (Gee et al., 2000). All fluorescent Ca^{2+} probes change their fluorescent properties upon Ca^{2+} binding and they can be divided into two groups, ratiometric and single wavelength indicators based on whether there is a shift in excitation or emission wavelength upon Ca^{2+} binding. Fura-2 and indo-1 are the most commonly used ratiometric dyes for quantitative Ca^{2+} measurements. Commonly used single wavelength indicators include fluo-3, fluo-4, calcium green, rhod-2, and Fura Red. More information about fluorescent Ca^{2+} probes is available from *The Handbook of Fluorescent Probes and Research Products* by Molecular Probes.

Confocal Imaging of Ca^{2+} in Pancreatic β-cells

Confocal laser-scanning microscopy has become one of the most important techniques for measurements of intracellular Ca^{2+} concentrations ($[Ca^{2+}]_i$) because it allows the precise spatial and temporal analysis of intracellular Ca^{2+} dynamics. In this work, indo-1, fluo-4, and Fura Red have been used for imaging Ca^{2+} in pancreatic β-cells.

Prior to imaging, all dyes were loaded into the β-cells by a similar procedure. The dyes in acetoxymethyl ester (AM) format were dissolved by DMSO to make 1-3 mM stock solutions and stored in freezer. Pancreatic β-cells used for imaging were plated on 25 mm glass coverslips and incubated in RMPI 1640 medium. During dye loading, cells were incubated with one of the following dyes (2 μM indo-1 AM, 2 μM fluo-4 AM, or 5 μM Fura Red AM) in KRB containing 2.4 mM Ca^{2+} at 37° C, 5% CO_2 for 30 min. After loading, cells are washed with dye-free KRB twice and then the coverslip containing cells is placed into a coverslip holder and incubated in KRB at 37° C by a micro-incubator (Medical Systems) on the stage on the Nikon confocal microscope for imaging experiments.

Indo-1 ratio imaging. The dual-emission ratiometric calcium indicator, indo-1, will be used for quantitatively imaging $[Ca^{2+}]_i$. The dye is excited at 351 nm and its emission maximums are at 405 and 480 nm. Fluorescence signals of 405 and 480 nm were separated by 450 nm cutoff dichroic mirror and simultaneously collected using the two PMTs on the confocal microscope. 405 ± 10 nm and 480 ± 10 nm emission band-pass filters (Chroma) were used for each channel in order to reduce cellular autofluorescence. The fluorescence intensities at 405 nm and 480 nm are used to generate fluorescence ratio R and $[Ca^{2+}]_i$ can be calculated using the following equation:

$$[Ca^{2+}]_i = K_d\left(\frac{R - R_{\min}}{R_{\max} - R}\right)\left(\frac{F_{480,\min}}{F_{480,\max}}\right) \qquad \text{(B.1)}$$

where K_d is the effective dissociation constant of indo-1, F is measured fluorescence intensity, R is the ratio of fluorescence intensities F_{405}/F_{480}, R_{min} and $F_{480,\,min}$ are the ratio and fluorescence intensity at 480 nm obtained in the presence of zero free Ca^{2+}, R_{max} and

$F_{480,\,max}$ are the ratio and fluorescence intensity at 480 nm obtained at saturated Ca^{2+} (~40 μM). The R_{min} and R_{max} for indo-1 loaded in the cells were measured daily using a two-point calibration. In this calibration, cells for imaging were incubated in KRB containing 20 μM 4-Br-A23187, a calcium ionophore. The calcium ionophore allows fast transport of Ca^{2+} ions across the cell membrane. Cells used for measuring R_{min} were incubated in KRB with 200 μM EGTA and without Ca^{2+}. The ratio obtained is Rmin in the presence of zero free Ca^{2+}. Cells for measuring R_{max} were incubated in KRB with 2.4 mM Ca^{2+}. Due to the presence of ionophore, Ca^{2+} was at saturated level inside the cells and R_{max} was measured. Typically, 5-10 cells were measured and averaged to obtain R_{min} and R_{max}. K_d and $F_{480,\,min}/F_{480,\,max}$ were determined using an *in vitro* calibration on the confocal system at room temperature using cell-free Ca^{2+}-EGTA buffer containing 50 μM indo-1 free acid (free Ca^{2+} concentrations ranges from 0 to 40 μM). The buffered Ca^{2+} solutions were prepared using the calcium calibration buffer kit #1 from Molecular Probes (Catalog number C-3008). The K_d and the ratio $F_{480,\,min}/F_{480,\,max}$ measured on the confocal system were 214 nM and 2.7, respectively. K_d and $F_{480,\,min}/F_{480,\,max}$ need to be recalibrated if a major instrumental change occurs.

The PMT voltages were adjusted to give ratios at basal Ca^{2+} level between 0.5-1.0 nd fluorescence intensities from both channels were between 50-100 on the 256 gray levels. With this adjustment, fluorescence intensities at both channels were within the dynamic range and changes in ratios can be sensitively measured. One concern for indo-1 imaging is its tendency to be photobleached. The laser power used for excitation was typically controlled to be below 10 μW in order to reduce the effect of photobleaching.

Imaging with single wavelength indicators. Single wavelength dyes such as fluo-4 and Fura Red have also been used to measure Ca^{2+} dynamics in β-cells. These dyes are of advantage because of the visible light excitation and good photo-stability. Both dyes are excited at 488 nm and fluo-4 emits at 516 nm, while Fura Red emits at 657 nm. Fluo-4 exhibits a fluorescence increase upon Ca^{2+} binding, while Ca^{2+} binding of Fura Red leads to a fluorescence decrease. In the imaging experiments, a 525 ± 15 nm band-pass filter and a 595 nm long-pass filter were used for the detection of fluo-4 and Fura Red fluorescence, respectively.

For a single wavelength Ca^{2+} indicator, $[Ca^{2+}]_i$ can be calculated using the following equation:

$$[Ca^{2+}]_i = K_d \times (F - F_{\min} / F_{\max} - F) \qquad \text{(B.2)}$$

where F is the measured fluorescence intensity, F_{min} and F_{max} are fluorescence intensity in the presence of zero free Ca^{2+} and saturated Ca^{2+} level. The problem of single wavelength dyes is that F_{min} and F_{max} cannot be easily obtained because the dye concentration in the cell is not even and any changes in instrumental sensitivity will lead to changes in fluorescence intensity. In contrast, such factors are cancelled out in ratiometric dual-channel imaging. Due to this problem, Ca^{2+} changes measured by fluo-4 and Fura Red were plotted as relative changes in intensity. F_1/F_0 ratio was used for fluo-4 and F_0/F_1 ratio was used for Fura Red since these two indicators change their fluorescence in opposite directions upon Ca^{2+} binding. Here, F_0 is measured intensity at the beginning of recording and F_1 is measured intensity at any point of time. Increases in both types of ratios reflect increases in $[Ca^{2+}]_i$.

LIST OF REFERENCES

Algenstaedt, P.; Antonetti, D. A.; Yaffe, M. B.; Kahn, C. R. *J. Biol. Chem.* **1997**, *272*, 23696-23702.

Almers, W. *Annu. Rev. Physiol.* **1990**, *52*, 607-624.

Alter, C. A.; Wolf, B. A. *Biochem. Biophys. Res. Comm.* **1995**, *208*, 190-197.

Ämmälä, C.; Eliasson, L.; Bokvist, K.; Larsson, O.; Ashcroft, F. M.; Rorsman, P. *J. Physiol.* **1993**, *472*, 665-688.

Ammon, H. P. T.; Verspohl, E. *Endocrinology* **1976**, *99*, 1469-1476.

Arslan, P.; Virgilio, F. D.; Beltrame, M.; Tsien, R. Y.; Pozzan, T. *J. Biol. Chem.* **1985**, *260*, 2719-2727.

Ashcroft, S. J. *Diabetologia* **1994a**, *37(Suppl. 2)*, S21-29.

Ashcroft, F. M.; Proks, P.; Smith, P. A.; Ämmälä, C.; Bokvist, K.; Rorsman, P. *J. Cell Biochem.* **1994b**, *55s*, 54-65.

Aspinwall, C. A.; Brooks, S. A.; Kennedy, R. T.; Lakey, J. R. T. *J. Biol. Chem.* **1997**, *272*, 31308-31314.

Aspinwall, C. A.; Lakey, J. R. T.; Kennedy, R. T. *J. Biol. Chem.* **1999a**, *274*, 6360-6365.

Aspinwall, C. A.; Huang, L.; Lakey, J. R. T.; Kennedy, R. T. *Anal. Chem.* **1999b**, *71*, 5551-5556.

Aspinwall, C. A.; Qian, W. J.; Roper, M. G.; Kulkarni, R. N.; Kahn, C. R.; Kennedy, R. T. *J. Biol. Chem.* **2000**, *275*, 22331-22338.

Augustine, G. J. *Curr. Opin. Neurobiol.* **2001**, *11*, 320-326.

Avruch, J. *Nature* **1998**, *391*, 846-847.

Bae, Y. S.; Cantley, L. G.; Chen, C.-S.; Kim, S.-R.; Kwon, K.-S.; Rhee, S. G. *J. Biol. Chem.* **1998**, *273*, 4465-4469.

Barbosa, R. M.; Silva, A. M.; Tome, A. R.; Stamford, J. A.; Santos, R. M.; Rosario, L. M. *J. Physiol.* **1998,** *510*, 135-143.

Bendayan, M. *J. Histochem. Cytochem.* **1992,** *40*, 327-331.

Bennett, B. D.; Jetton, T. L.; Ying, G.; Magnuson, M. A.; Piston, D. W. *J. Biol. Chem.* **1996,** *271*, 3647-3651.

Berggren, P. O.; Larson, O. *Biochem. Soc. Trans.* **1994,** *22*, 12-18.

Bergsten, P.; Hellman, B. *Diabetes* **1993a,** *42*, 670-674.

Bergsten, P.; Hellman, B. *Biochem. Biophys. Res. Commun.* **1993b,** *192*, 1182-1188.

Bergsten, P.; Grapengiesser, E.; Gylfe, E.; Tengholm, A.; Hellman, B. *J. Biol. Chem.* **1994,** *269*, 8749-8753.

Bertuzzi, F.; Davalli, A. M.; Nano, R.; Socci, C.; Codazzi, F.; Fesce, F.; Di Carlo, V.; Pozza, G.; Grohovaz, F. *Diabetes* **1999,** *48*, 1971-1978.

Bloc, A.; Cens, T.; Cruz, H.; Dunant, Y. *J. Physiol.* **2000,** *529*, 723-734.

Blundell, T.; Dodson, G. G.; Hodkin, D.; Mercola, D. *Adv. Protein Chem.* **1972,** *26*, 279-402.

Bokvist, K.; Eliasson, L.; Ämmälä, C.; Renstrom, E.; Rorsman, P. *EMBO. J.* **1995,** *14*, 50-57.

Bokvist, K.; Holmqvist, M.; Gromada, J.; Rorsman, P. *Pflügers Arch.* **2000,** *439*, 634-645.

Bonner-Weir, S. *Diabetes* **1988,** *37*, 616-621.

Bonner-Weir, S. In *Insulin Secretion*; Draznin, B., Melmed, S., LeRoith, D., Eds.; Alan, R. Liss, Inc.: New York, 1989; pp 1-12.

Bonner-Weir, S. In *The Endocrine Pancreas*; Samols, E., Ed.; Raven Press: New York, 1991; p 15.

Brose, N.; Petrenko, A. G.; Südhof, T. C.; Jahn, R. *Science* **1992,** *256*, 1021-1025.

Brown, H.; Meister, B.; Deeney, J.; Corkey, B. E.; Yang, S. N.; Larsson, O.; Rhodes, C. J.; Seino, S.; Berggren, P. O.; Fried, G. *Diabetes* **2000,** *49*, 383-391.

Budde, T.; Minta, A.; White, J. A.; Kay, A. R. *Neuroscience* **1997,** *79*, 347-358.

Chasserot-Golaz, S.; Hubert, P.; Thierse, D.; Dirrig, S.; Vlahos, C. J.; Aunis, D.; Bader, M. F. *J. Neurochem.* **1998**, *70*, 2347-2356.

Cheatham, B.; Vlahos, C. J.; Cheatham, L.; Wang, L.; Blenis, J.; Kahn, C. R. *Mol. Cell. Biol.* **1994**, *14*, 4902-4911.

Chen, T. K.; Luo, G.; Ewing, A. G. *Anal. Chem.* **1994**, *66*, 3031-3035.

Chow, R. H.; von Ruden, L.; Neher, E. *Nature* **1992**, *356*, 60-62.

Chow, R. H.; Lund, P. E.; Loser, S.; Panten, U.; Gylfe, E. *J. Physiol.* **1995**, *485*, 607-617.

Cochilla, A. J.; Angleson, J. K.; Betz, W. J. *Annu. Rev. Neurosci.* **1999**, *22*, 1-10.

Coore, H. G.; Hellman, B.; Phil, E.; Taljedal, I. B. *Biochem. J.* **1969**, *111*, 107-113.

Cortizo, A.; Espinal, J.; Hammonds, P. *FEBS Lett.* **1990**, *272*, 137-140.

Crank, J. *The Mathematics of Diffusion*; Oxford University Press: Oxford, 1975.

Cuajungco, M. P.; Lees, G. J. *Brain Res. Rev.* **1997**, *23*, 219-236.

De Camilli, P.; Scott, D. E.; McPherson, P. S.; Novick, P. *Science* **1996**, *271*, 1533-1539.

DeFronzo, R. A. *Diabetes Rev.* **1997**, *5*, 177-269.

Efendic, S.; Östenson, C.-G. *J. Intern. Med.* **1993**, *234*, 127-138.

Efrat, S.; Linde, S.; Kofod, H.; Spector, D.; Delannoy, M.; Grant, S.; Hanahan, D.; Baekkeskov, S. *Proc. Natl. Acad. Sci. U.S.A.* **1988**, *85*, 9037-9341.

Eliasson, L.; Renstrom, E.; Ammälä,C.; Berggren, P. O.; Bertorello, A. M.; Bokvist, K.; Chibalin, A.; Deeney, J. T.; Flatt, P. R.; Gabel, J.; Gromada, J.; Larsson, O.; Lindstrom, P.; Rhodes, C. J.; Rorsman, P. *Science* **1996**, *271*, 813-815.

Eliasson, L.; Renström, E.; Ding, W. G.; Proks, P.; Rorsman, P. *J. Physiol.* **1997**, *503*, 399-412.

Emdin, S. O.; Dodson, G. G.; Cutfield, J. M.; Cutfield, S. M. *Diabetologia* **1980**, *19*, 279-402.

Falasca, M.; Logan, S. K.; Lehto, V. P.; Baccante, G.; Lemmon, M. A.; Schlessinger, J. *EMBO J.* **1998**, *17*, 414-422.

Ferrannini, E. *Endocr. Rev.* **1998**, *19*, 477-490.

Figlewicz, D. P.; Forhan, S. E.; Hodgson, A. T.; Grodsky, G. M. *Endocrinology* **1984,** *115*, 877-881.

Flatt, P. R.; Bailey, C. J.; Berggren, P. O.; Herberg, L.; Swanston-Flatt, S. K. In *Nutrient Regulation of Insulin Secretion*; Flatt, P. R., Ed.; Portland Press: London and Chapel Hill, 1992; pp 341-386.

Formby, B.; Schmid-Formby, F.; Grodsky, G. M. *Diabetes* **1984,** *33*, 229-234.

Foster, M. C.; Leapman, R. D.; Li, M. X.; Atwater, I. *Biophys. J.* **1993,** *64*, 525-532.

Frederickson, C. J.; Suh, S. W.; Silva, D.; Frederickson, C. J.; Thompson, R. B. *J. Nutr.* **2000,** *130*, 1471S-1483S.

Gao, Z.-Y.; Konrad, R. J.; Collins, H.; Matschinsky, F. M.; Rothenberg, P. L.; Wolf, B. A. *Diabetes* **1996,** *45*, 854-862.

Gazzano, H.; Halban, P.; Prentki, M.; Ballotti, R.; Brandenburg, D.; Fehlmann, M.; Van Obberghen, E. *Biochem. J.* **1985,** *226*, 867-872.

Gee, K. R.; Brown, K. A.; Chen, W. N.; Bishop-Stewart, J.; Gray, D.; Johnson, I. *Cell Calcium* **2000,** *27*, 97-106.

Gee, K. R.; Zhou, Z. L.; Qian, W. J.; Kennedy, R. T. *J. Amer. Chem. Soc.* **2002,** *124*, 776-778.

Gillis, K. D.; Misler, S. *Pfülgers Arch.* **1992,** *420*, 121-123.

Gilon, P.; Henquin, J. C. *J. Biol. Chem.* **1992,** *267*, 20713-20720.

Gilon, P.; Shepherd, R. M.; Henquin, J. C. *J. Biol. Chem.* **1993,** *268*, 22265-22268.

Gilon, P.; Henquin, J. C. *Endocrinology* **1995,** *136*, 5725-5730.

Gilon, P.; Yakel, J.; Gromada, J.; Zhu, Y.; Henquin, J. C.; Rorsman, P. *J. Physiol.* **1997,** *499*, 65-76.

Gold, G.; Grodsky, G. M. *Experientia* **1984,** *40*, 1105-1114.

Grapengiesser, E.; Gylfe, E.; Hellman, B. *Biochem. Biophys. Res. Commun.* **1988,** *150*, 419-425.

Grapengiesser, E.; Gylfe, E.; Hellman, B. *Biochem. Biophys. Res. Commun.* **1999,** *254*, 436-439.

Grodsky, G. M.; Schmid-Formby, F. *Endocrinology* **1985**, *117*, 704-710.

Grynkiewicz, G.; Poenie, R. Y.; Tsien, R. Y. *J. Biol. Chem.* **1985**, *260*, 3440-3450.

Guerineau, N. C.; Bonnefont, X.; Stoeckel, L.; Mollard, P. *J. Biol. Chem.* **1998**, *273*, 10389-10395.

Gupta, B. B. P. *Curr. Sci.* **1997**, *73*, 993-1003.

Gylfe, E. *J. Biol. Chem.* **1988**, *263*, 5044-5048.

Gylfe, E.; Grapengiesser, E.; Hellman, B. *Cell Calcium* **1991**, *12*, 229-40.

Harbeck, M. C.; Louie, D. C.; Howland, J.; Wolf, B. A.; Rothenberg, P. L. *Diabetes* **1996**, *45*, 711-717.

Harrison, N. L.; Gibbons, S. J. *Neuropharmacology* **1994**, *33*, 935-952.

Hellman, B.; Gylfe, E.; Grapengiesser, E.; Lund, P.-E.; Marcström, A. In *Nutrient Regulation of Insulin Secretion*; Flatt, P. R., Ed.; Portland Press: London and Chapel Hill, 1992; pp 213-246.

Hille, B.; Billiard, J.; Babcock, D. F.; Nguyen, T.; Koh, D. S. *J. Physiol.* **1999**, *520*, 23-31.

Holst, L. S.; Mulder, H.; Manganiello, V.; Sundler, F.; Ahren, B.; Holm, C.; Degerman, E. *Biochem. Biophys. Res. Comm.* **1998**, *250*, 181-186.

Howell, S. L.; Kostianovsky, M.; Lacy, P. E. *J. Cell Biol.* **1969**, *42*, 695-705.

Howell, G. A.; Welch, M. G.; Frederickson, C. J. *Nature* **1984**, *308*,736-738.

Howell, S. L.; Jones, P. M.; Persaud, S. J. *Diabetologia* **1994**, *37*, S30-S35.

Huang, E. P. *Proc. Natl. Acad. Sci. U.S.A.* **1997**, *94*, 13386-13387.

Huang, L.; Shen, H.; Atkinson, M. A.; Kennedy, R. T. *Proc. Natl. Acad. Sci. U.S.A.* **1995**, *92*, 9608-9612.

Iversen, J.; Miles, D. W. *Diabetes* **1971**, *20*, 1-5.

Jankowski, J. A.; Schroeder, T. J.; Ciolkowski, E. L.; Wightman R. M. *J. Biol. Chem.* **1993**, *268*, 14694-14700.

Jetton, T. L.; Magnuson, M. A. *Proc. Natl. Acad. Sci. U.S.A.* **1992**, *89*, 2619-2623.

Jonkers, F. C.; Jonas, J. C.; Gilon, P.; Henquin, J. C. *J. Physiol.* **1999**, *520*, 839-849.

Jonkers, F. C.; Guiot, Y.; Rahier, J.; Henquin, J. C. *Br. J. Pharmacol.* **2001**, *133*, 575-585.

Kaether, C.; Salm, T.; Glombik, M.; Almers, W.; Gerdes, H. H. *Eur. J. Cell Biol.* **1997**, *74*, 133-142.

Kahn, B. B. *Cell* **1998**, *92*, 593-596.

Kahn, C. R.; Vicent, D.; Doria, A. *Annu. Rev. Med.* **1996**, *47*, 509-531.

Kahn, S. E.; McCulloch, D. K.; Porte, D. Jr. In *International Textbook of Diabetes Mellitus*, 2nd ed.; Alberi, K. G. M. M., Zimmet, P., Defronzo, R. A., Keen, H., Eds.; John Wiley and Sons: New York, 1997; pp 337-353.

Kamholz, A. E.; Schilling, E. A.; Yager, P. *Biophys. J.* **2001**, *80*, 1967-1972.

Kawagoe, K. T.; Zimmerman, J. R.; Wightman, R. M. *J Neurosci. Methods* **1993**, *48*, 225-240.

Kennedy, R. T.; Huang, L.; Aspinwall, C. A. *J. Am. Chem. Soc.* **1996**, *118*, 1795-1796.

Kim, B. J.; Kim, Y. H.; Kim, S.; Kim, J. W.; Koh, J. Y.; Oh, S. H.; Lee, M. K.; Kim, K. W.; Lee, M. S. *Diabetes* **2000**, *49*, 1325-1333.

Kristiansen, L. H.; Rungby, J.; Sondergaard, L. G.; Stoltenberg, M.; Danscher, G. *Histochem. Cell Biol.* **2001**, *115*, 125-129.

Kulkarni, R. N.; Winnay, J. N.; Brüning, J. C.; Hanahan, D. *Diabetes* **1998**, *47*, A57.

Kulkarni, R. N.; Winnay, J. N.; Daniels, M.; Kahn, C. R. *J. Clin. Invest.* **1999a**, *104*, R69-R75.

Kulkarni, R. N.; Brüning, J. C.; Winnay, J. N.; Postic, C.; Magnuson, M. A.; Kahn, C. R. *Cell* **1999b**, *96*, 329-339.

Kurebayashi, N.; Harkins, A. B.; Baylor, S. M. *Biophys. J.* **1993**, *64*, 1934-1960.

Lang, D. A.; Matthews, D. R.; Peto, J.; Turner, R. C. *N. Engl. J. Med.* **1979**, *301*,1023-1027.

Lang, J. *Eur. J. Biochem.* **1999**, *259*, 3-17.

Larsson, L.-I.; Sundler, F.; Hakanson, R. *Diabetologia* **1976**, *12*, 211-226.

Leibiger, I. B.; Leibiger, B.; Moede, T.; Berggren, P. O. *Mol. Cell* **1998**, *1*, 933-938.

Levitan, E. S. *Methods* **1998**, *16*, 182-187.

Liang, Y.; Matschinsky, F. M. *Annu. Rev. Nutr.* **1994**, *14*, 59-81.

Lillard, S. J.; Yeung, E. S. *J. Neurosci. Methods* **1997**, *75*, 103-109.

Lippard, S. J.; Berg, J. M. *Principles of Bioinorganic Chemistry*; University Science Books: Mill Valley, 1994.

Lombardi, T.; Montesano, R.; Wohlwend, A.; Amherdt, M.; Vassalli, J.; Orci, L. *Nature* **1985**, *313*, 694-696.

Lund, P. E.; Gylfe, E.; Hellman, B. *Biochem. Int.* **1989**, *19*, 83-87.

Mahadevan, I. B.; Kimber M. C.; Lincoln, S. E.; Tiekink, E. R. T.; Ward, A. D.; Betts, W. H.; Forbes, I. J.; Zalewski, P. D. *Aust. J. Chem.* **1996**, *49*, 561-568.

Maiti, S.; Shear, J. B.; Williams, R. M.; Zipfel, W. R.; Webb, W. W. *Science* **1997**, *275*, 530-532.

Martin, F.; Ribas, J.; Soria, B. *Biochem. Biophys. Res. Commun.* **1997**, *235*, 465-468.

Meda, P.; Kohen, E.; Kohen, C.; Rabinovitch, A.; Orci, L. *J. Cell Biol.* **1982**, *92*, 221-226.

Meissner, H. P. *Nature* **1976**, *262*, 502-504.

Minta, A.; Kao, J. P.; Tsien, R. Y. *J. Biol. Chem.* **1989**, *264*, 8171-8178.

Mochida, S. *Neurosci Res.* **2000**, 36, 175-182.

Moens, K.; Himberg, H.; Flamez, D.; Huypens, P.; Quartier, E.; Ling, Z.; Pipeleers, D.; Gremlich, S.; Thorens, B.; Schuit, F. *Diabetes* **1996**, *45*, 257-261.

Molnar, E.; Varadi, A.; McIlhinney, R. A.; Ashcroft, S. J. *FEBS Lett.* **1995**, *371*, 253-257.

Monck, J. R.; Robinson, I. M.; Escobar, A. L.; Vergara, J. L.; Fernandez, J. M. *Biophys. J.* **1994**, *67*, 505-514.

Newgard, C. B.; McGarry, J. D. *Annu. Rev. Biochem.* **1995**, *64*, 678-719.

Nilsson, T.; Arkhammar, P.; Berggren, P. O. *Biochem. Biophys. Res. Commun.* **1988,** *153*, 984-991.

Norman, A.W.; Litwack, G. *Hormones*, 2nd ed.; Academic Press: San Diego, 1997; pp 193-227.

Ohara-Imaizumi, M.; Nakamichi, Y.; Tanaka, T.; Ishida, H.; Nagamatsu, S. *J. Biol. Chem.* **2002**, *277*, 3805-3808.

O'Rahilly, S.; Turner, R. C.; Matthews, D. R. *N. Engl. J. Med.* **1988,** *318*,1225-1230.

Orci, L.; Malaisse, W. *Diabetes* **1980**, *29*, 943-944.

Orci, L.; Vassalli, J.-D.; Perrelet, A. *Sci. Am.* **1988,** *259*, 85-94.

Orci, L.; Thorens, B.; Ravazzola, M.; Lodish, H. F. *Science* **1989**, *45*, 295-297.

Östenson, C.-G., *Acta Physiol. Scand.* **2001**, *171*, 241-247.

Paras, C. D.; Kennedy, R. T. *Anal. Chem.* **1995,** *67*, 3633-3637.

Paras, C. D.; Qian, W. J.; Lakey, J. R.; Tan, W. H.; Kennedy, R. T. *Cell Biochem. Biophys.* **2000,** *33*, 227-240.

Parpura, V.; Tong, W.; Yeung, E. S.; Haydon, P. G. *J. Neurosci. Methods* **1998,** *82*, 151-158.

Patel, Y. C.; Amherdt, M.; Orci, L. *Science* **1982,** *217*, 1155-1156.

Pawley, J. B. *The Handbook of Biological Confocal Microscopy*, 2nd ed.; Plenum Press: New York, 1995.

Penner, R.; Neher, E. *J. Exp. Biol.* **1988,** *139*, 329-345.

Penner, R.; Neher, E. *Trends Neurosci.* **1989,** *12*, 159-163.

Perez-Clausell, J.; Danscher, G. *Brain Res.* **1986,** *362*, 358-361.

Persaud, S. J.; Asare-Anane, H.; Jones, P. M. *FEBS Lett.* **2002,** *510*, 225-228.

Peters, S.; Koh, J.; Choi, D. W. *Science* **1987,** *236*, 589-593.

Pipeleers, D.; Kiekens, R.; Ling, Z.; Wilikens, A.; Schuit, F. *Diabetologia* **1994,** *37(Suppl. 2*), S57-64.

Polonsky, K. S.; Given, B .D.; Van Cauter, E. *J. Clin. Invest.* **1988a**, *81*, 442-448.

Polonsky, K. S.; Given, B. D.; Hirsch, L. J.; Tillil, H.; Shapiro, E. T.; Beebe, C.; Frank, B. H.; Galloway, J. A.; Van Cauter, E. *N. Engl. J. Med.* **1988b**, *318*,1231-1239.

Polonsky, K. S. *Diabetes* **1995**, *44*, 705-717.

Porzio, O.; Federici, M.; Hribal, M. L.; Lauro, D.; Accili, D.; Lauro, R.; Borboni, P.; Sesti, G. *J. Clin. Invest.* **1999**, *104*, 357-364.

Pouli, A. E.; Emmanouilidou E.; Zhao, C.; Wasmeier C.; Hutton J. C.; Rutter, G. A. *Biochem. J.* **1998**, *333*, 193-199.

Qian, W. J.; Aspinwall, C. A.; Battiste, M. A.; Kennedy, R. T. *Anal. Chem.* **2000**, *72*, 711-717.

Qian, W. J.; Kennedy, R. T. *Biochem. Biophys. Res. Commun.* **2001**, *286*, 315-321.

Robinson, I. M.; Finnegan, J. M.; Monck, J. R.; Wightman, R. M.; Fernandez, J. M. *Proc. Natl. Acad. Sci. U.S.A.* **1995**, *92*, 2474-2478.

Roe, M. W.; Mertz, R. J.; Lancaster, M. E.; Worley III, J. F.; Dukes, I. D. *Am. J. Physiol.* **1994**, *266*, E852-862.

Roper, M. G.; Qian, W. J.; Zhang, B. B.; Kulkarni, R. N.; Kahn, C. R.; Kennedy, R. T. *Diabetes* **2002**, *51(Suppl. 1)*, S43-S49.

Rosario, L. M.; Atwater, I.; Scott, A. M. *Adv. Exp. Med. Biol.* **1986**, *211*, 413-425.

Rorsman, P.; Ashcroft, F. M.; Trube, G. *Pflügers Arch.* **1988**, *412*, 597-603.

Rothenberg, P. L.; Willison, L. D.; Simon, J.; Wolf, B. A. *Diabetes* **1995**, *44*, 802-809.

Rothman, J. E. *Nature* **1994**, *372*, 55-63.

Rutter, G. A. *Curr. Biol.* **1999**, *9*, 443-445.

Sala, F.; Hernandez-Cruz, A. *Biophys. J.* **1990**, *57*, 313-24.

Santos, R. M.; Rosario, L. M.; Nadal, A.; Garcia-Sancho, J.; Soria, B.; Valdeolmillos, M. *Pflügers Arch.* **1991**, *418*, 417-422.

Schiavo, G.; Gu, Q. M.; Pretwich, G. D.; Sollner,T. H.; Rothman, J. E. *Proc. Natl. Acad. Sci. U.S.A.* **1996**, *93*, 13327-13332.

Schroeder, T. J.; Jankowski, J. A.; Kawagoe, K. T.; Wightman, R. M.; Lefrou, C.; Amatore, C. *Anal. Chem.* **1992**, *64*, 3077-3083.

Schuit, F. C.; Derde, M. P.; Pipleers, D. G. *Diabetologia* **1989**, *32*, 207-212.

Sensi, S. L.; Canzoniero, L. M. T.; Yu, S. P.; Ying, H. S.; Koh, J.-Y.; Kerchner, G. A.; Choi, D. W. *J. Neuroscience* **1997**, *17*, 9554-9564.

Shepherd, P. R.; Reaves, B. J.; Davidson, H. W. *Trends Cell Biol.* **1996**, *6*, 92-97.

Smart, T. G.; Moss, S. J.; Xie, X., Huganir, R. L. *Br. J. Pharmacol.* **1991**, *103*, 1837-1839.

Smith, C. B.; Betz, W. J. *Nature* **1996**, *380*, 531-534.

Smith, P. A.; Duchen, M. R.; Ashcroft, F. M. *Eur. J. Physiol.* **1995**, *430*, 808-818.

Snitsarev, V.; Budde, T.; Stricker, T. P.; Cox, J. M.; Krupa, D. J.; Geng, L.; Kay, A. R. *Biophys. J.* **2001**, *80*,1538-1546.

Söllner, T.; Whiteheart, S. W.; Brunner, M.; Erdjument-Bromage, H.; Geromanos, S.; Tempst, P.; Rothman, J. E. *Nature* **1993**, *362*, 318-324.

Squires, P. E.; Hauge-Evans, A. C.; Persaud, S. J.; Jones, P. M. *Cell Calcium* **2000**, *27*, 287-296.

Steyer, J. A.; Horstmann, H.; Almers, W. *Nature* **1997**, *388*, 474-478.

Strein, T. G.; Ewing, A. G. *Anal. Chem.* **1992**, *64*, 1368-1373.

Sun, X. J.; Pons, S.; Wang, L. M.; Zhang, Y. T.; Yenush, L.; Burks, D.; Myers, M. G.; Glasheen, E.; Copeland, N. G.; Jenkins, N. A.; Pierce, J. H.; White, M. F. *Mol. Endocrinol.* **1997a**, *11*, 251-262.

Sun, W.-C.; Gee, K. R.; Klaubert, D. H.; Haugland, R. P. *J. Org. Chem.* **1997b**, *62*, 6469.

Tan, W. H.; Parpura, V.; Haydon, P. G.; Yeung, E. S. *Anal. Chem.* **1995**, *67*, 2575-2579.

Tan, W. H.; Haydon, P. G.; Yeung, E. S. *Appl. Spectroscopy*, **1997**, *51*, 1139-1143.

Tatham, P. E. R.; Duchen, M. R.; Millar, J. *Pflügers Arch.* **1991**, *419*, 409-414.

Taylor, S. I. *Cell* **1999**, *97*, 9-12.

Theler, J. M.; Mollard, P.; Guerineau, N.; Vacher, P.; Pralong, W. F.; Schlegel, W.; Wollheim, C. B. *J. Biol. Chem.* **1992**, *267*, 18110-18117.

Thompson, R. B.; Whetsell, W. O.; Maliwal, B. P.; Fierke, C. A.; Frederickson, C. J. *J. Neurosci. Methods* **2000**, *96*, 35-45.

Tong, W.; Yeung, E. S. *Appl. Spectroscopy* **1998**, *52*, 407-413.

Travis, E. R.; Wightman, R. M. *Annu. Rev. Biophys. Biomol. Struct.* **1998**, *27*, 77-103.

Tsien, R. Y.; Bacskai, B. J. In *Handbook of Biological Confocal Microscopy*; Pawley, J. B., Ed.; Plenum Press: New York, 1995; pp 459-478.

Tsuboi, T.; Zhao, C.; Terakawa, S.; Rutter, G. A. *Curr. Biol.* **2000**, *10*, 1307-1310.

Valdeolmillos, M.; Santos, R. M.; Contreras, D.; Soria, B.; Rosario, L. M. *FEBS Lett.* **1989**, *259*, 19-23.

Valdeolmillos, M.; Nadal, A.; Soria, B.; Garcia-Sancho, J. *Diabetes* **1993**, *42*, 1210-1214.

Velloso, L. A.; Carneiro, E. M.; Crepaldi, S. C.; Boschero, A. C.; Saad, M. J. A. *FEBS Lett.* **1995**, *377*, 353-357.

Varea, E.; Ponsoda, X.; Molowny, A.; Danscher, G; Lopez-Garcia, C. *J. Neurosci. Methods* **2001**, *110*, 57-63.

Verspohl, E. J.; Ammon, H. P. T. *J. Clin. Invest.* **1980**, *65*, 1230-1237.

Westerlund, J.; Ortsater, H.; Palm, F.; Sundsten, T.; Bergsten, P. *Eur. J. Endocrinol.* **2001**, *144*, 667-675.

Westerlund, J.; Wolf, B. A.; Bergsten, P. *Diabetes* **2002**, *51(Suppl. 1)*, S50-S52

White, M. F. *Diabetologia* **1997**, *40*, S2-S17.

Wightman, R. M.; Jankowski, J. A.; Kennedy, R. T.; Kawagoe, K. T.; Schroeder, T. J.; Leszczyszyn, D. J.; Near, J. A.; Diliberto, E. J.; Viveros, O. H. *Proc. Natl. Acad. Sci. U.S.A.* **1991**, *88*, 10754-10758.

Williams, R. M.; Shear, J. B.; Zipfel, W. R.; Maiti, S.; Webb, W. W. *Biophys. J.* **1999**, *76*, 1835-1846.

Wiser, O.; Bennett, M. K.; Atlas, D. *EMBO J.* **1996**, *15*, 4100-4110.

Wiser, O.; Trus, M.; Hernandez, A.; Renstrom, E.; Barg, S.; Rorsman, P.; Atlas, D. *Proc. Natl. Acad. Sci. U.S.A.* **1999,** *96*, 248-53.

Withers, D. J.; Gutierrez, J. S.; Towery, H.; Burks, D. J.; Ren, J.-M.; Previs, S.; Zhang, Y.; Bernal, D.; Pons, S.; Shulman, G. I.; Bonner-Weir, S.; White, M. F. *Nature* **1998,** *391*, 900-904.

Withers, D. J.; Burks, D. J.; Towery, H.; Altamuro, S. L.; Flint, C. L.; White, M. F. *Nat. Genet.* **1999,** *23*, 32-40.

Xu, G.; Marshall, C. A.; Lin, T.-A.; Kwon, G.; Munivenkatappa, R. B.; Hill, J. R.; Lawrence, J. C.; McDaniel, M. L. *J. Biol. Chem.* **1998a,** *273*, 4485-4491.

Xu, G.; Rothenberg, P. L. *Diabetes* **1998b,** *47*, 1243-1252.

Xu, G. G.; Gao Z. Y.; Borge, P. D.; Wolf B. A. *J. Biol. Chem.* **1999,** *274*, 18067-18074.

Xu, G. G.; Gao Z. Y.; Borge, P. D.; Jegier, P. A.; Young, R. A.; Wolf B. A. *Biochemistry* **2000,** *39*, 14912-14919.

Yada, T.; Kakei, M.; Tanaka, H. *Cell Calcium* **1992,** *13*, 69-76.

Yalow, R. S.; Berson, S. A. *J. Clin. Invest.* **1960,** *39*, 1157-1175.

Yang, S. N.; Larsson, O.; Branstrom, R.; Bertorello, A. M.; Leibiger, B.; Leibiger, I. B.; Moede, T.; Kohler, M.; Meister, B.; Berggren, P. O. *Proc. Natl. Acad. Sci. U.S.A.* **1999,** *96*, 10164-10169.

Yeung, E. S. *Anal. Chem.* **1999,** *71*, 522A-529A.

Zalewski, P. D.; Forbes, I. J.; Betts, W. H. *Biochem. J.* **1993,** *296*, 403-408.

Zalewski, P. D.; Millard, S. H.; Forbes, I. J.; Kapaniris, O.; Slavotinek, A.; Betts, W. H.; Ward, A. D.; Lincoln, S. F.; Mahadevan, I. B. *J. Histochem. Cytochem.* **1994,** *42*, 877-884.

Zawalich, W. S.; Zawalich, K. C.; Kelley, G. G. *Endocrinology* **1995,** *136*, 4903-4909.

Zhou, Z.; Misler, S. *Proc. Natl. Acad. Sci. U.S.A.* **1995,** *92*, 6938-6942.

Zhou, Z.; Misler, S. *J. Biol. Chem.* **1996,** *270*, 270-277.

BIOGRAPHICAL SKETCH

Weijun Qian was born June 25, 1972, in Longyou, Zhejiang, P. R. China. He obtained a Bachelor of Science degree in chemistry from Nanjing University in July 1994. From 1994 to 1997, he worked as a graduate research assistant under the direction of Professor Zuxun Zhang in the Chemistry Department at Nanjing University. In August 1997, he came to the United States and continued his graduate study under the direction of Dr. Robert T. Kennedy in the Chemistry Department at the University of Florida. He completed his research in May 2002, obtaining a Doctor of Philosophy degree.

I certify that I have read this study and that in my opinion it conforms to acceptable standards of scholarly presentation and is fully adequate, in scope and quality, as a dissertation for the degree of Doctor of Philosophy.

Robert T. Kennedy, Chairman
Professor of Chemistry

I certify that I have read this study and that in my opinion it conforms to acceptable standards of scholarly presentation and is fully adequate, in scope and quality, as a dissertation for the degree of Doctor of Philosophy.

Richard A. Yost
Professor of Chemistry

I certify that I have read this study and that in my opinion it conforms to acceptable standards of scholarly presentation and is fully adequate, in scope and quality, as a dissertation for the degree of Doctor of Philosophy.

Weihong Tan
Associate Professor of Chemistry

I certify that I have read this study and that in my opinion it conforms to acceptable standards of scholarly presentation and is fully adequate, in scope and quality, as a dissertation for the degree of Doctor of Philosophy.

Jon D. Stewart
Associate Professor of Chemistry

I certify that I have read this study and that in my opinion it conforms to acceptable standards of scholarly presentation and is fully adequate, in scope and quality, as a dissertation for the degree of Doctor of Philosophy.

Mark A. Atkinson
Professor of Pathology, Immunology, and
Laboratory Medicine

This dissertation was submitted to the Graduate Faculty of the Department of Chemistry in the College of Liberal Arts and Sciences and to the Graduate School and was accepted as partial fulfillment of the requirements for the degree of Doctor of Philosophy.

May 2002

Dean, Graduate School